Title

Regulation of Microtubule Motors by Activating Adaptors

ISBN

9798189271335

Author

Aslan, Merve

Publication Date

2026-05-01

Peer reviewed|Thesis/dissertation

Regulation of Microtubule Motors by Activating Adaptors

By

Merve Aslan

A dissertation submitted in partial satisfaction of the

requirements for the degree of

Doctor of Philosophy

in

Biophysics

in the

Graduate Division

of the

University of California, Berkeley

Committee in charge:

Professor A. Yildiz, Chair

Professor E. Nogales

Professor J. Hurley

Professor A. Martin

Spring 2026

Regulation of Microtubule Motors by Activating Adaptors

By

Merve Aslan

Abstract

Regulation of Microtubule Motors by Activating Adaptors

By

Merve Aslan

Doctor of Philosophy in Biophysics

University of California, Berkeley

Professor A. Yildiz, Chair

Microtubule-based motors play essential roles in intracellular organization and cell division by transporting cargos and generating force along microtubules. Kinesin and dynein are microtubule motors that move toward the plus and minus ends of microtubules, respectively. These motors are highly coordinated to enable bidirectional cargo transport and precise spatial organization within cells. However, the molecular mechanisms that regulate kinesin and dynein activity and coordination remain elusive.

In my doctoral work, I addressed this question using biochemical reconstitution and single-molecule imaging. First, I studied the activation and regulation of kinesin and dynein by the mitochondrial adaptor protein TRAK. I showed that TRAK activates dynein and enhances kinesin activation in vitro. In addition, I found that TRAK adaptors can recruit kinesin and dynein simultaneously, and these complexes, in which both motors are associated, move exclusively to the plus end at kinesin speed, demonstrating that dynein is carried by kinesin as an inactive passenger. Furthermore, I demonstrated that recruitment of syntaphilin to mitochondria acts as a static anchor that opposes motor-driven motility, leading to mitochondrial pausing.

Additionally, I investigated the activation and regulation of dynein by its mitotic cargo adaptor NuMA. Using a biochemical reconstitution approach, I discovered that the N-terminal fragment of NuMA activates dynein. At the same time, the C-terminal region of NuMA binds and suppresses microtubule minus-end dynamics in vitro. The C-terminal region also recognizes microtubule minus ends through its MTBD1 region. Full-length NuMA is autoinhibited during interphase, and its ability to interact with dynein is significantly enhanced by phosphomimetic mutations at CDK1, Aurora A, and Plk1 phosphorylation sites at its C terminus. Together with dynein/dynactin, activated NuMA sorted and focused the minus-ends of microtubules into aster-like structures, resembling spindle pole focusing during prometaphase. This work provides mechanistic insight into how the adaptor protein NuMA regulates dynein activation during mitosis

Table of Contents

ACKNOWLEDGEMENTS

First, I would like to thank my supervisor, Ahmet Yildiz, for believing in me and guiding me throughout my PhD. His ambitious mentorship and his constant reminder that nothing is more exciting than the work we do in the lab kept me focused even when things were challenging.

I owe special thanks to Amanda Jack, my first mentor in the Yildiz lab, who patiently helped me set everything up from the start using detailed, well-documented protocols.

Furthermore, I would like to thank former Yildiz lab members John Canty and Andrew Hensley for collaborating with me on the TRAK project. John provided invaluable guidance, which gave me the courage to work with the biochemically "impossible" protein, NuMA.

My sincere thanks also go to my collaborators on the NuMA project—Ennio d'Amico, Andrew Carter, Nathan Cho, and Sophie Dumont—whose valuable contributions made our story impactful and compelling. I also thank my thesis committee members, Eva Nogales, James Hurley, and Andy Martin, for listening to my presentations and asking valuable questions to help shape the project.

I would also like to thank the Yildiz lab members—Joseph, Joy, Aryan, Ipsita, Yuanchang, John, Yifei, and Burak—who created a very welcoming lab environment in which I felt energized and encouraged to come in every day.

My special thanks go to my dear sister Selime and her family, who listened to my weekly PhD updates and were always there for me. Lastly, I am most grateful to my dear family—Aziz, Mina, and Azra—for their endless love and support throughout my PhD. I cannot imagine completing this marathon at this stage of my life without them.

Chapter 1. Introduction

The microtubule cytoskeleton facilitates the internal organization of the cell and the intracellular transport of organelles, vesicles, and RNAs to distal regions. During interphase, microtubules originate from the centrosome located near the nucleus and extend their plus ends towards the cell periphery. In mitosis, microtubules undergo a large reorganization to form the bipolar mitotic spindle, with minus ends targeting the spindle poles and plus ends interacting with kinetochores and the cell cortex. Bipolar spindle formation is essential for accurate segregation of duplicated chromosomes into two daughter cells in mitosis. Errors in spindle formation and chromosome segregation result in missing or extra copies of chromosomes, called aneuploidy, which is a hallmark of cancer.

Microtubules, nucleated from microtubule-organizing centers near the centrosomes, are 25-nm-wide, cylindrical filaments that are composed of alpha and beta tubulin dimers. Tubulin dimers polymerize in a head-to-tail manner, which means the beta subunit of one tubulin dimer contacts the alpha subunit of the next dimer. Each protofilament is polarized, with alpha-tubulin exposed at one end and beta-tubulin at the other. These polarized 13 parallel protofilaments are bundled around a hollow core, generating distinct plus (beta-tubulin-exposed) and minus (alpha-tubulin-exposed) ends. Microtubules are dynamically unstable, polymerizing and depolymerizing rapidly at the plus end and more slowly at the minus end in the cell.

Microtubule polarity can be recognized by microtubule-associated motor proteins, kinesin and dynein, which is critical for their diverse and dynamic cellular functions. Kinesin and dynein convert chemical energy into mechanical work to move unidirectionally, facilitating bidirectional cargo transport along microtubules. In this study, we focused on kinesin and dynein and on how their activities are regulated by activating adaptor proteins.

1.1 Kinesin

45 different genes in humans encode the kinesin family of proteins, which is responsible for diverse cellular processes, from unidirectional cargo transport to microtubule dynamics[1]. Kinesins have a conserved motor domain, and the position of this domain classifies kinesin motors as N-kinesins (N-terminal motor domain), M-kinesins (motor domain is in the middle), and C-kinesins (C-terminal motor domain)[1]. Among them, N-kinesins are the plus-end-directed motors that drive long-distance intracellular cargo transport.

Kinesin 1 family motors (KIF5A, B, and C) are principal motors for plus-end directed cargo transport, and KIF5B is ubiquitously expressed in all tissues, whereas KIF5A and KIF5C are specific to neurons[2,3]. KIF5B (hereafter kinesin) is used in this study.

The kinesin motor domain is the mechanical element of the protein that generates motility. Motor domain contains ATP hydrolysis and MT binding domains, and it is attached to the neck coil of the stalk through an unstructured, short neck linker[4]. This 14-amino acid-long neck linker enables motor domains to bind adjacent tubulin dimers and coordinates the two heads by docking and undocking from the motor domain in a nucleotide-dependent manner. Kinesin moves 8 nm per step using a hand-over-hand mechanism driven by ATP hydrolysis along the microtubules. This

motility is generated by coordinated coupling between nucleotide-bound states and conformational changes in the neck linker and the microtubule-binding interface.

The motor domain binds and hydrolyzes ATP in solution. Since bound ADP release is very slow, the basal ATPase activity of the motor remains low[5]. Both motor heads exist in an ADP-bound state in solution, which confers low affinity for microtubules (state 1)[6]. Upon encountering a microtubule, one head (head 1) binds to the microtubule and releases its ADP, entering a nucleotide-free state, while the second head (head 2) remains detached (state 2)[7]. ATP binding to head 1 then induces partial docking of its neck linker, generating a forward movement that biases head 2 approximately 8 nm toward the microtubule plus end (state 3). Subsequent ATP hydrolysis in head 1 produces the ADP·Pi state, completing neck linker docking and further advancing head 2 toward the tubulin subunit located on the plus-end side of head 1 (state 4). The binding of head 2 to the microtubule stimulates the release of its ADP (state 5). ATP binding to head 2 is temporally gated and does not occur until head 1 releases inorganic phosphate and detaches from the microtubule (state 6). At this point, head 1 occupies the trailing position near its original binding site, and kinesin awaits ATP binding to head 2, thereby resetting the system to initiate the next ATPase cycle (state 7)[8-10] (**Fig. 1.1a**).

Kinesin contains two copies of the heavy chain, which bind to the microtubule through the motor domain and dimerize through the coiled-coil stalk. Hinge regions in the stalk give the motor flexibility. The C-terminal kinesin tail either directly interacts with cargo or forms heterotetramers by interacting with kinesin light chains. When the kinesin tail is not bound to cargo, it folds back around the hinges onto the motor domain to inhibit its catalytic activity. Autoinhibition of kinesin regulates motor motility when it is necessary for the cell and prevents futile energy expenditure. Rescue from autoinhibited conformation requires a two-step activation process. First, the microtubule-associated protein MAP7 binds to the coiled-coil, which relieves the autoinhibited conformation, and second, binding to a cargo or cargo adaptor protein further stabilizes the active motor conformation (**Fig. 1.1 b**).

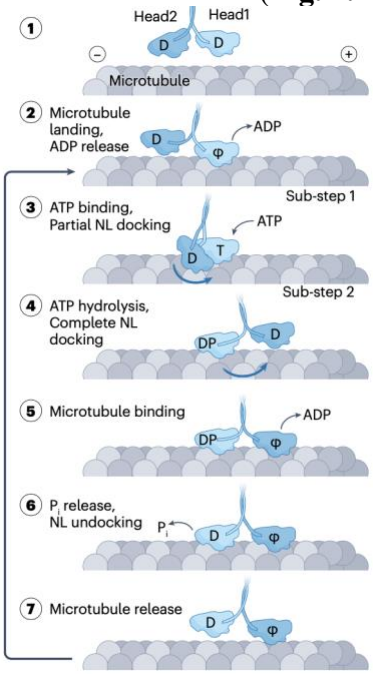

Fig. 1.1. Mechanochemical cycle of kinesin. Kinesin initiates its cycle with both motor heads in an ADP-bound state, conferring low microtubule affinity (state 1). Upon microtubule encounter, one head binds and releases ADP, while the partner head remains detached (state 2). ATP binding to the bound head induces partial neck-linker docking, biasing the unbound head forward toward the microtubule plus end (state 3). ATP hydrolysis completes neck linker docking and advances the unbound head toward the next tubulin binding site (state 4). Microtubule binding of the leading head triggers ADP release (state 5). ATP binding to the new leading head is gated until phosphate release and detachment of the trailing head occur (state 6), resetting the motor to initiate the next ATPase cycle (state 7). (Reproduced from Yildiz A. (2025). Nat Rev Mol Cell Biol *26*, 86–103)

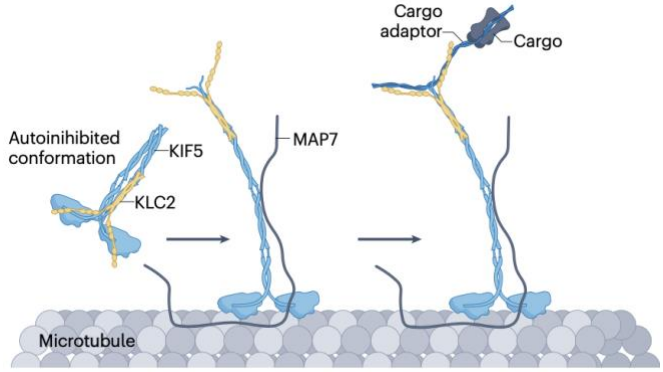

Fig. 1.2. Activation of kinesin. Kinesin adopts an autoinhibited conformation by tail region folding back onto the motor domain. MAP7 interaction and further cargo/cargo adaptor binding to the tail region fully activate the motor. (Reproduced from Yildiz A. (2025). Nat Rev Mol Cell Biol *26*, 86–103)

1.2 Dynein

Cytoplasmic dynein (hereafter dynein) is the motor responsible for minus-end-directed motility in the cell[11]. It transports membrane-bound organelles (Golgi vesicles, peroxisomes, and endocytic pathway components), viruses, transcription factors, misfolded proteins, and mRNA in the retrograde direction. In addition, dynein anchors organelles to the microtubule network, promotes nuclear migration during neuronal development, and positions the mitotic spindle in dividing cells[12].

Human dynein is a multi-subunit protein complex that contains two copies of six subunits: the heavy chain (DHC), intermediate chain (DIC), light intermediate chain (DLIC), and three different light chains (Roadblock, LC8, and Tctex)[13]. DHC is the largest subunit and contains the C-terminal AAA+ motor domain and the microtubule binding domain. The N-terminal tail region of DHC mediates dimerization of the motor and provides a scaffold for the attachment of two copies of DIC and DLIC, as well as three light chains. The catalytic ring of the motor domain comprises six AAA+ (AAA1-AAA6) sites[14]. The catalytic core is spatially separated from the microtubule-binding domain by an antiparallel coiled-coil stalk that extends from the AAA+ ring between the AAA4 and AAA5 sites[15]. A second antiparallel coiled coil, known as the buttress, originates from AAA5 and interacts with the stalk near the AAA+ ring. The linker, an alpha helical bundle

connected to the N terminus of the AAA+ ring[16,17], changes conformation in a nucleotide-dependent manner at the ring surface, providing the mechanical force for dynein motility.

ATP hydrolysis in the AAA+ domain drives a mechanochemical cycle involving at least four nucleotide states: ATP, ADP.Pi, ADP, and nucleotide-free. Primary catalytic activity begins with ATP binding to AAA1, followed by conformational changes within the stalk-microtubule binding domain and the linker domain. When AAA1 is nucleotide-free, dynein binds tightly to the microtubule, and the linker adopts a straight conformation, emerging from the ring near the AAA5 site. Upon ATP binding to AAA1, the interface between AAA1 and AAA2 closes, initiating coordinated rigid-body rearrangements within the AAA+ ring. During this transition, AAA5 and AAA6 move closer together, causing the buttress to shift the registry of the stalk coiled-coils and promote the release of the microtubule-binding domain from the microtubule. Concurrently, conformational changes in AAA2–AAA4 destabilize the straight linker conformation and induce the priming movement of the linker near AAA2. This priming stroke displaces the unbound microtubule-binding domain toward the microtubule minus end, biasing dynein stepping in the minus-end direction. Reattachment of the microtubule-binding domain triggers inorganic phosphate (Pi) release from AAA1, likely through reversal of the stalk coiled-coil registry shift. The linker subsequently disengages from AAA2 and returns to its straight conformation, generating the power stroke that advances the cargo forward. Following ADP release, dynein is reset for the next nucleotide cycle, completing a single step toward the microtubule minus end (**Fig. 1.3**).
Both recombinant and tissue-purified mammalian dynein behave as weak motors in vitro, diffusing along microtubules and generating low forces that do not reflect dynein's robust motility in vivo. Several studies revealed that dynein adopts an autoinhibited conformation termed the phi-particle, due to its resemblance to the Greek letter ϕ. In phi conformation, the motor domains face each other in a mirror-symmetric arrangement, preventing simultaneous microtubule binding (**Fig. 1.4a**). Dynein activation requires the assembly of a ternary complex with dynactin and a coiled-coil adaptor protein. Dynactin is a multi-subunit protein complex composed of 11 different polypeptides (**Fig. 1.4b**). The structural backbone of dynactin is a short actin filament consisting of eight copies of Arp1 and one β-actin molecule. This filament is capped at its pointed end by four associated proteins (p62, p27, p25, and Arp11) and at its barbed end by CAPZαβ. Positioned near the barbed end is the shoulder domain, composed of four copies of dynamitin and two copies of each of p24 and p150^{glued}. The largest subunit of dynactin, p150^{glued}, extends from the N-terminal shoulder through a long coiled-coil region and terminates in a CAP-Gly domain. This coiled-coil facilitates interaction with the N-terminus of the DIC. The CAP-Gly domain binds microtubules and contributes to the localization of dynactin and dynein at microtubule plus ends through interactions with EB1 and CLIP170, which are enriched at growing microtubule tips.

Dynein and dynactin interact weakly on their own, and formation of the active complex requires a coiled-coil adaptor protein that spans the length of the dynactin filament and interacts with DHC and DLIC (**Fig. 1.4c**). Adaptor proteins are not only essential for dynein-dynactin activation but also for recruiting dynein to a wide range of intracellular cargos[18]. Although these adaptors lack sequence conservation, they share common features, including an extended coiled-coil region flanked by an amino-terminal domain - such as a CC1 box (AAxxG motif), Hook, or EF-hand domain, that mediates interaction with DLIC - as well as a carboxy-terminal Spindly motif that binds to the pointed end of dynactin. In addition, adaptor proteins share a heavy chain binding site

(HBS1) through which they interact with DHC. Several adaptors are maintained in an autoinhibited state when isolated, and their ability to bind dynein is activated upon engagement with cargo, cargo-associated receptor proteins, or other factors that connect these adaptors to their cargo.

Because many cargos recruit both kinesin and dynein through adaptor proteins, intracellular transport has often been described as a 'tug of war' between opposing motors. One motor can defeat the opposing motor in a mechanical competition. Furthermore, the frequent pauses and directional reversals of cargos observed in live-cell studies have been interpreted as evidence of mechanical competition between opposing motors. However, recent studies have shown that inhibiting one motor eventually suppresses motility in both directions, suggesting that cargo transport is regulated through coordination rather than simple competition between motors. Emerging studies further suggest that coordination of opposing motors is mediated by cargo adaptors that attach motors to their specific cargos. Understanding how adaptor proteins coordinate opposing motors is therefore critical for explaining bidirectional cargo transport in cells.

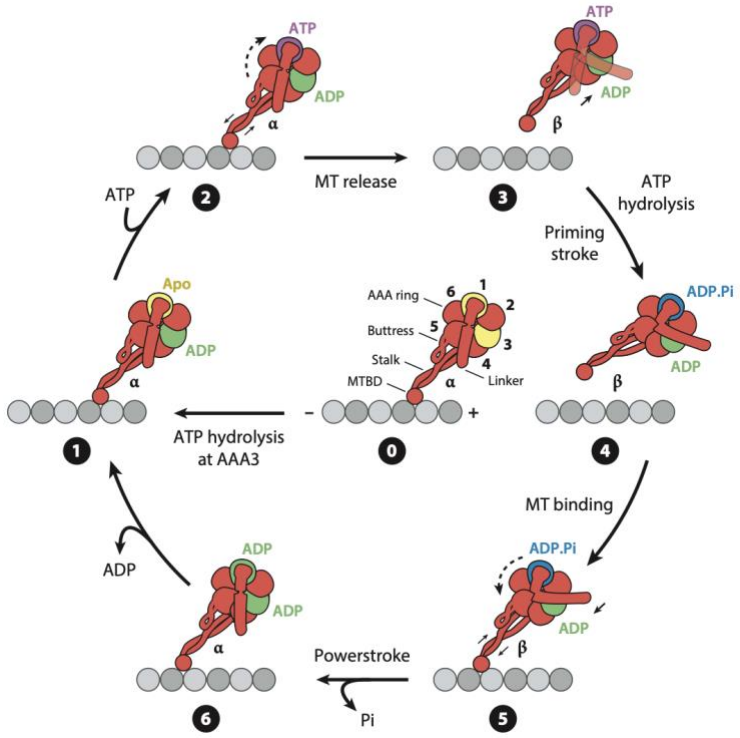

Fig. 1.3. Mechanochemical cycle of dynein. b. In the nucleotide-free state, dynein binds tightly to the microtubule with the linker in a straight conformation (1). ATP binding to AAA1 induces closure of the AAA1–AAA2 interface and coordinated rearrangements within the AAA+ ring, leading to registry shifts in the stalk coiled coils and release of the microtubule-binding domain (2-3). Conformational changes in AAA2–AAA4 drive linker priming, biasing movement toward the microtubule minus end (4). Rebinding to the microtubule promotes phosphate release, followed by linker straightening that generates the power stroke (5). ADP release resets dynein for the next stepping cycle (6). (Reproduced from Canty J. *et al.* (2021). Annu. Rev. Biophys. *50*, 549–574)

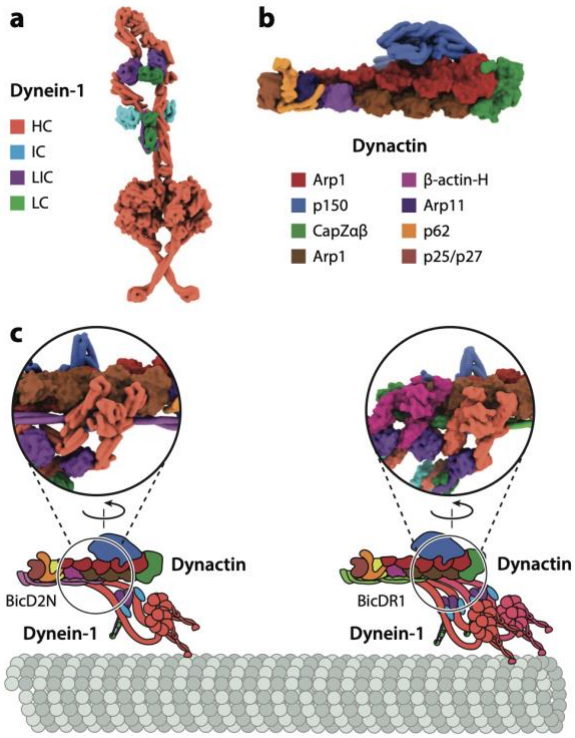

Fig 1.4. Structure and activation mechanism of dynein. a. Dynein phi particle conformation **b.** Structure of dynactin. **c.** Dynein forms an active complex with dynactin and a coiled-coil region of an adaptor protein (BicD2N and BicDR1). (Reproduced from Canty J. *et al.* (2021). Annu. Rev. Biophys. *50*, 549–574)

1.3 Mitochondrial Transport and the TRAK Adaptor

Bidirectional cargo transport is particularly critical in specialized cells such as neurons, which have extremely long axons. Newly synthesized components must be transported long distances along the axon, and damaged organelles and vesicles containing misfolded proteins must be transported back to the soma for degradation.

Mitochondria are among the most important organelles transported bidirectionally along axons to satisfy local energy demands and buffer excess calcium in neurons. In mature neurons, two-thirds of mitochondria are stationary, particularly at locations with elevated calcium levels. Recent studies have identified key components of mitochondrial transport machinery. One such factor is Miro, a Rho GTPase, that contains GTP- and calcium-binding sites. Miro is a mitochondrial outer membrane protein that binds to the adaptor protein TRAK. TRAK then recruits kinesin and dynein to form an active transport complex. TRAK1 is predominantly expressed in axons, whereas TRAK2 is more abundant in dendrites. Knockdown of TRAK1/2 reduces mitochondrial motility along axons by approximately 60%. Impairment of bidirectional mitochondrial motility is linked to neurodegenerative diseases. However, the molecular mechanism of mitochondrial transport remains unclear.

1.4 Dynein Regulation at the Mitotic Spindle by NuMA

Dynein plays crucial roles in cell division by focusing microtubule minus ends in spindle poles, generating pulling forces on astral microtubules, and transporting spindle-activation checkpoints (SAC) away from kinetochores in metaphase. All these activities of dynein require a cargo adaptor and Nuclear Mitotic Apparatus protein (NuMA) is one of them.

NuMA localizes to the nucleus in interphase, where it helps as a scaffolding protein for the formation of a single, round nucleus[19,20]. After nuclear envelope breakdown, NuMA accumulates at MT minus-ends and recruits dynein. Together with dynein, NuMA helps focus the minus-ends of MTs at spindle poles and maintain a steady-state spindle structur[21-26]. Minus-end-directed forces generated by dynein counteract forces generated by plus-end-directed kinesin-5s[27,28] to maintain spindle structure[29,30]. NuMA also recruits dynein to the cell cortex[31-35], where dynein anchors astral MTs and generates tension to determine the position and orientation of the spindle[35-37]. Consistent with its cellular roles, NuMA dysfunction causes defects in spindle mechanics and architecture, as well as micronuclei formation[38].

NuMA is a large (237 kDa) and elongated protein composed of an N-terminal HOOK domain (amino acids (a.a.) 1-153) and a C-terminal region (a.a. 1700-2115) separated by a ~210 nm long coiled-coil domain[39,40]. This central coiled-coil promotes dimerization[40] and provides the extended architecture required for crosslinking MTs and DNA[20,41,42], as well as for efficiently capturing astral MTs at the cell cortex[43]. The coiled-coil also prevents the binding of NuMA to chromosomes during mitosis[20]. The intrinsically disordered C-terminal region contains two MT-binding sites (MTBD1 (a.a. 1914-1985) and MTBD2 (a.a. 2002-2115)), as well as DNA- and other partner-binding sites, a clustering motif, and a nuclear localization signal[38]. MTBD2 interacts with the MT lattice[44] and is required for cortical spindle-pulling activity in human cells[35,36]. MTBD1 binds MTs more weakly[45], but it is essential for spindle pole focusing[46,47] and accumulation of NuMA at the minus-end of MTs in mammalian cells[26]. However, studies in other cell types report differing roles for MTBD1 and MTBD2 in spindle organization and orientation[48], and the mechanisms by which these domains interact with MTs and regulate MT dynamics remain unclear[48].

During my Ph.D., I used biochemical reconstitution and single-molecule imaging to investigate how adaptor proteins regulate the activity and coordination of kinesin and dynein. First, I examined how the mitochondrial adaptor TRAK controls bidirectional transport. Second, I studied how the mitotic adaptor NuMA activates dynein and organizes microtubules.

Chapter 2. Regulation of Dynein and Kinesin by Mitochondrial Cargo Adaptor TRAK

This work presented in this chapter was published in this paper:
Canty, J.T.*, Hensley, A.*, **Aslan, M.*,** Jack A., and Yildiz, A. TRAK adaptors regulate the recruitment and activation of dynein and kinesin in mitochondrial transport. *Nat Commun,* 14, 1376 (2023). https://doi.org/10.1038/s41467-023-36945-8
* Equal contribution

2.1 Abstract

Mitochondrial transport along microtubules is mediated by Miro1 and TRAK adaptors that recruit kinesin-1 and dynein-dynactin. To understand how these opposing motors are regulated during mitochondrial transport, we reconstitute the bidirectional transport of Miro1/TRAK along microtubules in vitro. We show that the coiled-coil domain of TRAK activates dynein-dynactin and enhances the motility of kinesin-1 activated by its cofactor MAP7. TRAK adaptors that recruit both motors move towards kinesin-1's direction, whereas kinesin-1 is excluded from binding TRAK transported by dynein-dynactin, avoiding motor tug-of-war. We also test the predictions of the models that explain how mitochondrial transport stalls in regions with elevated Ca^{2+}. Transport of Miro1/TRAK by kinesin-1 is not affected by Ca^{2+}. Instead, the microtubule docking protein syntaphilin induces resistive forces that stall kinesin-1 and dynein-driven motility. Our results suggest that mitochondrial transport stalls by Ca^{2+}-mediated recruitment of syntaphilin to the mitochondrial membrane, not by disruption of the transport machinery.

2.2 Introduction

Mitochondria are cellular power plants that generate most of the ATP needed for many biochemical reactions and have a high capacity to buffer cytosolic Ca^{2+}. In neurons, mitochondria are distributed to distal regions where ATP and Ca^{2+} buffering are in high demand, such as synapses and axonal branches[49]. Mitochondrial transport is essential for axonal growth and branching, maintaining action potentials, and supporting synaptic transmission[49]. Aged and dysfunctional mitochondria need to be transported back to the cell body for degradation[50]. Defects in mitochondrial transport are associated with a variety of neurodegenerative disorders, including Parkinson's disease[49].

Early genetic screens identified the mitochondrial Rho GTPases Miro1 and Miro2 as essential factors regulating mitochondrial transport and quality control[51]. Miro1 is composed of two GTPase domains and two EF-hands that bind Ca^{2+}. Miro1 is localized to the outer mitochondrial membrane through its transmembrane domain[52,53], and is coupled to the C-terminus of the trafficking of kinesin-binding (TRAK) adaptors[54]. The N-terminal coiled-coil domain of TRAK1 and TRAK2 can separately bind to kinesin-1 and dynein-dynactin[52,55], which transport mitochondria towards the plus- and minus-ends of microtubules (MTs), respectively[55-57]. Co-immunoprecipitation studies showed that TRAK1 recruits both dynein and kinesin whereas TRAK2 primarily interacts with dynein[55]. TRAK1 was found to be enriched in the axons of cultured neurons, while TRAK2 was found mainly in dendrites[55], suggesting that these adaptors have nonredundant roles in mitochondrial trafficking.

Live cell imaging studies showed that mitochondria exhibit rapid anterograde and retrograde transport, interspersed with infrequent pausing and directional switching in axons and dendrites[58-

[61]. The complex transport properties of mitochondria are primarily driven by Miro1, TRAK adaptors, motors, and other associated factors[49], but little is known about how these components control mitochondrial directionality and pausing. In vitro reconstitution studies showed that TRAK1 binds and activates kinesin motility[62]. TRAK2 was also shown to recruit both kinesin and dynein and regulate their activity in cell extracts[63], but the underlying mechanism of how TRAK facilitates the activation and coordination of these opposing motors and mediates the transport of Miro1 is not well understood.

In mature neurons, two-thirds of mitochondria are docked to MTs[49]. Studies in cultured neurons demonstrated that mitochondrial transport stalls when local Ca^{2+} concentrations are elevated[56]. Yet a rise in the cytosolic Ca^{2+} concentration fails to halt mitochondrial transport when an EF-hand mutant of Miro1 is expressed in neurons and other cell types[53,64,65], indicating that Miro is the Ca^{2+} sensor that facilitates this process. However, the mechanism by which Ca^{2+} binding to Miro1 prevents motors from driving mitochondrial transport remains controversial[53,65,66]. The 'motor detachment' model proposes that Ca^{2+} binding to Miro1 decouples kinesin from TRAK[53]. In the 'Miro-binding' model, Ca^{2+} binding causes Miro1 to directly interact with the kinesin motor domain and inhibits its motility[65]. These models do not explain how elevated Ca^{2+} concentration also stops the retrograde mitochondrial transport driven by dynein. In addition, knockdown of both Miro1 and Miro2 does not completely suppress Ca^{2+}-induced arrest of mitochondria in neurons[64,67], suggesting that the Ca^{2+}-mediated arrest may function independently of the transport machinery. Recent studies in mouse models proposed an alternative model, in which a mitochondrial docking protein, syntaphilin (SNPH) anchors mitochondria to MTs in axons[66]. SNPH is recruited to mitochondria in response to sustained neuronal activity and elevated Ca^{2+} levels[66]. This model is supported by the observations that overexpression of SNPH completely abolishes mitochondrial transport in both directions and that increasing cytosolic Ca^{2+} fails to arrest mitochondrial transport in axons of SNPH knock-out neurons[66,68]. The "engine-switch and brake" model proposes that SNPH inhibits kinesin through direct molecular interaction and serves as a brake by anchoring mitochondria to MTs[68]. The predictions of these models could not be directly tested in vitro due to the lack of reconstituted assays from purified components.

In this study, we investigated the role of Miro1 and TRAK in the recruitment and activation of dynein and kinesin motility using *in vitro* reconstitution. We show that TRAK1 and TRAK2 activate dynein-dynactin motility. TRAK1 also increases the kinesin landing rate onto MTs but the MT-associated protein MAP7 is required to stimulate robust kinesin motility. TRAK1 or TRAK2 can simultaneously recruit dynein-dynactin and kinesin and these complexes are exclusively transported to the plus-end of MTs by kinesin. In comparison, kinesin does not colocalize to the TRAK adaptors transported to the minus-end by dynein/dynactin, demonstrating that TRAK coordinates the activity of opposing motors to avoid futile tug-of-war. We also distinguished between the predictions of the existing models of Ca^{2+}-mediated stalling of mitochondrial transport. Miro1 stably interacts with kinesin/TRAK, and the motility of this complex is unaffected by excess Ca^{2+}. However, static anchoring by SNPH is sufficient to stall kinesin or dynein motility. These results provide insight into the regulation of mitochondrial transport.

2.3 Results

2.3.1 TRAK1 and TRAK2 are activating adaptors of dynein-dynactin

Recent studies have identified a family of coiled-coil adaptor proteins that activate dynein motility by recruiting one or two dynein motors to dynactin[13,69]. Sequence alignments with established dynein adaptors confirmed that TRAK1 and TRAK2 contain the CC1 box that binds the dynein light-intermediate chain (LIC)[69,70] and the Spindly motif that interacts with the pointed-end of dynactin[71] **(Fig. 2.1a,b)**. We first investigated whether human TRAK1/2 could activate mammalian dynein-dynactin for processive motility using single-molecule imaging *in vitro* **(Fig. 2.2a)**. In the absence of TRAK, dynein-dynactin exhibited little to no motility, as previously shown[72,73] **(Fig. 2.2b)**. Remarkably, the N-terminal coiled coils of TRAK1/2 that contain both the CC1 box and the Spindly motif (TRAK1$^{1\text{-}400}$ and TRAK2$^{1\text{-}400}$) led to robust activation of dynein-dynactin motility towards the MT minus-end **(Fig. 2.1c,d and Fig. 2.2b)**. The velocities of dynein-dynactin-TRAK1$^{1\text{-}400}$ (DDT$_1$$^{1\text{-}400}$), and -TRAK2$^{1\text{-}400}$ (DDT$_2$$^{1\text{-}400}$) complexes (810 ± 20 and 870 ± 20 nm s^{-1}, mean ± s.e.m., respectively) were comparable to that of dynein-dynactin assembled with BicD adaptors in vitro[72-74] and the retrograde transport speed of mitochondria (300 – 900 nm s^{-1}) *in vivo*[55,60] **(Fig. 2.2c)**. In comparison, TRAK1/2 constructs that contain the CC1 box but lack the Spindly motif (TRAK1$^{1\text{-}360}$ and TRAK2$^{1\text{-}360}$) resulted in only occasional motility (**Fig. 2.1c,d)**, underscoring the importance of the Spindly motif in the activation of dynein-dynactin.

Multi-color tracking experiments visualized direct colocalization of motile dynein and TRAK adaptors **(Fig. 2.1e,f)**, demonstrating that TRAK needs to be part of the dynein-dynactin complex to sustain processive motility. The MT landing rate of active DDT$_1$$^{1\text{-}400}$ and DDT$_2$$^{1\text{-}400}$ complexes increased two-fold with the addition of 1 μM Lis1 (**Fig. 2.1c,d,f and Fig 2.2b)**, a dynein regulatory protein that facilitates the assembly of active dynein-dynactin-adaptor complexes[75-77]. Collectively, our results showed that TRAK1 and TRAK2 are activating adaptors of dynein-dynactin for mitochondrial transport **(Fig. 2.1g)**.

2.3.2 TRAK binding increases the frequency of kinesin motility

A previous study reported that the N-terminal coiled-coil domain of TRAK recruits the kinesin heavy chain[55]. In vitro pull-down assays using purified proteins revealed that full-length human kinesin-1 heavy chain (KIF5B, kinesin hereafter) binds to TRAK1$^{1\text{-}360}$, and to a lesser extent TRAK2$^{1\text{-}360}$ **(Fig. 2.3a and Fig. 2.4a)**. To determine how TRAK binding affects the activation and motility of kinesin, we performed single-molecule motility assays of kinesin with and without TRAK adaptors in vitro **(Fig. 2.3b-d)**. In the absence of TRAK, kinesin landed infrequently onto the MTs and did not walk along the MT **(Fig. 2.3b,c)**, consistent with autoinhibition of this motor[78]. In the presence of 5 nM TRAK1$^{1\text{-}360}$ or TRAK2$^{1\text{-}360}$, we only observed occasional motility of kinesin-TRAK (KT) complexes on MTs **(Fig. 2.3b,c)**. A previous study[62] reported activation of kinesin motility by a higher concentration (100-150 nM) of full-length TRAK1, but we observed little to no increase in kinesin landing rate by the addition of 20-100 nM TRAK1$^{1\text{-}360}$, suggesting that TRAK alone is insufficient to trigger robust activation of kinesin motility **(Fig. 2.3e)**.

We next asked whether TRAK adaptors more efficiently recruit kinesin when this motor is activated by its required cofactor, MAP7[79-81]. In vitro pull-down assays showed that kinesin binds more strongly to TRAK1$^{1\text{-}360}$ and TRAK2$^{1\text{-}360}$ in the presence of 10 nM MAP7 **(Fig. 2.3a)**. Consistent with previous reports[79-81], the landing rate and mobile fraction of kinesin increased 10-40 fold when we decorated MTs using 5 – 50 nM MAP7 in motility assays **(Fig. 2.3b,c)**. Under

the same MAP7 concentration, the addition of 5 nM TRAK1$^{1-360}$ increased the landing rate of kinesin- TRAK1$^{1-360}$ complexes (KT$_1$$^{1-360}$) about 1.5-fold compared to the no TRAK condition, while we did not observe a significant increase in the presence of 5 nM TRAK2$^{1-360}$ **(Fig. 2.3b,c)**. Similarly, the landing rate and percent colocalization of TRAK1$^{1-360}$ and TRAK2$^{1-360}$ adaptors to processive kinesins increased under higher MAP7 concentrations, with TRAK1$^{1-360}$ colocalizing with kinesin more efficiently than TRAK2$^{1-360}$ **(Fig. 2.4b)**. We also observed the comigration of longer (TRAK1$^{1-400}$ and TRAK2$^{1-400}$) and full-length (TRAK1$^{1-953}$ and TRAK2$^{1-914}$) TRAK constructs with kinesin on MTs **(Fig. 2.4c-e).** However, the landing rate of KT complexes assembled with full-length TRAK was noticeably infrequent than those formed by shorter TRAK constructs that lack its C-terminus, consistent with a previous report that the C-terminus of TRAK reduces the affinity between the N-terminal coiled-coil and kinesin[55].

We also tested whether an increase in TRAK concentration can lead to more robust kinesin motility in the presence of MAP7. Compared to the condition without TRAK, the addition of 20 nM TRAK1$^{1-360}$ increased the kinesin landing rate by 5-fold, whereas the addition of 100 nM TRAK2$^{1-360}$ resulted in a modest increase (30%) **(Fig. 2.3e,f)**. Collectively, our results show that the coiled-coil domain of TRAK1, and to a lesser extent TRAK2, efficiently recruits kinesin when the motor is rescued from autoinhibition by MAP7 **(Fig. 2.3g)**.

Kinesin motors co-localized with TRAK adaptors moved at similar velocities but exhibited higher run lengths than kinesin alone **(Fig. 2.3d)**. A previous study also reported longer run lengths for kinesin transporting full-length TRAK1 and attributed this increase in processivity to the interaction of the TRAK1 C-terminus with MTs[62]. We also observed MT binding of 150 nM TRAK1$^{1-360}$ and a TRAK1 construct containing the coiled coils and part of the C-terminal domain (TRAK1$^{1-532}$) in the absence of kinesin. However, the affinity of TRAK for MTs was weak and we could not detect MT binding of TRAK1$^{1-360}$, TRAK1$^{1-532}$, or full-length TRAK1 when TRAK concentration was lowered to 20 nM **(Fig. 2.5)**. Because kinesin run length increases when it transports a TRAK construct that lacks its C-terminus (TRAK1$^{1-360}$) at low TRAK concentrations **(Fig. 2.3d)**, we concluded that KT processivity increases even without MT binding of the TRAK C-terminus.

2.3.3 TRAK simultaneously recruits dynein-dynactin and kinesin

To test whether dynein and kinesin can colocalize to the same TRAK adaptor, we performed three-color imaging of dynein-dynactin, kinesin, and either TRAK1$^{1-400}$ or TRAK2$^{1-400}$. We observed dynein-dynactin/kinesin/TRAK1$^{1-400}$ (DDKT$_1$$^{1-400}$) colocalizers moving along the MT **(Fig. 2.6a,b)**. The likelihood of detecting dynein and kinesin to simultaneously colocalize on TRAK2$^{1-400}$ was substantially lower, presumably because kinesin has a low affinity for TRAK2 **(Fig. 2.6c,d)**. The analysis of these trajectories revealed that all DDKT$_1$$^{1-400}$ and DDKT$_2$$^{1-400}$ assemblies moved towards the MT plus-end at similar velocities to KT$_1$$^{1-400}$ and KT$_2$$^{1-400}$ complexes in the same chamber **(Fig. 2.6b, 2.7d and Fig. 2.7b)**. The velocity of DDKT$_1$$^{1-400}$ and DDKT$_2$$^{1-400}$ complexes were substantially higher than the case in which kinesin and dynein engage in a tug-of-war on an artificial DNA scaffold[74,82,83], indicating that dynein is not competing against kinesin-driven motility when both motors are recruited by TRAK.

We next investigated why DDKT complexes exclusively move towards the plus-end. We first tested different concentrations of MAP7, which activates full-length kinesin, while reducing the landing rate of dynein motility[82]. Without MAP7, we predominantly observed DDT motility, and a small number of KT or DDKT complexes on MTs when we used either TRAK1$^{1-400}$ **(Fig. 2.6a,b)**

or TRAK2$^{1-400}$ **(Fig. 2.7a,b)**. In contrast, at 5 and 10 nM MAP7, we mostly observed processive runs of KT complexes on MTs **(Fig. 2.6e and Fig. 2.7b)** and a slight reduction in the landing rate of active DDT complexes. Importantly, in all MAP7 concentrations we tested, both DDKT$_1^{1-400}$ and DDKT$_2^{1-400}$ complexes always moved toward the plus-end **(Fig. 2.6b)**. Thus, the concentration of MAP7 acts to tune bidirectional motility by activating kinesin and interfering with dynein motility, but it does not affect the directionality of DDKT complexes. We also tested whether dynein more efficiently competes against kinesin when its assembly with dynactin and TRAK is aided by Lis1$^{75-77}$. The addition of 1 μM Lis1 increased the landing rate of both DDT$_1^{1-400}$ and DDT$_2^{1-400}$ without affecting kinesin motility. However, the Lis1 addition had only a minor effect on the landing rate of complexes containing both motors, and no effect on their directional preference **(Fig. 2.7c,d)**, ruling out this possibility.

We also considered the possibility that the direction of DDKT motility is driven by higher force generation of kinesin compared to single dynein **(Fig. 2.6)**. To test this possibility, we replaced full-length kinesin with a kinesin tail construct that binds to TRAK but lacks the motor domain needed for plus-end directed motility and force generation (KIF5B$^{\Delta 1-336}$). If the direction of DDKT is determined by mechanical competition, we expected DDKT$_1^{1-400}$ complexes assembled with KIF5B$^{\Delta 1-336}$ to move towards the minus end. However, the addition of excess KIF5B$^{\Delta 1-336}$ only resulted in more than a 5-fold reduction in DDT$_1^{1-400}$ landing rate **(Fig. 2.6f,g)**, but we did not observe any KIF5B$^{\Delta 1-336}$ colocalizing with processive DDT$_1^{1-400}$ complexes moving towards the minus end. These results indicate that when kinesin transports TRAK, dynein-dynactin cannot form an active motor, but it can be transported by kinesin towards the plus-end as an inactive motor. In comparison, kinesin is excluded from binding to a TRAK adaptor actively transported by dynein-dynactin towards the minus-end **(Fig. 2.6h)**.

2.3.4 Miro1 forms a complex with kinesin, dynein, and TRAK

We next turned our attention to the association of Miro1 with the KT and DDT complexes. Miro1 was shown to interact separately with TRAK adaptors and kinesin in immunoprecipitation assays[52,53,65], but it remained unclear which of these interactions form a stable complex capable of plus-end directed transport. To address this question, we expressed a soluble Miro1 construct lacking its transmembrane domain (Miro1$^{1-592}$, Miro1 hereafter; **Fig. 2.9a and Fig. 2.9a)**. We first tested whether Miro1 can interact with kinesin independent of TRAK, as previously reported[5]. In pull-down assays using purified components, kinesin pulled down TRAK but not Miro1 when we used TRAK1$^{1-360}$ and TRAK2$^{1-360}$ constructs that bind kinesin but lack the Miro1 interaction domain **(Fig. 2.8b)**. However, longer (TRAK1$^{1-532}$) or full-length TRAK constructs (TRAK1$^{1-953}$, TRAK2$^{1-914}$) co-precipitated with Miro1 **(Fig. 2.8c)**. These interactions were stable in the presence of a nonhydrolyzable GTP analog (GTPγS) or GDP **(Fig. 2.9b)**, indicating that Miro1's nucleotide state does not affect its association with TRAK[84]. Consistent with the pull-down assays, we observed little to no comigration of Miro1 with kinesin motors in the absence of a TRAK adaptor or the presence of 10 nM TRAK1$^{1-360}$ or TRAK2$^{1-360}$ **(Fig. 2.8d and Fig. 2.9c)**. Unlike TRAK1$^{1-360}$, TRAK1$^{1-532}$ and full-length TRAK1 facilitated the formation of frequent kinesin- TRAK1$^{1-532}$-Miro1 (KTM) complexes that walk along the MTs **(Fig. 2.8d-f and Fig. 2.9d,e)**. Collectively, these results show that kinesin does not strongly interact with Miro1 in the absence of a TRAK adaptor and that N-terminal 532 residues of TRAK is sufficient to establish a link between kinesin and Miro1.

The velocity and run length of KTM complexes were similar to KT complexes that do not colocalize with Miro1 **(Fig. 2.8f)**. We also observed dynein-dynactin assembled with $TRAK1^{1-532}$ to migrate with Miro1 in motility assays **(Fig. 2.8g and Fig. 2.9d)**. Similar to kinesin, the velocity and run length of DDT_1^{1-532} complexes that comigrate with Miro1 (DDTM) were similar to DDT_1^{1-532} only **(Fig. 2.8h)**. We concluded that Miro1 binding to TRAK1 does not substantially affect the assembly and motility of KT and DDT complexes.

2.3.5 Ca^{2+}-mediated arrest of the mitochondrial transport

We used our in vitro reconstitution assay to test the predictions of the models that explain how Ca^{2+} binding to Miro1 stalls mitochondrial transport. The motor detachment model[53] predicts that kinesin decouples from Miro1/TRAK in excess Ca^{2+} **(Fig. 2.10a)**. However, our in vitro immunoprecipitation assays showed that kinesin co-precipitated with $TRAK1^{1-532}$ and Miro1 in the absence or presence of physiological (100 nM) or excess (2 mM) Ca^{2+} **(Fig. 2.10b)**. Similarly, in the absence of Miro1, kinesin efficiently transports both $TRAK1^{1-360}$ and $TRAK2^{1-360}$ in motility assays, and the percentage of kinesins comigrating with TRAK remain unaffected by the addition of 2 mM Ca^{2+} **(Fig. 2.10c,d)**. In the presence of Miro1, kinesin and $TRAK1^{1-532}$ comigrated with Miro1 in 0, 0.1, and 2 mM Ca^{2+} **(Fig. 2.10e and Fig. 2.11a)**. The landing rate, velocity, and run length of KTM complexes in 2 mM Ca^{2+} **(Fig. 2.10f-g)** were similar to the no Ca^{2+} condition **(Fig. 2.8e,f)**. These results are inconsistent with the motor detachment model and show that Miro1 remains bound to the KT complex in the presence of Ca^{2+}.

The Miro-binding model predicts that Ca^{2+} binding causes Miro1 to directly interact with the kinesin motor domain and inhibit kinesin motility[17] **(Fig. 2.10h)**. We tested whether Miro1 directly binds and inhibits the motility of a kinesin construct that contains the motor domain but lacks the tail domain ($KIF5B^{1-490}$, **Fig. 2.11b**). Because $KIF5B^{1-490}$ is a constitutively active motor[79], these assays were performed in the absence of MAP7. Unlike full-length kinesin, Miro1 did not co-precipitate with $KIF5B^{1-490}$ in the presence or absence of Ca^{2+} **(Fig. 2.10i)**. In motility assays, $KIF5B^{1-490}$ did not comigrate with Miro1 in the presence or absence of Ca^{2+} **(Fig. 2.10j and Fig. 2.11c).** In addition, the landing rate of $KIF5B^{1-490}$ on MTs remained unaffected by the addition of Miro1 and 2 mM Ca^{2+} **(Fig. 2.10k)**. Collectively, our results are inconsistent with the Miro-binding model and show that Miro1 does not bind and inhibit the kinesin motor domain in response to elevated Ca^{2+}.

Finally, we tested the models that propose Ca^{2+}-mediated accumulation of SNPH to the outer mitochondrial membrane to inhibit both anterograde and retrograde transport of mitochondria[66,68]. The "engine-switch and brake" model predicts that SNPH inhibits kinesin through direct molecular interaction[68] **(Fig. 2.13a)**. To test this model, we expressed an SNPH construct that lacks the C-terminal transmembrane domain ($SNPH^{1-473}$, **Fig. 2.12a**). We did not observe strong interactions between kinesin and SNPH in immunoprecipitation assays **(Fig. 2.12b).** In motility assays, we confirmed that SNPH densely decorates the MT surface[66] **(Fig. 2.13b)**. According to the "engine-switch and brake" model, decoration of the MT surface by SNPH would increase the kinesin landing rate but prevent subsequent motility. However, kinesin was able to walk along the MT even in the presence of 1 μM SNPH, indicating that SNPH does not inhibit kinesin motility through direct interactions. We note that the addition of SNPH substantially decreased the kinesin landing rate to MTs and slowed down subsequent motility **(Fig. 2.13b-d)**, raising the possibility that MT

binding of SNPH may reduce MT recruitment and velocity of kinesin similar to MT-associated proteins (MAPs)[85].

The "static anchor" model predicts that SNPH can induce resistive forces against motility by passively anchoring mitochondria to MTs **(Fig. 2.13a)**[66,86]. To test this prediction, we immobilized kinesin and SNPH to the glass surface and asked how MT binding of SNPH affects MT gliding activity of kinesin and dynein motors **(Fig. 2.13e)**. Consistent with this model, the addition of SNPH slowed down gliding motility driven by kinesin **(Fig. 2.13f-g)** and DDT_1^{1-400} in a dose-dependent manner **(Fig. 2.13h,i)**. MT gliding was almost completely stopped when we incubated the glass surface with excess (1-2 μM) SNPH **(Fig. 2.13g and Fig. 2.12c,d)**, suggesting that multiple SNPH molecules may be required to efficiently counter either motor. These results support the model that SNPH inhibits both anterograde and retrograde transport of mitochondria by passively anchoring mitochondria to MTs[66,68].

2.4 Discussion

In this study, we used in vitro reconstitution to demonstrate that kinesin and dynein transport Miro1/TRAK1 towards the plus- and minus-ends of MTs. Our work provides an explanation for how opposing actions of kinesin and dynein might be regulated by TRAK adaptors to control the directionality of mitochondrial transport. Using our in vitro reconstitution assay, we also directly tested the predictions of the models that describe how mitochondrial transport is arrested at regions of elevated Ca^{2+} **(Fig. 2.14)**. We showed that TRAK1 and TRAK2 are bona fide adaptors that activate the motility and force generation of dynein-dynactin. Consistent with studies in neurons[55], TRAK1, and to a lesser extent TRAK2, recruit kinesin, but TRAK binding is not sufficient to substantially activate kinesin-1 for processive motility. We observed that MAP7 decoration of MTs promoted the motility of KT complexes, highlighting the necessity of MAP7 for most, if not all, kinesin-1 driven transport in various cell types[78,87]. In the presence of MAP7, kinesin binding to TRAK1 increased its MT landing rate and run length. In addition, an increase in TRAK concentration stimulated more frequent kinesin motility at a given MAP7 concentration, indicating that TRAK binding may increase the stability of the active conformation of kinesin once this motor is activated by MAP7. These results are in agreement with a recent in vitro reconstitution study[88], which showed that kinesin-1 employs a two-step activation process that involves binding to a cargo adaptor and interacting with MAP7 on MTs.

Our results are largely consistent with recent reports that studied kinesin and dynein-mediated transport of TRAK1 and TRAK2 adaptors in vitro. Similar to our results, Henrichs et al. showed that full-length TRAK1 activates kinesin motility and increases the motor run length[62]. This study has reported activation of kinesin by full-length TRAK1 without MAP7[62]. While we also observed occasional processive runs of kinesin by TRAK1 addition in the absence of MAP7, the landing rate of these runs was ~40-fold lower compared to the addition of both TRAK1 and MAP7. Henrichs et al. also attributed the increase in the processivity of KT complexes to the interaction of the TRAK1 C-terminus with MTs[62]. However, we observed that TRAK1 only weakly interacts with MTs at high concentrations, consistent with the lack of strong MT localization of TRAK adaptors in cells[55]. We also observed that TRAK binding increases kinesin run length even in the absence of the TRAK1 C-terminus.

More recently, Fenton et al. reported TRAK2-mediated activation of kinesin and dynein-dynactin motility in cell extracts and observed that TRAK2 adaptors that recruit both kinesin and dynein exclusively moved towards the MT plus-end[63]. We also observed our reconstituted DDKT complexes to exclusively move towards the plus-end at speeds comparable to kinesin, indicating that dynein is transported as an inactive passenger by kinesin on TRAK adaptors **(Fig. 14)**. This is consistent with the observation that mitochondria move at similar speeds to kinesin in an anterograde direction[89] even though dynein is localized to these cargos[90,91]. Fenton et al. reported that the knockdown of either kinesin or dynein also results in a decrease in the frequency of TRAK2 transport in the opposite direction[63], indicating that TRAK binding of one motor increases the affinity of the other motor to the same TRAK adaptor. Our results are not fully consistent with this view, because we did not observe dynein transporting kinesin towards the minus-end. Instead, the assembly of the active DDT complexes was mutually exclusive with kinesin binding to the TRAK adaptor. While we cannot exclude the possibility that our purified system lacks additional factors that link these motors together on TRAK, these observations suggest that retrograde transport of Miro1/TRAK requires dissociation of kinesin and formation of active dynein-dynactin complex on TRAK **(Fig. 2.14)**. Our results do not exclude the possibility that kinesin remains bound to retrogradely moving mitochondria by interacting with other mitochondrial adaptor proteins and these possibilities remain to be tested by tracking the association of motor proteins with anterogradely and retrogradely transported mitochondria in live cells[92].

The motility of DDKT complexes was markedly different from the reconstituted kinesin-3/Hook3/dynein-dynactin complex[93]. Unlike DDKT, complexes assembled with Hook3 move either towards the plus- or minus-end of the MT at speeds lower than kinesin or dynein alone[93], suggesting that the presence of the opposing motor slows down the motility of the active motor. These differences may be attributed to whether kinesin and dynein motors interact with each other when they are bound to the same adaptor. While kinesin-3 and dynein bind to distant sites on Hook3[93], kinesin-1 and dynein may have overlapping binding sites on TRAK. Although the kinesin binding site on TRAK1 has not been well characterized, the coiled-coil between the CC1 box and the Spindly motif (amino acids 100-360) of TRAK1 was sufficient to co-precipitate with kinesin[55]. Based on the structures of dynein-dynactin assembled with BicD or Hook family adaptors[16,94], this entire region is expected to run from the pointed to the barbed end of dynactin in active DDT complexes. If kinesin has a smaller footprint on TRAK, it may block some of the pairwise interactions required for the formation of the active DDT complex, but not fully inhibit the binding of dynein and dynactin to the rest of this coiled-coil. In comparison, activation of the DDT complex may block the entire kinesin binding site, and thereby, exclude kinesin from motile DDT complexes. Alternatively, TRAK may coordinate motor binding through a registry shift of its coiled coils, as proposed for the BicD2 adaptor[95]. These possibilities could be best distinguished by future cryo-electron imaging of reconstituted DDKT complexes at near-atomic resolution.

The in vitro reconstitution assay we developed enabled us to directly test the predictions of the models that describe how elevated levels of intracellular Ca^{2+} arrest mitochondrial transport. We first tested whether Miro1 dissociates from or inhibits the KT complexes in the presence of excess Ca^{2+}. The assembly and motility of the KTM complexes were unaffected by increased Ca^{2+} levels, which is incompatible with both 'motor detachment' and 'Miro binding' models[53,65]. Our results indicate that Ca^{2+} binding to Miro1 does not directly disrupt the machinery that transports mitochondria, and thereby Ca^{2+}-mediated docking of mitochondria might occur upstream of the motor transport machinery **(Fig. 2.6)**. However, we provided evidence that the MT anchoring

protein SNPH is sufficient to stall the MT gliding activity of kinesin and dynein motors, consistent with overexpression of this protein to fully inhibit mitochondrial transport in both directions[66].

We note that our results do not discount the role of Miro1 to coordinate the arrest of mitochondrial transport. Miro1 may serve as the primary factor that facilitates Ca^{2+}-mediated recruitment of SNPH[66] and other associated factors to the outer mitochondrial membrane. In particular, the dynein-interacting protein Disrupted in Schizophrenia 1 (DISC1)[96], Armadillo repeat-containing X-linked (Armcx) 1 and 3[97,98], and mitochondrial fusion proteins MFN1 and MFN2 have been shown to interact with the Miro1/TRAK complex, and knockdown of these factors led to defects in mitochondrial transport[92]. The in vitro reconstitution assay we developed provides an experimental platform to investigate the molecular mechanism of how these factors regulate mitochondrial transport.

2.5 Figures

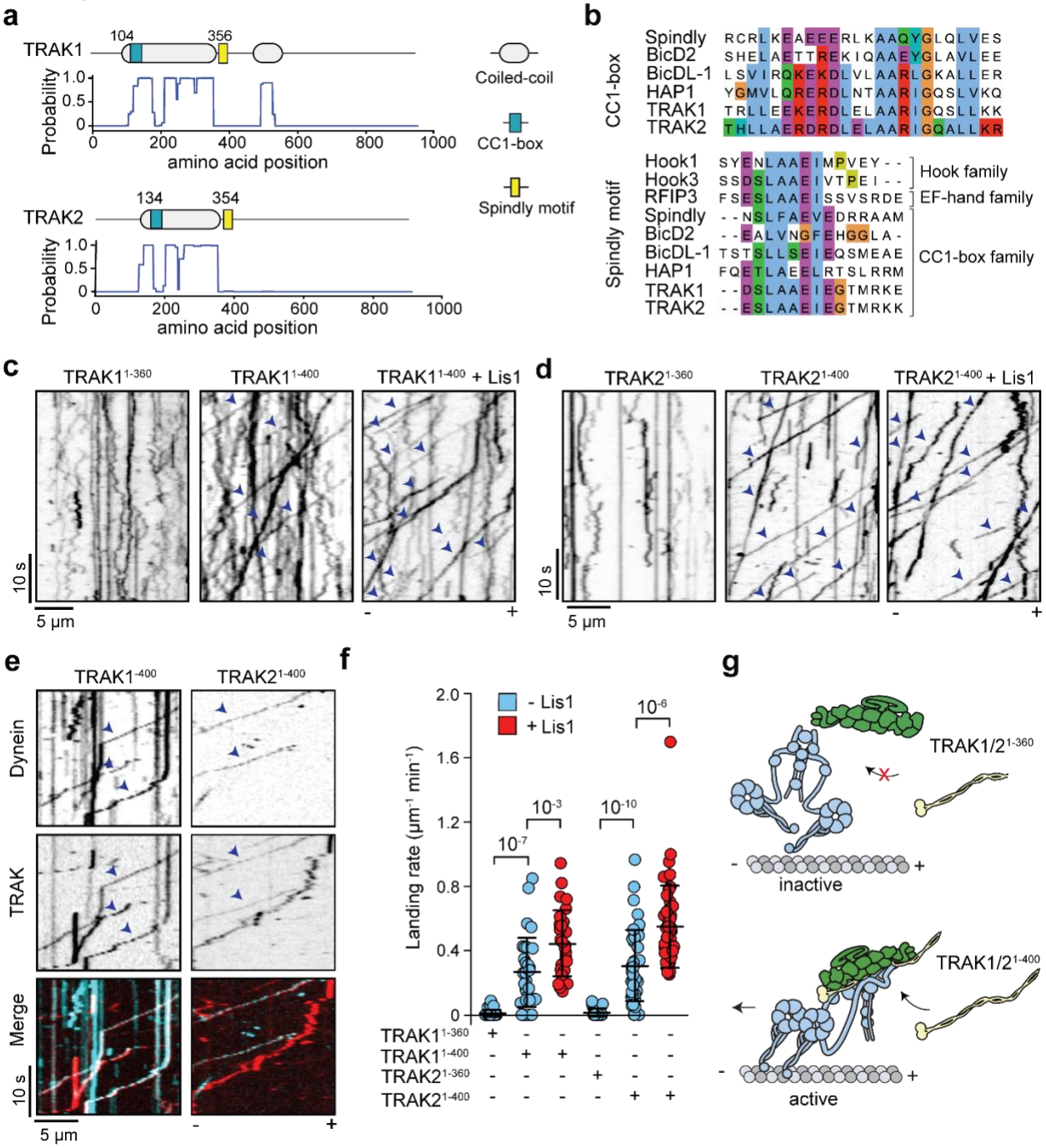

Fig. 2.1. TRAK coiled-coil domains activate dynein-dynactin motility. a. Domain organization and coiled-coil prediction score of human TRAK1 and TRAK2. **b.** Sequence alignment shows the conserved CC1 box (top) and the Spindly motif (bottom) of TRAK1 and TRAK2 with other activating adaptors of human dynein-1. The sequences were aligned using the Clustal Omega algorithm. **c-d.** Representative kymographs of TRAK1 (**c**) and TRAK2 (**d**) constructs labeled with the LD655 dye in the presence of unlabeled dynein/dynactin (DD) with or without 1 µM Lis1. Arrowheads highlight processive motility. **e.** Representative kymographs of LD655-dynein and

LD555-TRAK constructs in the presence of unlabeled dynactin. Arrowheads represent TRAK-dynein colocalization. The processive motility of TRAK not colocalizing with dynein is due to less than 100% labeling efficiency of dynein. **f.** The landing rate of motor complexes on MTs. The centerline and whiskers represent mean and s.d., respectively (n = 30, 32, 31, 31, 44, and 48 MTs from left to right). P values are calculated from a two-tailed t-test. **g.** TRAK is an activating adaptor of dynein-dynactin. Activation of dynein motility requires both the CC1 box and the Spindly motif in the TRAK coiled-coil.

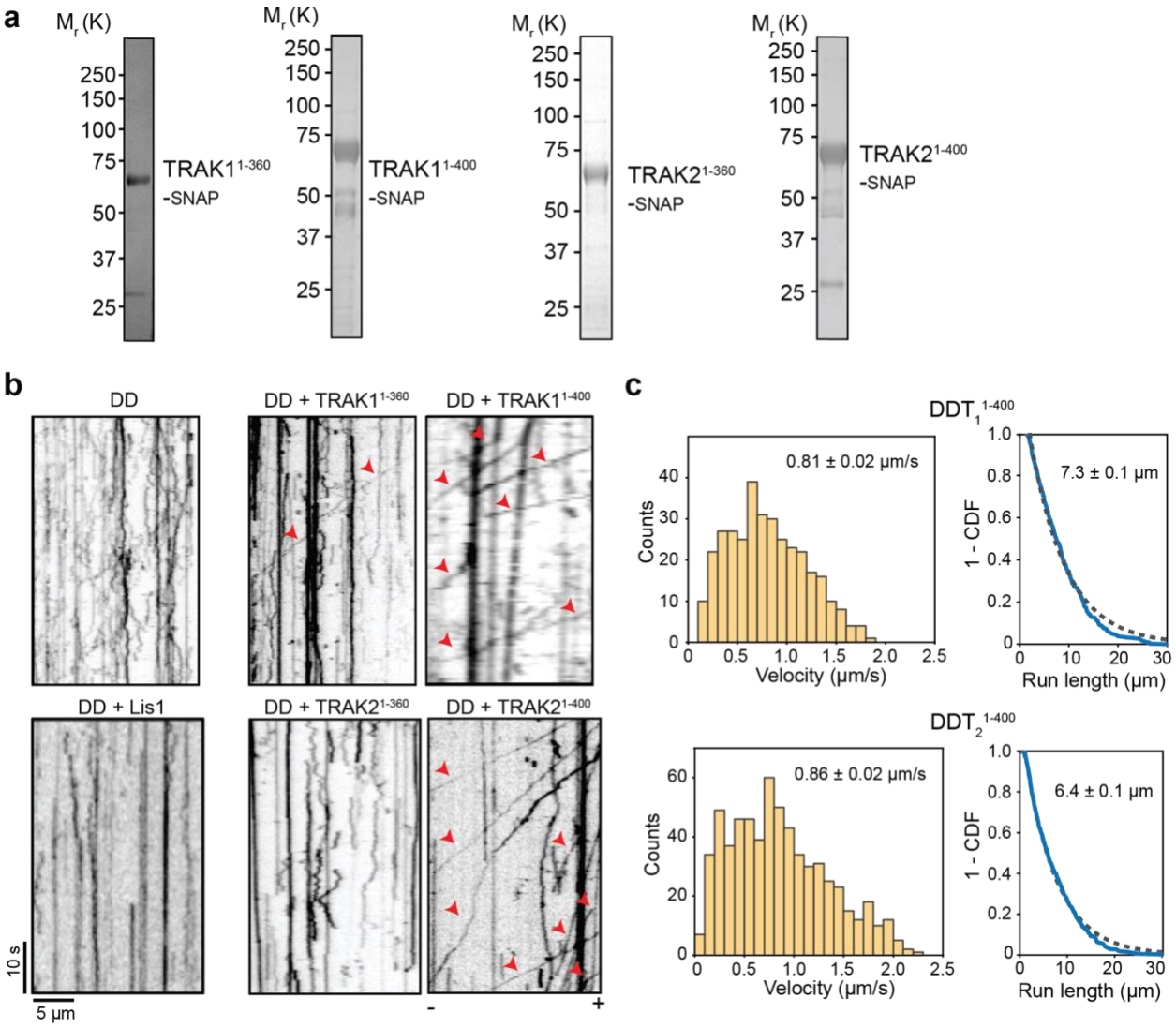

Fig. 2.2. Purification and motility of DDT complexes. a. Coomassie-stained denaturing gel of purified TRAK constructs. **b.** Representative kymographs of LD655-dynein in the presence of unlabeled dynactin and TRAK1 or TRAK2 constructs in 2 mM ATP. Arrowheads highlight processive complexes. DD and DD+Lis1 only exhibit weak microtubule binding and diffusion along the microtubule surface in the absence of a TRAK adaptor. **c.** Velocity histograms (mean ± s.e.m.) and 1-CDF of run length for DDT$_1^{1-400}$ (n = 341 molecules from three independent

experiments) and $DDT_2^{1\text{-}400}$ (n = 630 molecules from three independent experiments). Fits to a single exponential decay (dashed curves) reveal the motor run lengths (±s.e.).

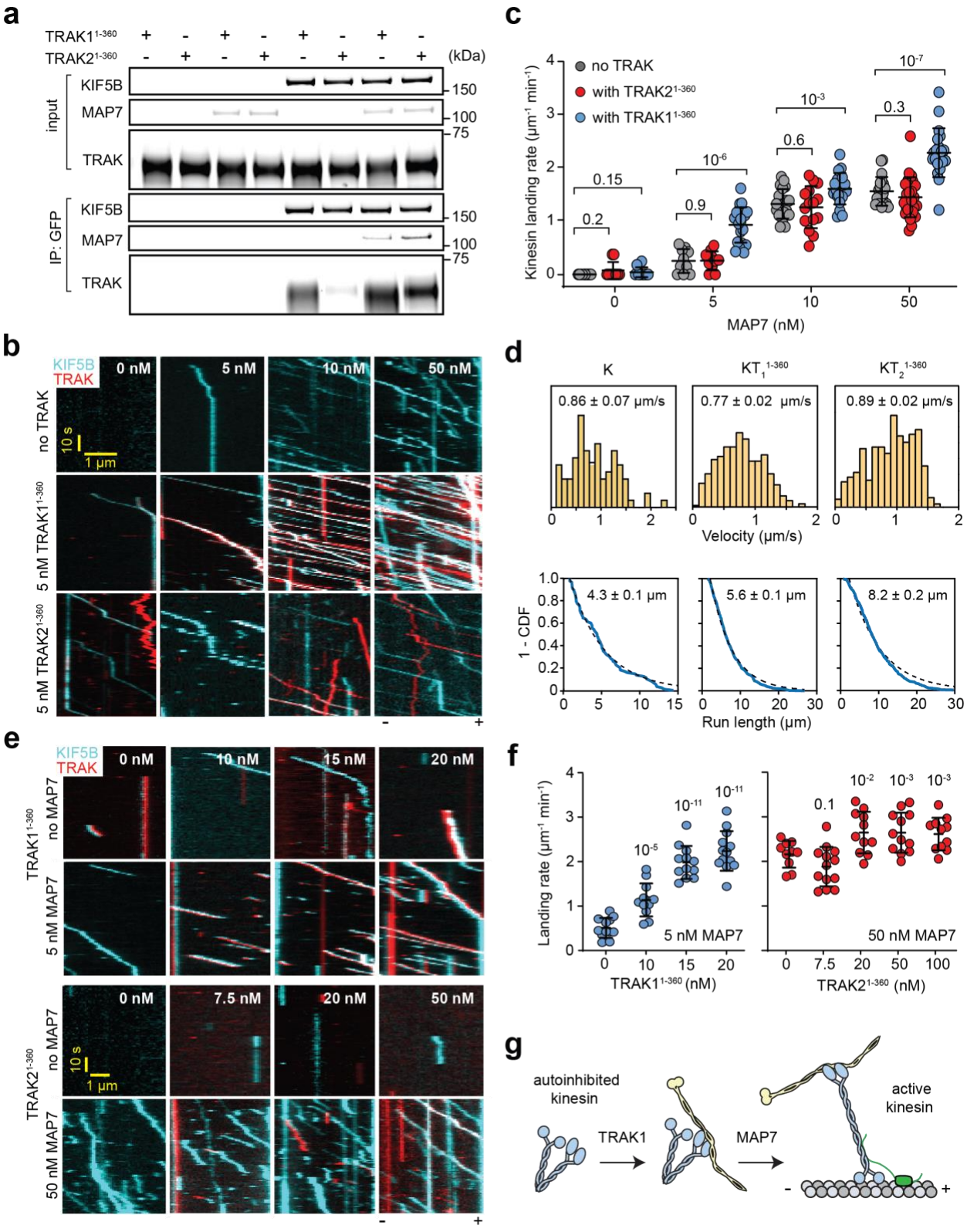
a
TRAK1 1-360
TRAK2 1-360
(kDa)
input
IP: GFP
KIF5B
MAP7
TRAK
150
100
75
b
KIF5B
TRAK
0 nM
5 nM
10 nM
50 nM
no TRAK
5 nM TRAK1 1-360
5 nM TRAK2 1-360
10 s
1 µm
c
no TRAK
with TRAK2 1-360
with TRAK1 1-360
Kinesin landing rate (µm-1 min-1)
MAP7 (nM)
0.2
0.15
0.9
10-6
0.6
10-3
0.3
10-7
d
K
KT1 1-360
KT2 1-360
0.86 ± 0.07 µm/s
0.77 ± 0.02 µm/s
0.89 ± 0.02 µm/s
Velocity (µm/s)
1 - CDF
4.3 ± 0.1 µm
5.6 ± 0.1 µm
8.2 ± 0.2 µm
Run length (µm)
e
KIF5B
TRAK
0 nM
10 nM
15 nM
20 nM
TRAK1 1-360
no MAP7
5 nM MAP7
0 nM
7.5 nM
20 nM
50 nM
TRAK2 1-360
no MAP7
50 nM MAP7
10 s
1 µm
f
Landing rate (µm-1 min-1)
10-5
10-11
10-11
0.1
10-2
10-3
10-3
5 nM MAP7
50 nM MAP7
TRAK1 1-360 (nM)
TRAK2 1-360 (nM)
g
autoinhibited kinesin
TRAK1
MAP7
active kinesin

Fig. 2.3. Kinesin recruits TRAK adaptors more efficiently following activation by MAP7. a. In vitro immunoprecipitation (IP) of purified kinesin (KIF5B-GFP-SNAPf), TRAK1$^{1\text{-}360}$, and TRAK2$^{1\text{-}360}$ in the presence or absence of 10 nM MAP7. The proteins were eluted from anti-GFP beads. **b.** Representative two-color kymographs of KIF5B and TRAK constructs with increasing concentrations of MAP7. The processive motility of TRAK not colocalizing with kinesin is due to less than 100% labeling of kinesin. **c.** The landing rate of kinesin in the absence and presence of 5 nM TRAK1$^{1\text{-}360}$ or TRAK2$^{1\text{-}360}$ under increasing MAP7 concentrations a(n = 10, 10, 10, 10, 10, 20, 20, 15, 20, 20, 25, and 20 MTs from left to right, two independent trials). **d.** (Top) Velocity histogram (mean ± s.e.m.) and (Bottom) the inverse cumulative distribution function (1-CDF) of motor run length for K (n = 88), KT$_1$$^{1\text{-}360}$ (n = 404), and KT$_2$$^{1\text{-}360}$ (n = 499, three independent experiments) in 10 nM MAP7. Fits to a single exponential decay (dashed curves) reveal the motor run length (±s.e.). **e.** Representative two-color kymographs of LD555-kinesin with increasing concentrations of LD655-labeled TRAK1$^{1\text{-}360}$ or TRAK2$^{1\text{-}360}$ in the presence or absence of MAP7. A higher MAP7 concentration (50 nM) was used for TRAK2 because kinesin runs remained infrequent at a lower MAP7 concentration (5 nM). **f.** The landing rate of kinesin with increasing concentrations of TRAK adaptors. The centerline and whiskers represent mean and s.d., respectively (n = 12, 12, 12, 13, 10, 13, 11, 12, and 11 MTs from left to right, three independent trials). **g.** TRAK recruits kinesin, but activation of KT motility requires a kinesin-1 cofactor, MAP7. In (**c**) and (**f**), the center line and whiskers represent the mean and s.d., respectively. P-values are calculated from a two-tailed t-test. In (**f**), P-values are calculated in comparison to the no TRAK condition.

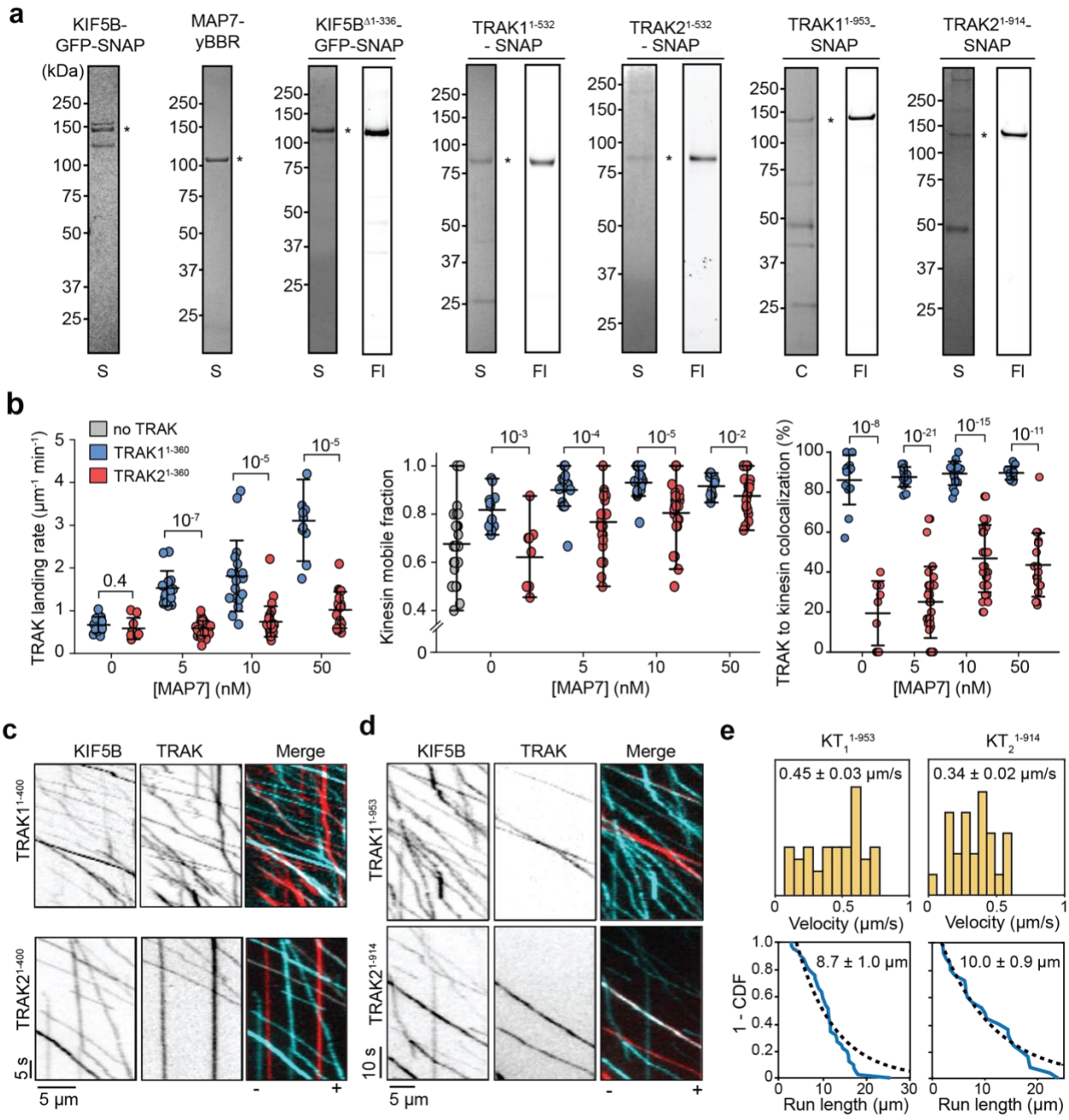

Fig. 2.4. Purification and motility of KT complexes. a. Denaturing gel pictures of purified KIF5B, MAP7, and TRAK constructs. Stars indicate the expected molecular weight (C: Coomassie-stained, S: silver-stained; Fl: fluorescence image scan). The SNAP tags of kinesin and TRAK were labeled with Alexa488 and LD555 for fluorescence imaging, respectively. **b.** (Left) The landing rate of TRAK adaptors, (Middle) the mobile fraction of kinesin motors landed on MTs, and (Right) the percentage of TRAK colocalization to processive kinesin motors moving along the MTs in the absence and presence of 5 nM TRAK1$^{1\text{-}360}$ or TRAK2$^{1\text{-}360}$ under increasing MAP7 concentrations. The center line and whiskers represent the mean and s.d., respectively (n = 26, 13, 14, 18, 12, 9, 22, 29, and 19 MTs from left to right, three independent trials). P values are calculated from a two-tailed t-test. **c.** Representative kymographs of LD555-kinesin and LD655-

labeled TRAK1$^{1\text{-}400}$ or TRAK2$^{1\text{-}400}$ in 10 nM MAP7. **d.** Representative kymographs of LD555-kinesin and LD655-labeled full-length TRAK1$^{1\text{-}953}$ or TRAK2$^{1\text{-}914}$ in 10 nM MAP7. **e.** (Top) Velocity histogram (mean ± s.e.m.) and (Bottom) 1-CDF of run length for kinesin carrying full-length TRAK1 (KT$_1^{1\text{-}953}$; n = 41, three independent experiments) or full-length TRAK2 (KT2$^{1\text{-}914}$; n = 25, three independent experiments). Fits to a single exponential decay (dashed curves) reveal the motor run length (±s.e.).

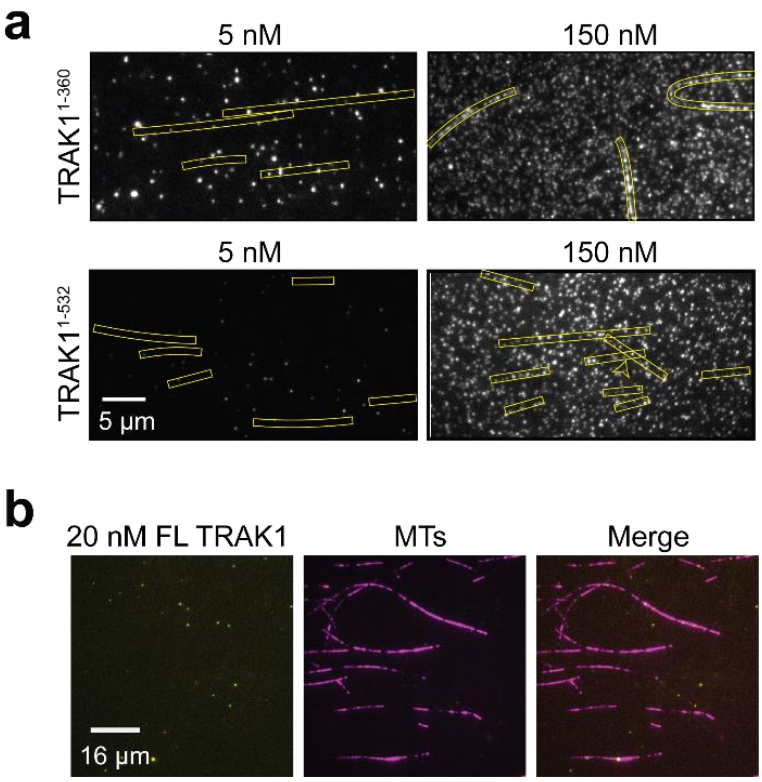

Fig. 2.5. TRAK weakly interacts with MTs. a. Sample images show localization of 5 nM and 150 nM TRAK1$^{1\text{-}360}$ or TRAK1$^{1\text{-}532}$ on surface-immobilized MTs (highlighted in yellow) in the absence of kinesin (experiments were replicated three times per condition with reproducible results). **b.** Sample images show little to no binding of 20 nM full-length TRAK1$^{1\text{-}953}$ to surface-immobilized Cy5-MTs in the absence of kinesin (experiments were replicated three times per condition with reproducible results).

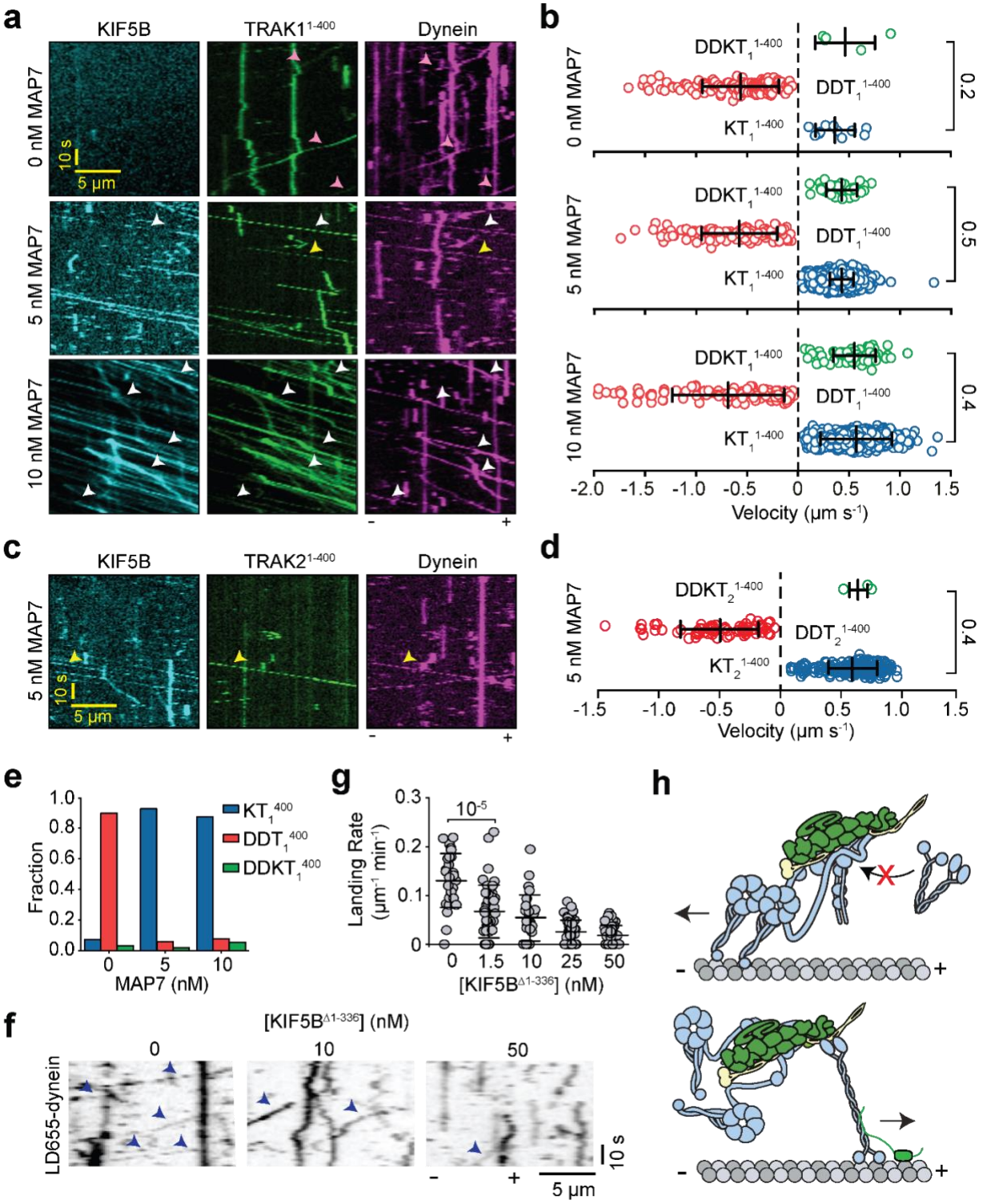

Fig. 2.6 TRAK adaptors simultaneously recruit dynein-dynactin and kinesin. a. Representative kymographs of Alexa488-kinesin, LD555-TRAK1$^{1\text{-}400}$, and LD655-dynein in the presence of 0, 5, and 10 nM MAP7. White arrowheads show colocalization of dynein, kinesin, and TRAK. Yellow arrowheads highlight the plus-end-directed movement of dynein and TRAK by

unlabeled kinesin. Magenta arrowheads represent the minus-end-directed movement of dynein and TRAK. **b.** The velocity distribution of complex assemblies at 0, 5, and 10 nM MAP7. Negative velocities correspond to minus-end-directed motility. (n = 5, 138, 11, 43, 130, 2104, 79, 117, and 1342 from top to bottom, three independent experiments per condition). **c.** Representative kymographs of Alexa488-kinesin, LD555-TRAK2$^{1\text{-}400}$, and LD655-dynein on a surface-immobilized MT in the presence of 5 nM MAP7. Assays were performed in the absence of Lis1. Yellow arrowheads show colocalization of dynein, kinesin, and TRAK2. **d.** The velocity distribution of complex assemblies at 5 nM MAP7 and 0 nM Lis1 (n = 3, 67, and 206 from top to bottom, three independent experiments per condition). **e.** The fraction of complexes formed with TRAK$_1^{1\text{-}400}$ under different MAP7 concentrations. **f.** Sample kymographs of 0.5 nM DDT1$^{1\text{-}400}$ assemblies in the presence of 1 μM Lis1 and increasing concentrations of KIF5B$^{\Delta 1\text{-}336}$. Processive runs of LD655-dynein are highlighted with blue arrowheads. **g.** The landing rates of 0.5 nM DDT$_1^{1\text{-}400}$ assemblies under increasing concentrations of KIF5B$^{\Delta 1\text{-}336}$ (n = 28, 45, 27, 50, and 51 MTs from left to right; two independent experiments per condition). **h.** Schematic representation of motor coordination on TRAK. When kinesin transports TRAK, dynein can remain as an inactive passenger, but kinesin is excluded from minus-end directed DDT complexes. In (**b**), (**d**), and (**g**), the center line and whiskers represent the mean and s.d., respectively. P-values are calculated from a two-tailed t-test.

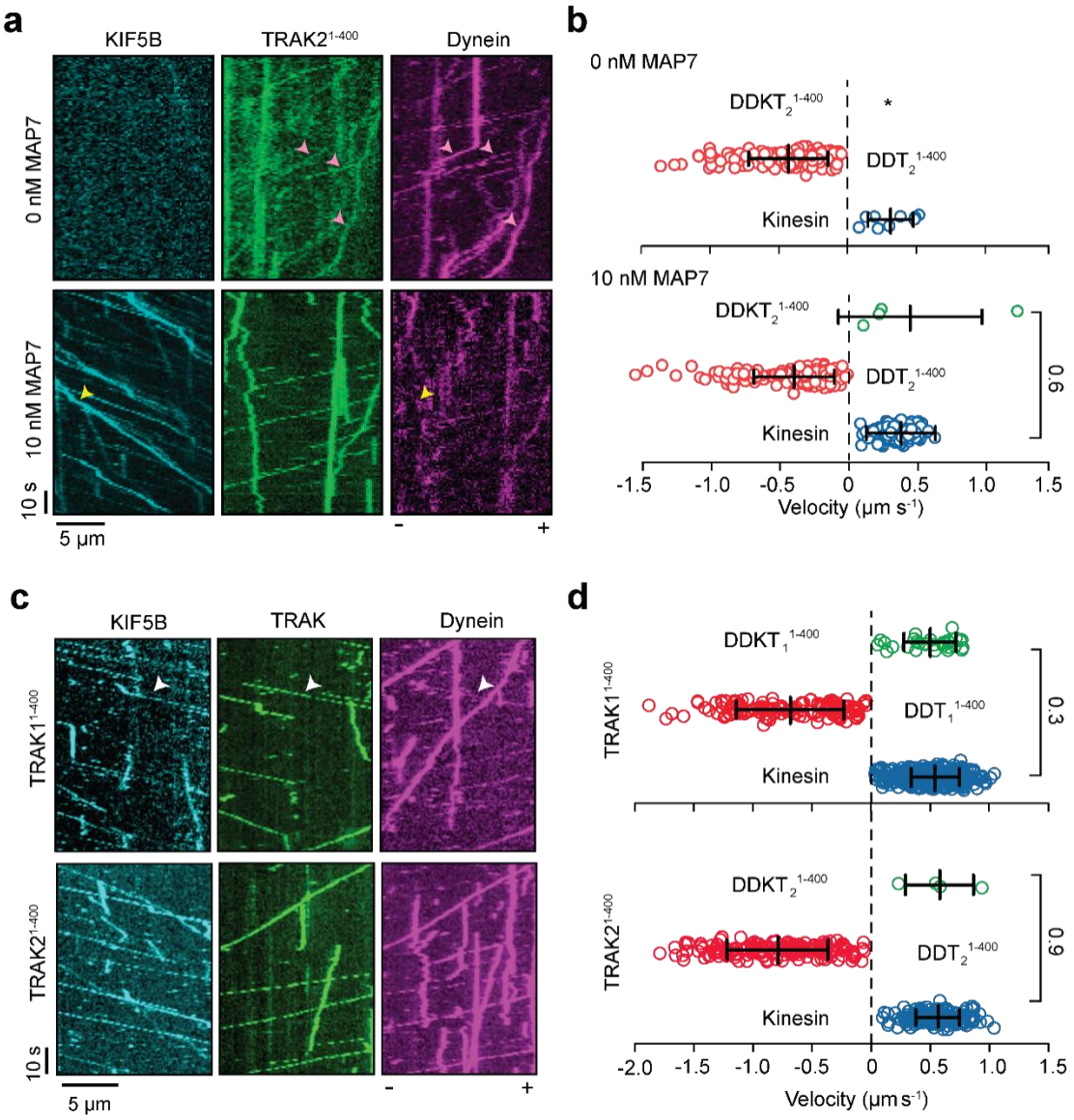

Fig. 2.7. Velocity of DDKT complexes in the presence and absence of Lis1. a. Representative kymographs of Alexa488-kinesin, LD555-TRAK2$^{1-400}$, and LD655-dynein on a surface-immobilized MT in the presence of 0 and 10 nM MAP7. Assays were performed in the absence of Lis1. Magenta arrowheads show the comigration of dynein and TRAK2, and yellow arrowheads show the comigration of dynein and kinesin towards the microtubule plus-end. **b.** The velocity distribution of individual motor complexes and DDKT assemblies at 0 and 10 nM MAP7 and 0 nM Lis1 (n = 0, 157, 9, 5, 180, and 234 from top to bottom, three independent experiments per condition). **c.** Representative kymographs of Alexa488-kinesin, LD555-TRAK1$^{1-400}$ or -TRAK2$^{1-400}$, and LD655-dynein on a surface-immobilized MT in the presence of unlabeled dynactin, 5 nM MAP7 and 1 µM Lis1. The white arrowhead shows the colocalization of kinesin, dynein, and TRAK. **d.** The velocity distribution of individual motor complexes and DDKT assemblies in the presence of 1 µM Lis1 (n = 30, 140, 439, 4, 175, and 165 from top to bottom, three independent experiments per condition). In (**b**) and (**d**), negative velocities correspond to minus-end-directed

motility. The center line and whiskers represent the mean and s.d., respectively. *P*-values are calculated from a two-tailed t-test.

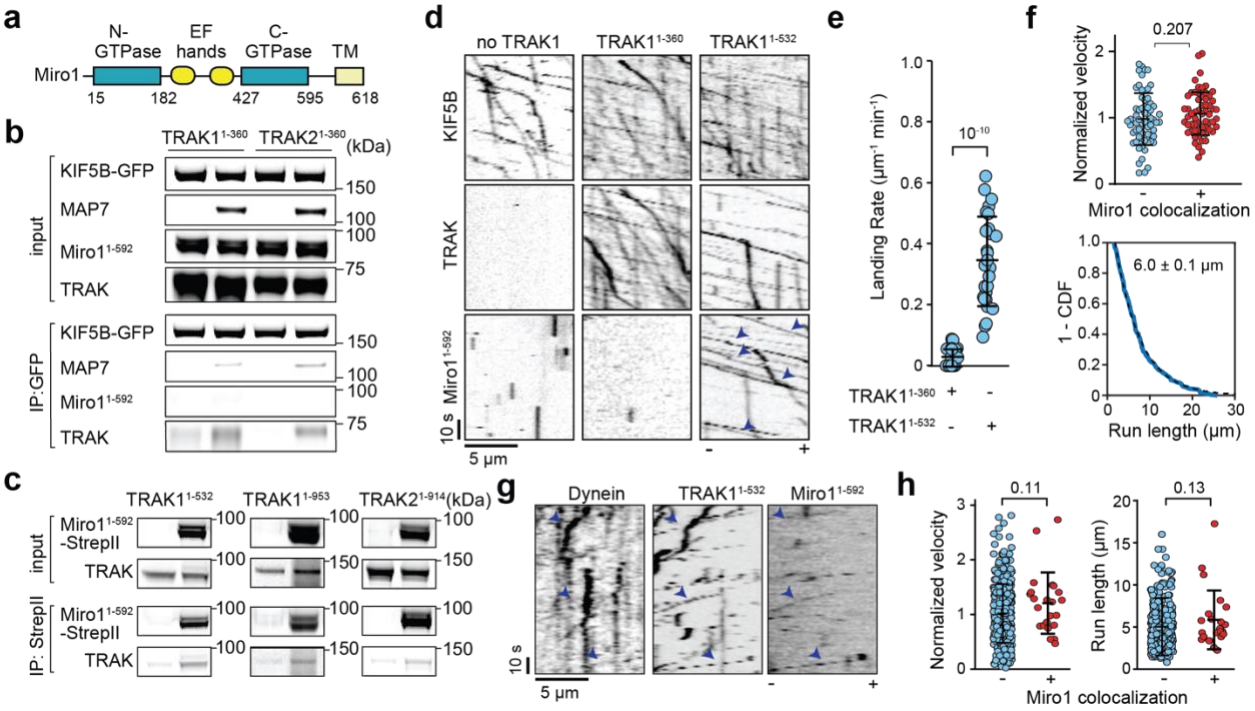

Fig. 2.8. Miro1 is transported by KT and DDT complexes. a. Miro1 binds to GTP at its GTPase domains and Ca^{2+} ions at its EF-hands and localizes to the outer mitochondrial membrane through its transmembrane (TM) domain. **b.** In vitro immunoprecipitation of purified KIF5B-GFP-SNAPf, TRAK1$^{1-360}$ or TRAK2$^{1-360}$, Miro1$^{1-592}$ with or without MAP7. **c.** In vitro immunoprecipitation of purified Miro1$^{1-592}$-StrepII and either TRAK1$^{1-532}$, full-length TRAK1$^{1-953}$, or full-length TRAK2$^{1-914}$ in the presence of GTPγS. KIF5B-GFP-SNAPf was present in all conditions. **d.** Kymographs of Alexa488-KIF5B and LD655-Miro1$^{1-592}$ in the absence of a TRAK adaptor or the presence of LD555-TRAK1$^{1-360}$ or TRAK1$^{1-532}$. Assays were conducted at 10 nM MAP7. Arrowheads show colocalization of Miro1 to TRAK. **e.** The landing rate of KTM co-localizers in the presence of different TRAK constructs (n = 27 MTs for each condition, three independent trials). **f.** (Top) Normalized velocity distribution of KT complexes that localize or not localize with Miro1 (n = 65 and 61 from left to right). (Bottom) 1-CDF of motor run length for KTM complexes (n = 209, three independent experiments). Fits to a single exponential decay (dashed curves) reveal the motor run length (±s.e.). **g.** Representative kymographs of LD488-dynein, LD555-TRAK1$^{1-532}$, and LD655-Miro1$^{1-592}$ in the presence of unlabeled dynactin and 1 µM Lis1. The arrowheads show colocalization of dynein, TRAK1, and Miro1. **h.** The velocity and run length of DDT$_1$$^{1-532}$ that colocalize or not colocalize with Miro1 (n = 349 and 23 from left to right). Assays were conducted in 1 µM Lis1 and the absence of Ca^{2+}. In (**e**), (**f**), and (**h**), the center line and whiskers represent mean and s.d., respectively. *P*-values are calculated from a two-tailed t-test.

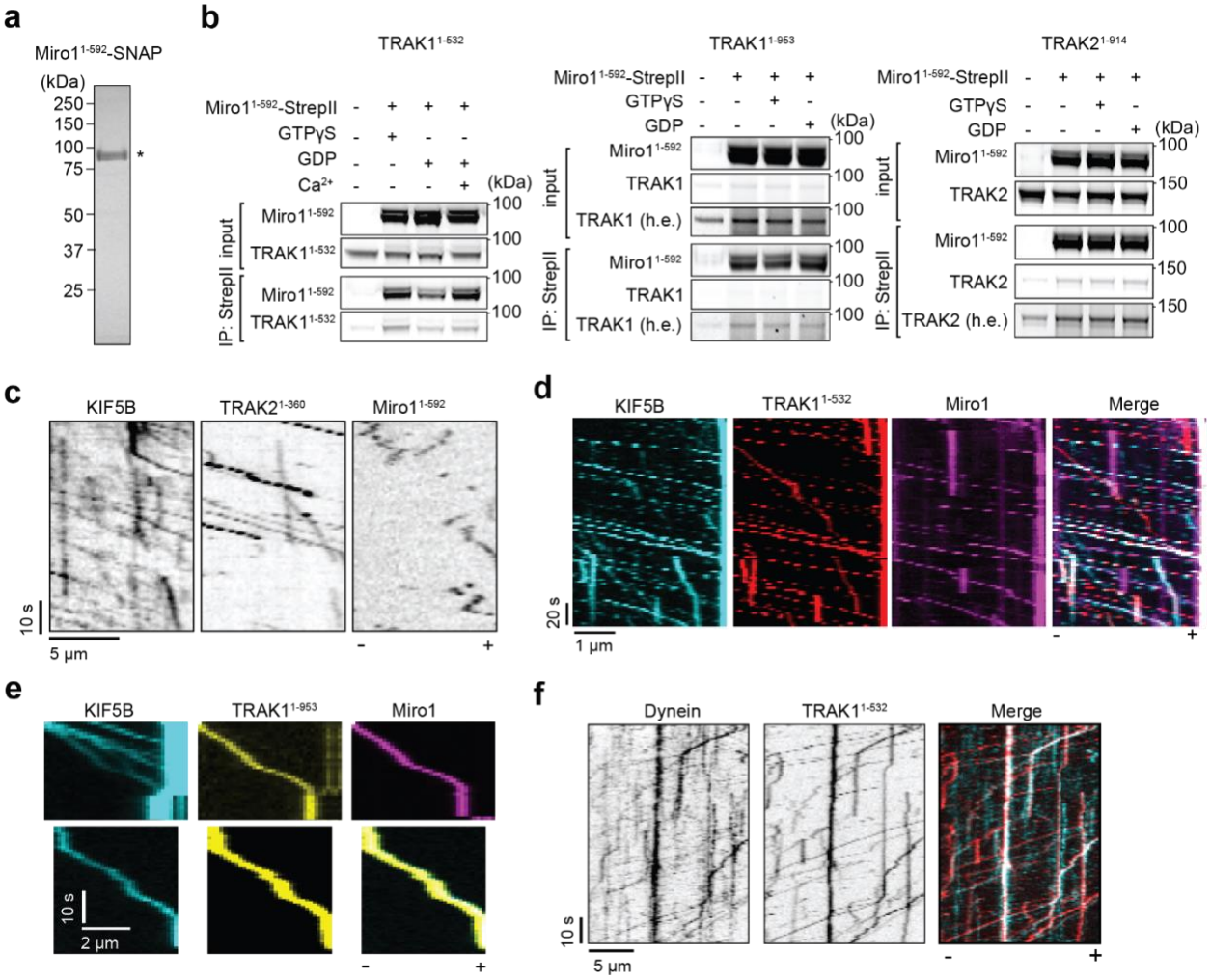

Fig. 2.9. TRAK-Miro1 interactions under different nucleotide and Ca^{2+}conditions. a. Coomassie-stained denaturing gel of purified Miro1$^{1-592}$-SNAP (experiment was repeated twice with reproducible results). **b.** In vitro immunoprecipitation of purified Miro1$^{1-592}$-SNAP-StrepII and either TRAK1$^{1-532}$ (left), full-length TRAK1 (middle), or full-length TRAK2 (right). KIF5B-GFP-SNAPf was present in all conditions. Assays were conducted in the presence of 100 µM GTPγS, 100 µM GDP, or 2 mM Ca^{2+} (h.e.: high exposure) (experiments were repeated twice with reproducible results). **c.** Representative kymograph of Alexa488-KIF5B, LD555-TRAK2$^{1-360}$, and LD655-Miro1$^{1-592}$ in the presence of 10 nM MAP7 (three independent experiments per condition). **d.** Representative kymograph of Alexa488-KIF5B, LD555-TRAK1$^{1-532}$, and LD655-Miro1$^{1-592}$ shows the formation of processive KTM complexes that walk along MTs in the presence of 10 nM MAP7 (three independent experiments per condition). **e.** Two representative kymographs of Alexa488-KIF5B, LD555-labeled full-length TRAK1, and LD655-Miro1$^{1-592}$ show the formation of processive KTM complexes that walk along MTs in the presence of 10 nM MAP7 (three independent experiments per condition). **f.** Representative kymograph of LD655-dynein and LD555-TRAK1$^{1-532}$ shows processive motility of DDT complexes on a surface-immobilized MT in the presence of unlabeled dynactin and 1 µM Lis1 (three independent experiments per condition).

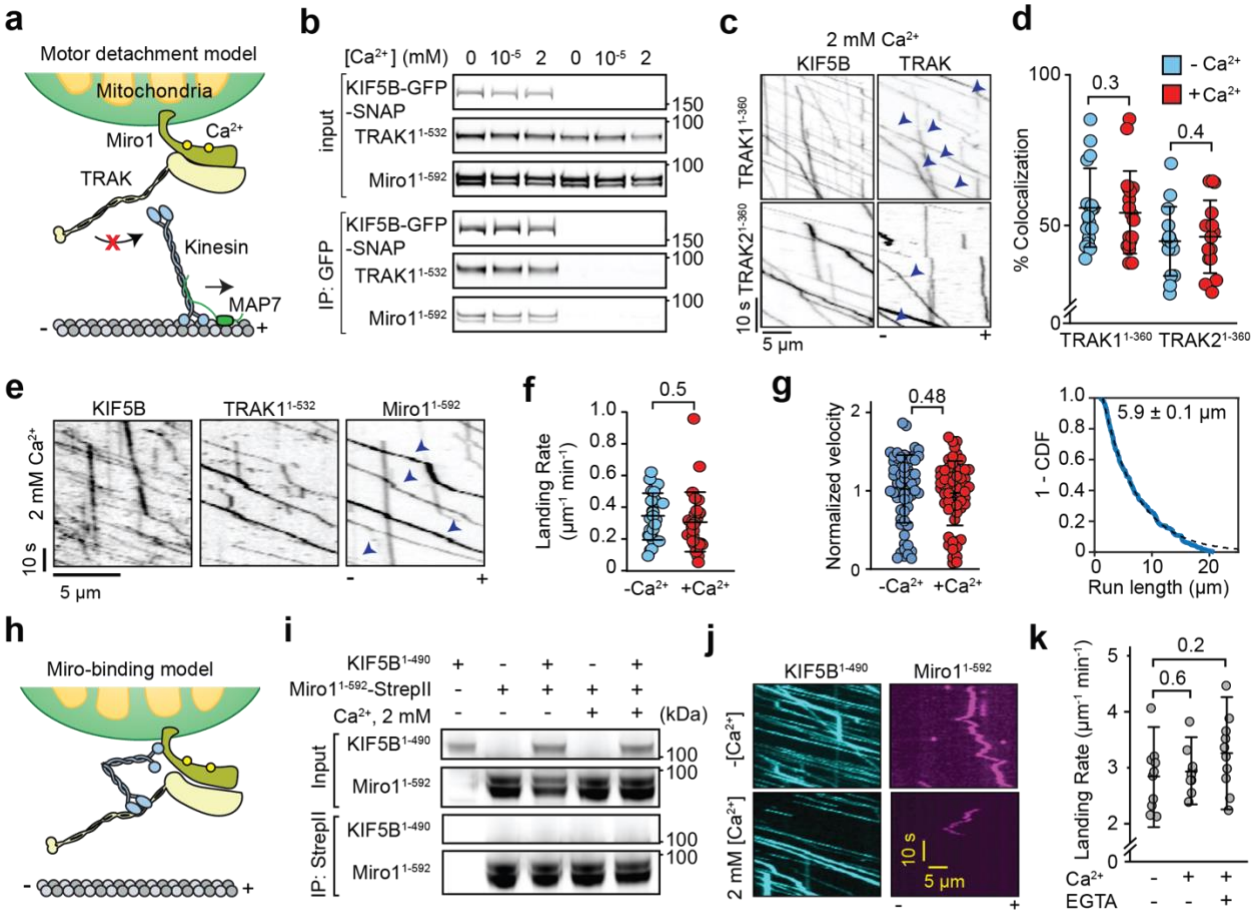

Fig. 2.10. Kinesin-driven transport of Miro1/TRAK1 is not disrupted by Ca^{2+}. a. The motor detachment model predicts that Ca^{2+} binding to Miro1 triggers dissociation of kinesin from TRAK. **b.** In vitro immunoprecipitation of KIF5B-GFP-SNAPf, TRAK1$^{1-532}$, and Miro1$^{1-592}$ in 0, 100 nM, or 2 mM Ca^{2+}. **c.** Representative kymographs show colocalization of LD555-KIF5B and LD655-TRAK adaptors in 2 mM Ca^{2+} and 10 nM MAP7. Arrowheads show colocalization of TRAK to processive kinesins. **d.** The percentage of kinesin runs that colocalize with TRAK on MTs in the presence or absence of 2 mM Ca^{2+} (n = 15, 15, 12, and 12 MTs from left to right, three independent trials). **e.** A representative kymograph of Alexa488-KIF5B, LD555-TRAK1$^{1-532}$, and LD655-Miro1$^{1-592}$ in 2 mM Ca^{2+} and 10 nM MAP7. Arrowheads show colocalization of Miro1 to TRAK. **f.** The landing rate of KTM complexes in the presence or absence of 2 mM Ca^{2+} (n = 27 MTs for each condition, three independent trials). **g.** (Left) Normalized velocity distribution of KTM complexes in the presence or absence of 2 mM Ca^{2+}. (Right) 1-CDF of motor run length for KTM complexes in 2 mM Ca^{2+} (n = 189, three independent experiments). Fits to a single exponential decay (dashed curves) reveal the motor run length (±s.e.). **h.** The Miro-binding model predicts that Ca^{2+} binding to Miro1 triggers the binding of the kinesin motor domain to Miro1. **i.** In vitro immunoprecipitation assays show no interaction between purified KIF5B$^{1-490}$ and Miro1$^{1-592}$-SNAPf-StrepII in the presence and absence of 2 mM Ca^{2+}. **j.** Kymographs show that KIF5B$^{1-490}$ does not colocalize with Miro1 in the presence or absence of 2 mM Ca^{2+}. Assays were performed

in the absence of TRAK adaptors and MAP7. **k.** The landing rate of KIF5B$^{1-490}$ in the presence and absence of 2 mM Ca^{2+} and 2 mM Ca^{2+}-chelating agent EGTA (n = 10 MTs for all conditions, three independent trials). In (**d**), (**f**), (**g**), and (**k**), the center line and whiskers represent mean and s.d., respectively. P-values are calculated from a two-tailed t-test.

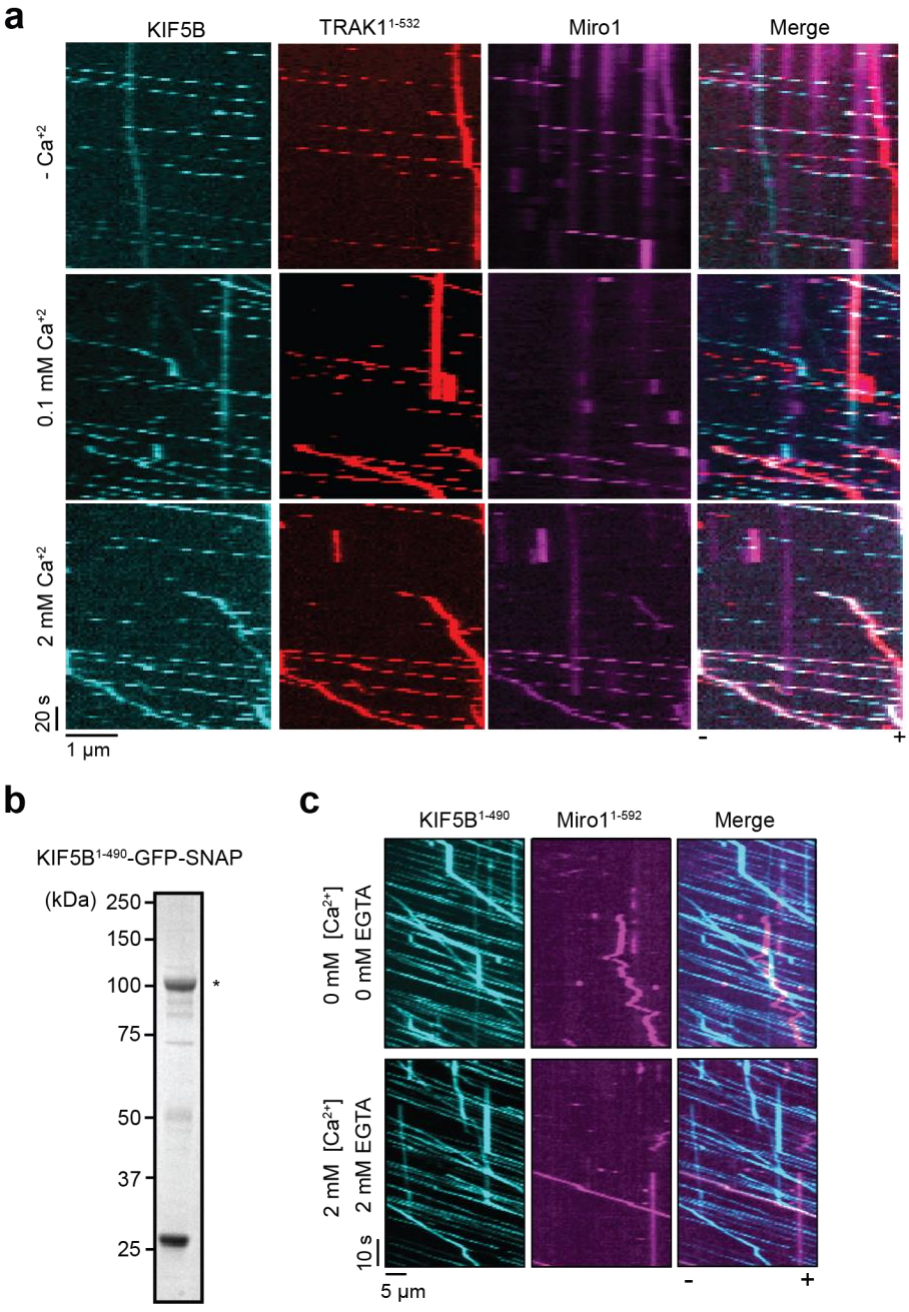

Fig. 2.11. Miro1 does not interact with the kinesin motor domain. a. Representative kymographs show comigration of Alexa488-kinesin, LD555- TRAK1$^{1-532}$, and LD655-Miro1$^{1-592}$ in 0, 0.1, and 2 mM Ca^{2+}. The assay was conducted in the presence of 10 nM MAP7 (three independent experiments per condition). **b.** Coomassie-stained denaturing gel picture of purified KIF5B$^{1-490}$-GFP-SNAP (experiment was repeated twice with reproducible results). **c.** Representative two-color kymographs of KIF5B$^{1-490}$ and Miro1$^{1-592}$ in the presence and absence of

2 mM Ca^{2+} and 2 mM EGTA. Assays were performed in the absence of TRAK and MAP7 (three independent experiments per condition).

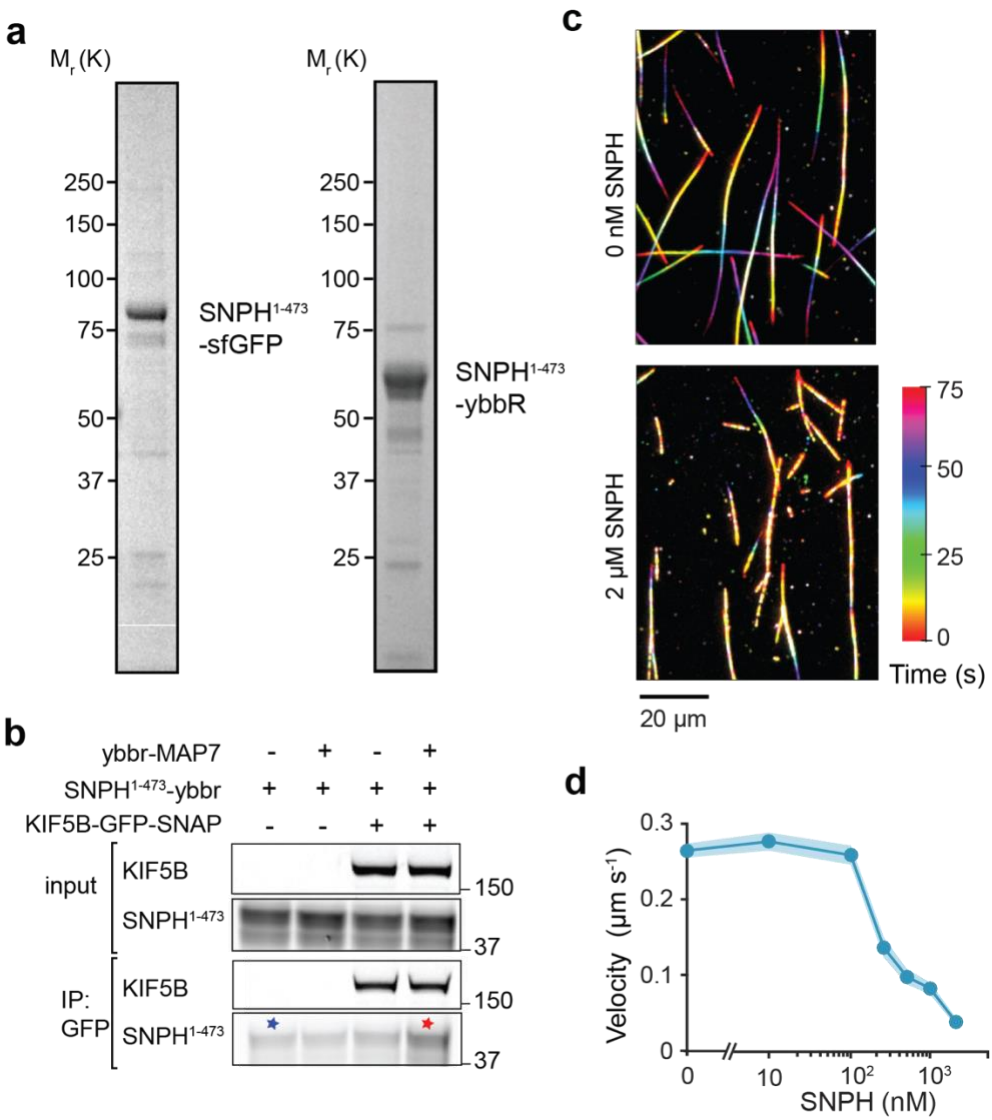

Fig. 2.12. Effect of SNPH on the MT gliding by constitutively-active kinesin. a. Coomassie-stained denaturing gel pictures of purified SNPH$^{1-473}$-sfGFP and SNPH$^{1-473}$-ybbR. **b.** In vitro immunoprecipitation shows no interaction between purified kinesin (KIF5B) and SNPH$^{1-473}$ above background (blue star) and weak interaction in the presence of MAP7 (red star). **c.** Representative color-coded projections of MT gliding driven by 2.5 nM constitutively-active KIF5B$^{1-560}$-GFP motors in the presence or absence of 2 µM SNPH-sfGFP. **d.** MT gliding velocity driven by KIF5B$^{1-560}$ motors in the presence of different SNPH$^{1-473}$-sfGFP concentrations (mean ± s.e.m., *n* = 31, 53, 67, 51, 71, 52, 68 MTs from left to right, three independent trials).

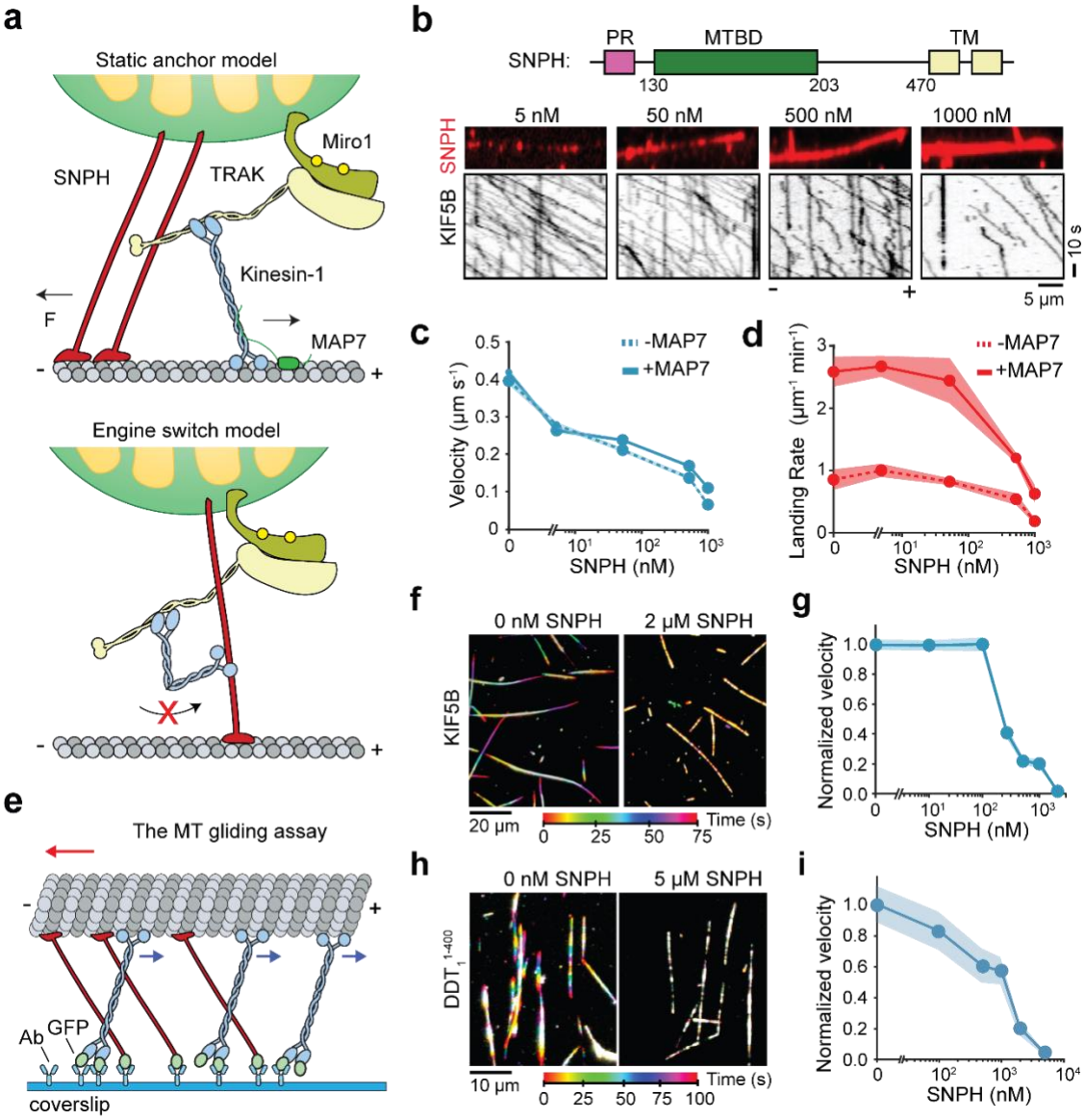

Fig. 2.13. SNPH stalls MT gliding driven by kinesin and dynein motors. a. Static anchor, and engine switch models for SNPH-mediated stalling of mitochondrial transport. **b.** (Top) Domain organization of human SNPH (MTBD: MT-binding domain, PR: proline-rich domain). (Middle) SNPH decorates surface-immobilized MTs. (Bottom) Representative kymographs of kinesin motility in the presence of increasing concentrations of SNPH. The assays were conducted in 10 nM MAP7. **c.** The average velocity of kinesin in the presence (± s.e.m., n = 98, 158, 95, 58, and 20 from left to right) and absence of 10 nM MAP7 (n = 115, 191, 154, 93, and 59 from left to right). **d.** The landing rate of kinesin in the presence and absence of 10 nM MAP7 (mean ± s.e.m., n = 9 MTs for each condition, three independent trials). **e.** Schematic of the MT gliding by kinesin motors. Motors were fixed on the glass surface from their tail through a GFP-antibody linkage. MTs glide with their minus-ends in the lead (red arrows) due to the plus-end directed motility of kinesins (blue arrows). Static binding of SNPH to MTs exerts resistive forces against gliding motility. **f.** Representative color-coded time projections of Cy5-MTs glided by KIF5B-GFP-

SNAPf in the presence or absence of 2 μM SNPH-sfGFP. **g.** Quantification of kinesin-driven MT gliding velocities as a function of increasing SNPH-sfGFP concentration (mean ± s.e.m., n = 50, 57, 58, 59, 71, 70, 61 MTs from left to right, two independent trials). **h.** Representative color-coded time projections of Cy5-MTs with DDT assembled with TRAK1$^{1\text{-}400}$-GFP in the presence or absence of 5 μM SNPH-sfGFP. Assays were conducted in 1 μM Lis1. **i.** Quantification of MT gliding velocities as a function of increasing SNPH-sfGFP concentration (mean ± s.e.m., n = 60, 61, 67, 72, 64, 60 MTs from left to right, three independent trials).

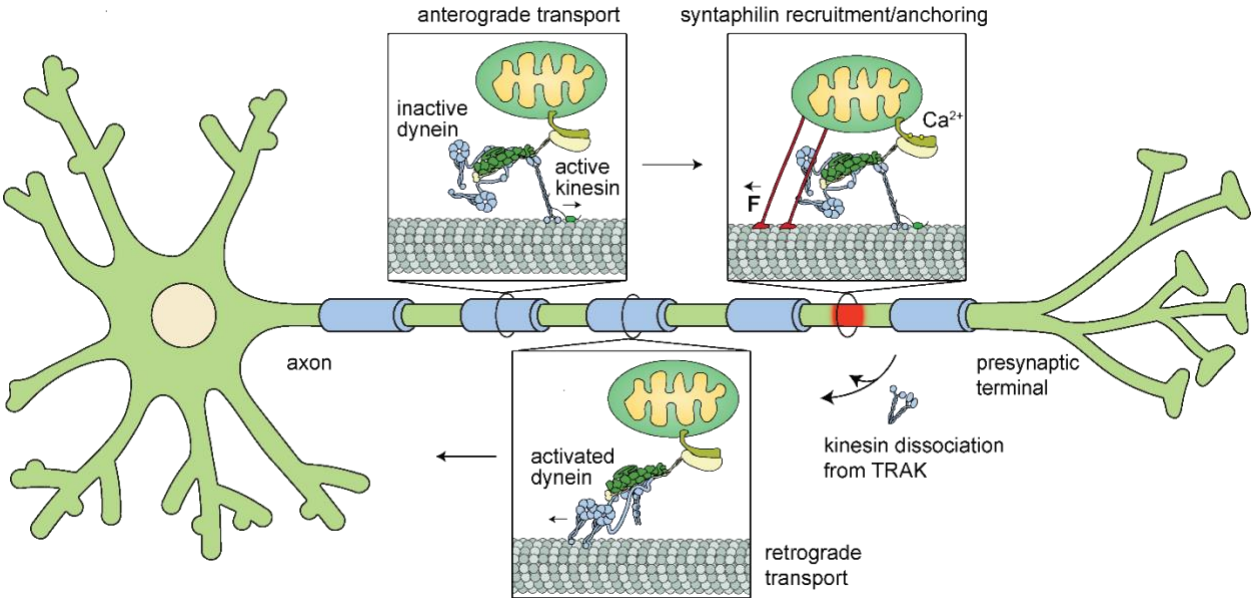

Fig. 2.14. A model for bidirectional transport and Ca^{2+}-mediated arrest of mitochondria in neurons. Mitochondria are transported anterogradely by active kinesin motors recruited by TRAK1 while dynein-dynactin is transported as an inactive passenger. In regions with high Ca^{2+} concentration (red), mitochondria recruit SNPH, which anchors the mitochondria to the MT and stalls the transport machinery. Retrograde transport is initiated by the dissociation of kinesin from TRAK, followed by activation of the DDT complex.

Construct Name	Figures
SNAPf-DYNH1C1$_{R1567E-K1610E}$ -IC2C-LIC2-Robl1-Tctex1-LC8	Fig. 2.1c-f; Fig. 2.2b-c; Fig. 2.6a-g; Fig. 2.7a-d; Fig. 2.8g-h; Fig. 2.9f; Fig. 2.13h-i
TRAK1$^{1-360}$-SNAPf	Fig. 2.1c,f; Fig. 2.2a,b; Fig. 2.3a-f; Fig. 2.4b; Fig. 2.5a Fig. 2.8b,d,e; Fig. 2.10c,d
TRAK1$^{1-400}$-SNAPf	Fig. 2.1c,e,f; Fig. 2.2a-c; Fig. 2.4c; Fig. 2.6a-b, e-g; Fig. 2.7c-d
TRAK2$^{1-360}$-SNAPf	Fig. 2.1d,f; Fig. 2.2a-c; Fig. 2.3a-f; Fig. 2.4b; Fig. 2.8b; Fig. 2.9c
TRAK2$^{1-400}$-SNAPf	Fig. 2.1d-f; Fig. 2.2a-c; Fig 2.4c; Fig. 2.6c-d, Fig 2.7a-d
KIF5B-GFP-SNAPf	Fig. 2.2a-e; Fig. 2.3a-f; Fig. 2.6a-g; Fig. 2.7a-d; Fig. 2.8b-f; Fig. 2.9c-e; Fig. 2.10b-g; Fig. 2.11a; Fig. 2.12b; Fig. 2.13b-d,f,g
MAP7-ybbR	Fig. 2.3a-f; Fig. 2.4b-e; Fig. 2.6a-e; Fig. 2.7a-d; Fig. 2.8b,d-f; Fig. 2.9c-e; Fig. 2.10c-g; Fig. 2.11a; Fig. 2.12b; Fig. 2.13b-d
TRAK1$^{1-400}$-GFP	Fig. 2.13h-i
TRAK1$^{1-532}$-SNAPf	Fig. 2.5b; Fig. 2.8c-h; Fig. 2.9b,d,h; Fig. 2.10e-g; Fig. 2.11a
KIF5B$^{\Delta 1-336}$-GFP-SNAPf	Fig. 2.4a; Fig. 2.6f,g
KIF5B$^{1-490}$-GFP-SNAPf	Fig. 2.10i-k; Fig. 2.11b,c
Miro1$^{1-592}$-SNAPf- StrepII	Fig. 2.8a-h; Fig. 2.9a-e;Fig. 2.10b,e-g,i-k; Fig. 2.11a,c
TRAK1$^{1-953}$-SNAPf	Fig. 2.8c; Fig. 2.4d,e; Fig. 2.5b; Fig. 2.9e
TRAK1$^{1-953}$-sfGFP-SNAPf	Fig. 2.9b
TRAK2$^{1-914}$-SNAPf	Fig. 2.8c; Fig. 2.4d,e; Fig. 2.9b
SNPH$^{1-473}$-sfGFP	Fig. 2.13b-d,f-i; Fig. 2.12a,c,d
SNPH$^{1-473}$-ybbR	Fig. 2.12a,b
Lis1-SNAPf	Fig. 2.1c,d,f; Fig. 2.8g,h; Fig. 2.13h-i; Fig. 2.2b; Fig. 2.7c,d; Fig. 2.9f

Table 2.1. The list of constructs used in this study. The SNAPf- DYNH1C1$_{R1567E-K1610E}$ -IC2C-LIC2-Robl1-Tctex1-LC8 construct was a gift from A. Carter (MRC, UK). Other constructs were cloned into the pOmniBac vector for baculovirus expression in SF9 cells, except SNPH constructs which were cloned into the pET17b vector for bacterial expression. A ZZ-Tev tag was inserted at the N-termini of all constructs (except Miro1) for binding the protein to IgG beads and eluting by TEV protease. The SNAPf tag was used to label the proteins with fluorescent dyes or biotin. The ybbR tag was inserted for SFP-catalyzed labeling of proteins with CoA-functionalized fluorescent dyes or biotin. A StrepII tag was inserted at the C-termini of Miro1$^{1-592}$ to elute the protein with desthiobiotin from Strep-Tactin-coated beads.

2.6 Methods

2.6.1 Cloning and plasmid generation

The constructs expressing the phi-dynein mutant (SNAP–DHC R1567E-K1610E), full-length TRAK1, and full-length TRAK2 were provided in a pACEBac1 vector backbone by A.P. Carter (MRC, University of Cambridge). The sequences encoding full-length or truncated versions of human TRAK1 and TRAK2 were cloned into the pOmniBac vector. All constructs contained an N-terminal His6-ZZ tag followed by a TEV protease cleavage site for protein purification and a C-terminal SNAP-tag or GFP fusion for labeling and imaging purposes. A cDNA for full-length human kinesin (*KIF5B*; amino acids 1–963, clone ID 8991995) was obtained from GE Dharmacon and fused to GFP-SNAPf at its C terminus. The phi mutant of the dynein-1 heavy chain (DHC) was co-expressed by fusing the coding sequence to the pDyn2 plasmid containing genes encoding IC2C, LIC2, TCTEX1, LC8, and ROBL1, as described[73]. The list of constructs used for each dataset is given in **Table 2.1**.

2.6.2 Protein expression and purification

Native dynactin was purified from pig brains[99]. Fresh brains were purchased from a butcher and transported in ice-cold PBS. Brains were washed in homogenization buffer (35 mM PIPES pH 7.2, 5 mM $MgSO_4$, 1 mM EGTA, 0.5 mM EDTA) and frozen in liquid nitrogen. Three frozen brains were broken into pieces and blended in a blender in the presence of homogenization buffer supplemented with four EDTA protease-inhibitor tablets per 500 mL (Roche), 1.6 mM PMSF, 1 mM DTT, and 0.1 mM ATP. The brain lysate was gently stirred for 30 min at 4°C until completely thawed and was then spun in a JLA 8.1 fixed angle rotor (Beckman Coulter) at 8,000 r.p.m. for 45 min at 20 °C. The supernatant was collected and further clarified using a Type 45 T.i. rotor (Beckman Coulter) at 45,000 r.p.m. for 50 min at 4°C. The supernatant was then filtered with a glass-fiber filter (Sartorius), followed by a 0.45 μm filter (Milex Millipore). The sample was loaded into a SP-Sepharose column pre-equilibrated with SP buffer (35 mM PIPES pH 7.2, 5 mM $MgSO_4$, 1 mM EGTA, 0.5 mM EDTA, 1 mM DTT, and 0.1 mM ATP) using an Akta FPLC (GE). The column was washed with 4 column volumes of SP buffer in the presence of 3 mM KCl followed by elution using a linear gradient up to 250 mM KCl. Fractions collected from the first major peak were pooled, filtered using a 0.22 μm filter (Milex Millipore), then loaded onto a MonoQ 16/10 column (Cytiva) pre-equilibrated with MonoQ buffer (35 mM PIPES pH 7.2, 5 mM $MgSO_4$, 1 mM EGTA, 0.5 mM EDTA, 1 mM DTT, and 0.1 mM ATP). The column was washed with 10 column volumes of MonoQ buffer followed by elution using a linear gradient up to 150 mM KC1 in 1 column volume, a second linear gradient up to 350 mM KCl in 10 column volumes, and a third linear gradient up to 1 M KCl in 1 column volume. The peak dynactin fractions located at approximately 38 mS cm^{-1} were then pooled and concentrated to a volume of about 3 mL and loaded onto a G4000$_{SW}$ 21.5/600 column (Tosoh Bioscience) equilibrated with GF150 buffer (25 mM HEPES pH 7.2, 150 mM KCl, 1 mM $MgCl_2$, 5 mM DTT, and 0.1 mM ATP) for gel-filtration. The dynactin peak collected, pooled, and concentrated to approximately 2 mg mL^{-1} using an 0.5 mL 100 kDa MWCO filter unit (Millipore). 2 μL aliquots were then flash frozen in liquid nitrogen and stored at -80 °C.

The phi mutant of dynein, KIF5B, MAP7, and truncated TRAK1, and TRAK2 constructs were purified from baculovirus-infected SF9 cells (UC Berkeley Cell Culture Facility). Briefly, cell pellets were resuspended in a lysis buffer (see below) supplemented with Roche cOmplete Protease

Inhibitor Cocktail and lysed using a dounce homogenizer (20 strokes with loose plunger followed by 20 strokes tight plunger). The cell lysate was clarified by centrifugation at 186,000 g for 45 min, incubated with IgG Sepharose (GE Healthcare) for 2 hr at 4°C, applied to a gravity flow column, and washed extensively with a TEV wash buffer (see below). The protein-bead complexes were then treated with TEV protease at 12 °C overnight. The mixture was then centrifuged at 4,000 g for 5 min and the supernatant was concentrated using an Amicon Ultra 0.5 mL spin column (EMD Millipore). Protein concentration was determined by measuring the OD_{280} using Nanodrop 1000.

Different buffer conditions were used for each protein preparation. Cells expressing dynein were lysed in a dynein lysis buffer (50 mM HEPES pH 7.4, 100 mM NaCl, 10% Glycerol, 1 mM DTT, 2 mM PMSF), IgG beads were washed with a dynein TEV wash buffer (50 mM Tris-HCl pH 7.4, 150 mM K-Acetate, 2 mM Mg-Acetate, 1 mM EGTA, 10% Glycerol, 1 mM DTT) and the protein was concentrated using a 100K molecular weight cut-off (MWCO) spin filter. For kinesin purification, the cells were lysed in a kinesin lysis buffer (50 mM HEPES pH 7.4, 1 M NaCl, 10% Glycerol, 1 mM DTT, 2 mM PMSF), IgG beads were washed with a kinesin TEV wash buffer (50 mM HEPES pH 7.4, 300 mM NaCl, 10% Glycerol, 1 mM EGTA, 1 mM DTT), and the protein was concentrated using 100K MWCO spin filter. MAP7 purification was performed using a MAP7 lysis buffer (25 mM HEPES pH 7.4, 1 M KCl, 10% Glycerol, 1 mM DTT, 1 mM PMSF) and MAP7 TEV wash buffer (25 mM HEPES pH 7.4, 300 mM KCl, 1 mM EGTA, 10 mM $MgCl_2$, 10% Glycerol, 1 mM DTT). MAP7 was concentrated using a 50K MWCO spin filter. Truncated TRAK constructs were purified in the presence of high salt, glutamic acid, and arginine to improve solubility (TRAK lysis buffer: 50 mM HEPES pH 7.4, 1 M NaCl, 10% Glycerol, 50 mM L-Glu, 50 mM L-Arg, 1 mM DTT, 2 mM PMSF, 1 mM ATP; and TRAK TEV wash buffer: 50 mM HEPES pH 7.4, 500 mM NaCl, 50 mM L-Glu, 50 mM L-Arg, 10% Glycerol, 1 mM EGTA, 1 mM DTT, 1 mM ATP), and protein was concentrated using a 50K MWCO spin column. Full-length TRAK1 and TRAK2 were purified from HEK 293F $GNTI^{-/-}$ cells (UC Berkeley Cell Culture Facility) using polyethyleneimine (PEI) transfection of the pcDNA and the TRAK purification procedure described above.

$Miro1^{1-592}$ ($Miro1^{1-592}$-SNAP-psc-StrepII) was purified using Miro lysis buffer (25 mM HEPES pH 7.4, 300 mM NaCl, 10% Glycerol, 1 mM DTT, 1 mM PMSF) supplemented with 1x protease inhibitor cocktail and lysed using a dounce homogenizer. The lysate was clarified by centrifugation at 65,000 g for 45 min, incubated with Streptactin Sepharose beads (IBA) for 2 hr at 4°C, applied to a gravity flow column, and washed extensively with Miro wash buffer (25 mM HEPES pH 7.4, 300 mM NaCl, 10% Glycerol, 1 mM DTT). The protein was then eluted from beads with 3 mM desthiobiotin and concentrated using a 50K MWCO spin column.

$SNPH^{1-473}$ was purified from BL21(DE3) *E. coli* cells (UC Berkeley QB3 MacroLab). Briefly, cell pellets were resuspended in SNPH lysis buffer (25 mM HEPES pH 7.4, 300 mM NaCl, 10% Glycerol, 1 mM DTT, 1 mM PMSF) supplemented with 1x protease inhibitor cocktail and lysed using a tip sonicator for 2 min. The lysate was clarified by centrifugation at 65,000 g for 45 min, incubated with IgG Sepharose beads for 2 hr at 4°C, applied to a gravity flow column, and washed extensively with SNPH wash buffer (25 mM HEPES pH 7.4, 300 mM NaCl, 10% Glycerol, 1 mM DTT). The protein-bead complexes were then treated with TEV protease at 4°C overnight. The mixture was then centrifuged at 4,000 g for 5 min and the supernatant was concentrated using a 50K MWCO spin column.

2.6.3 Co-immunoprecipitation assays

For each sample, 10 µg of each protein construct was pre-mixed on ice for 5 min and then added to 15 µL of GFP-Trap beads (Chromotek) that were pre-washed with the MB buffer (30 mM HEPES, 5 mM $MgSO_4$, 1 mM EGTA, pH 7.0). Samples were then diluted 1:2 in MB supplemented with 100 mM NaCl, 1 mg ml^{-1} BSA, and 1 mM DDT and incubated on ice for 2 hr to facilitate complex formation. 10% of samples were collected for input lanes and then washed 3x with the MB buffer including supplements. Samples were then resuspended into LDS sample buffer, boiled for 10 min at 95 ºC, and run on an SDS-PAGE gel. Imaging was performed on a GE Typhoon FLA fluorescence imager.

2.6.4 Labeling

Proteins were labeled with fluorescent probes before they were eluted from the affinity columns. For SNAP labeling, bead slurry was concentrated to 5 mL, followed by the addition of 5 nmol of either BG-LD555 or BG-LD655 dye, followed by incubation for 1 hr at 4 ºC. The slurry was added to a gravity flow column and washed extensively in a wash buffer. For ybbR labeling, bead slurry was concentrated to 5 mL, followed by the addition of 5 nmol of either CoA-LD555 or BG-LD655 dye followed by incubation for 30 min at room temperature in the presence of 1 µM Sfp phosphopantetheinyl transferase to catalyze protein labeling.

2.6.5 Motility assays

To immobilize biotinylated MTs to the coverslip, 1 mg ml^{-1} BSA-biotin (Sigma) was introduced into the flow chamber, which was then washed with MB buffer supplemented with 1 mM DTT, 10 µM taxol, 1.25 mg ml^{-1} casein (Sigma) and 0.5% pluronic (MBCT). MBCT was additionally supplemented with 0.2% methylcellulose and 50 nM K-Acetate for DDKT motility assays and dynein motility assays with $TRAK1^{1-532}$. The chamber was then incubated with 20 µl 1 mg ml^{-1} streptavidin (NEB) in MBCT and washed with 40 µl MBCT. For imaging dynein motility, fluorescently-labeled dynein, dynactin, and a cargo adaptor (TRAK1 or TRAK2) were mixed at a 1:5:20 molar ratio in MB for $TRAK1^{1-400}$ and $TRAK2^{1-400}$ and a 1:3:10 molar ratio for $TRAK1^{1-532}$, respectively. $Miro1^{1-592}$, dynein, dynactin, and $TRAK1^{1-532}$ were mixed at a 1:3:10:30 molar ratio, respectively, in the presence of 1 µM Lis1. For imaging kinesin motility, kinesin, a cargo adaptor (TRAK1 or TRAK2), MAP7, and $Miro1^{1-592}$ were mixed at a 1:3:3:3 molar ratio, respectively, in MB buffer. For imaging both dynein and kinesin simultaneously, dynein, dynactin, kinesin, and a cargo adaptor were mixed at a 1:3:1:1 (TRAK1) or 1:5:1:1 (TRAK2) ratios, respectively, in MB buffer with the stated concentration of MAP7. The mixtures were incubated on ice for 10 min and diluted 30-fold in MBCT. Finally, the mixture was diluted 10-fold in the stepping buffer (MBCT supplemented with 0.1 mg ml^{-1} glucose oxidase, 0.02 mg ml^{-1} catalase, 0.8% D-glucose, and 1 mM Mg·ATP) and introduced into the chamber. Motility was recorded for 5 min. For assays including $Miro1^{1-592}$, 0.1 mg ml^{-1} biotin-BSA was also included in the stepping buffer for surface passivation.

2.6.6 Gliding assays

Rabbit monoclonal anti-GFP antibody (~0.4 mg ml^{-1}, Covance) was flown into an assay chamber and incubated for 3 min. The chamber was washed with 30 µl MB supplemented with 1 mM DTT, 10 µM taxol, and 1.25 mg ml^{-1} casein. For kinesin-driven MT gliding, 10 µl of 2.5 nM GFP-tagged kinesin was subsequently added to the chamber. In the case of DDT-driven MT gliding, 10 nM

dynein, 10 nm dynactin, and 10 nM GFP-TRAK2$^{1-400}$ were incubated in MB on ice for 10 min in the presence of 1 μM Lis1, and 10 μl of this mixture were added to the chamber. After 2 min incubation, the unbound motor was removed by washing the chamber with 30 μl MB. For experiments with SNPH, 10 μl of SNPH$^{1-473}$-sfGFP was added to the chamber at the indicated concentration for 2 min followed by a 30 μl MB wash. Then, 10 μl of 200 nM Cy5-labeled MTs were flown to the chamber and allowed to bind the kinesin- or DDT-decorated surface for 4 min. The chamber was then washed with 60 μl MB. Lastly, 10 μl of imaging buffer (MB supplemented with 0.02 mg ml^{-1} catalase, 0.8% D-glucose, and 1 mM Mg·ATP) was flown into the chamber to initiate gliding motility.

2.6.7 Microscopy

Fluorescence imaging experiments were performed using a custom-built multicolor TIRF microscope equipped with a Nikon Ti-E microscope body, a 100X magnification 1.49 N.A. apochromat oil-immersion objective (Nikon), a perfect focusing system, and an electron-multiplied charge-coupled device camera (Andor, Ixon EM+, 512 × 512 pixels) with an effective pixel size of 160 nm after magnification. Alexa488/GFP, LD555, and LD655 probes were excited with fiber-coupled 0.05 kW cm^{-2} 488-nm, 561-nm, and 633-nm laser beams (Coherent) through a Nikon TIRF Illuminator, and their fluorescent emissions were filtered through a notch dichroic filter and 525/40, 585/40, and 655/40 bandpass emission filters (Semrock), respectively. Multicolor fluorescence imaging was performed using the time-sharing mode in MicroManager. Videos were recorded at 2-4 Hz.

2.6.8 Data analysis

Coiled-coil prediction scores of human TRAK1 and TRAK2 were calculated from the NPS@ server using the algorithm of Lupas et al.[54]. Videos were analyzed in ImageJ. Kymographs were generated by plotting segmented lines along the MTs using a custom-written ImageJ macro. The processive movement was defined and analyzed as described previously[27]. Complexes that exhibited diffusive movement, ran for less than 250 nm, and paused for more than 1 s were excluded from velocity analysis. For two-color imaging, the fluorescence channels were overlaid in ImageJ to generate a composite image. Colocalization events were manually scored in kymographs. For two-color imaging of a motor and a cargo adaptor (TRAK1 or TRAK2), processive motility events observed in the cargo adaptor channel that did not colocalize with a motor were still included in the velocity analysis. **Statistics and reproducibility:** At least two independent repetitions were performed to obtain any given result. The number of replicates (*n*) and statistical analysis methods are clearly stated in the figure legends. Representative data are shown from independently repeated experiments.

Chapter 3. Regulation of Dynein by Mitotic Adapter Protein NuMA

This chapter presented in this book, was published in the following paper:

Aslan, M.[*], d'Amico, E.A.[*], Cho, N.H.[*], Taheri, A., Perez-Bertoldi, J.M., Zhao, Z., Zhong, X., Blaauw, M., Carter A.P., Dumont, S., and Yildiz, A. Activation and regulation of the dynein-dynactin-NuMA complex. Nat. Chem. Bio., 2026.
* Equal contribution.

3.1 Abstract

During cell division, NuMA orchestrates the focusing of microtubule minus-ends in spindle poles and cortical force generation on astral microtubules by interacting with dynein motors, microtubules, and other cellular factors. Here, we used in vitro reconstitution, cryo-electron microscopy, and live cell imaging to understand the mechanism and regulation of NuMA. We determined the structure of the processive dynein/dynactin/NuMA complex (DDN) and showed that the NuMA N-terminus drives dynein motility in vitro and facilitates dynein-mediated transport in live cells. The C-terminus of NuMA directly binds to and suppresses the dynamics of the microtubule minus-end. Full-length NuMA is autoinhibited for its interactions with dynein and microtubules, but mitotically phosphorylated NuMA activates dynein in vitro and interphase cells. Together with dynein, activated full-length NuMA focuses microtubule minus-ends into aster-like structures. These results provide critical insights into the activation of NuMA and dynein for their mitotic functions.

3.2 Introduction

Nuclear Mitotic Apparatus protein (NuMA) interacts with DNA, microtubules (MTs), motors, plasma membranes, importins, and other accessory proteins for fundamental cellular processes[38]. In interphase, NuMA localizes to the nucleus, where it organizes chromosomes and helps the formation of a single, round nucleus[19,20]. After nuclear envelope breakdown, NuMA accumulates at MT minus-ends and recruits a minus-end-directed MT motor, dynein. Together with dynein, NuMA helps focus the minus-ends of the MTs into spindle poles and maintain a steady-state spindle structure[21-26] **(Fig. 3.1a)**. Minus-end-directed forces generated by dynein counteract forces generated by plus-end-directed kinesin-5s[27,28] to maintain spindle structure[29,30]. NuMA also recruits dynein to the cell cortex[31-35], where dynein anchors astral MTs and generates tension to determine the position and orientation of the spindle[35-37]. Consistent with its cellular roles, NuMA dysfunction causes defects in spindle mechanics and architecture, as well as micronuclei formation[38].

NuMA is a large (237 kDa) and extended protein containing an N-terminal HOOK domain (amino acids (a.a.) 1-153) and a C-terminal region (a.a. 1700-2115) separated by a ~210 nm long coiled-coil domain[39,40]. The central coiled-coil facilitates dimerization[40], provides the extension needed for properly crosslinking MTs and DNA[20,41,42], as well as efficiently capturing astral MTs at the cell cortex[43]. The coiled-coil also prevents the binding of NuMA to chromosomes during mitosis[20]. The C-terminal region is disordered and contains two MT-binding sites (MTBD1 (a.a. 1914-1985) and MTBD2 (a.a. 2002-2115)), sites that bind to DNA and other associated factors, a clustering motif, and a nuclear localization signal[38]. MTBD2 can bind to the MT lattice[44] and is required for spindle-pulling activity at the cortex in human cells[35,36]. MTBD1 has a weaker affinity for MTs[45],

but it is required for spindle pole focusing[46,47] and accumulation of NuMA to the minus-end of MTs in mammalian cells[26]. There are contradictory reports for the distinct roles of MTBD1 and MTBD2 in spindle pole focusing and orientation in other cell types[48], and it remains unclear how these MTBDs bind MTs and regulate MT dynamics.

Dynein forms a 1.4 MDa complex consisting of two copies of six subunits (heavy, intermediate, and light intermediate chains, and three light chains, Fig.1a)[100]. The dynein heavy chain is the largest subunit, which contains AAA+ ATPase and MT binding domains. The tail of the heavy chain facilitates homodimerization and recruitment of other subunits. Isolated dynein is autoinhibited and does not actively move along the MT[101,102]. Activation of dynein motility requires recruitment to its cofactor dynactin (a 23-subunit, 1.2 MDa complex) via the coiled-coil region of adaptor proteins[72,73,103]. These activating adaptors contain several conserved motifs such as a specific binding site (i.e., CC1-box, HOOK, and EF-hand domains) for the C terminus of the dynein light intermediate chain (DLIC), a heavy chain binding site 1 (HBS1) motif for interaction with the dynein heavy chain (DHC) and a Spindly motif for interacting with the pointed end subcomplex of dynactin[13]. Studies in live cells showed that the N-terminal portion of NuMA (a.a. 1-505) is required for the recruitment of dynein to the cell cortex[36]. This region of NuMA contains a coiled coil and two regions reported to interact with the DLIC (an N-terminal HOOK domain and a CC1-box-like motif (a.a. 360–385))[104], along with a predicted Spindly motif (a.a. 417–422)[35] (Fig. 1b). Collectively, these observations suggest that the N-terminus of NuMA can form a complex with dynein and its cofactor dynactin. However, the presence of two distinct DLIC-binding sites, which has not been observed in any other activating adaptor, as well as the absence of a clear DHC binding site (HBS1), limits our understanding of how NuMA interacts with dynein and dynactin. It also remains unclear whether NuMA requires additional factors or post-translational modifications to activate dynein.

Our understanding of how NuMA orchestrates spindle assembly, maintenance, and orientation mostly comes from studies in cells. The molecular mechanisms by which NuMA is regulated and repurposed for its mitotic functions, recruits dynein/dynactin, localizes to the minus-ends of MTs, and focuses MT minus-ends remain unclear. The lack of in-depth *in vitro* biochemical and biophysical characterization of NuMA was partly due to its large size, low solubility, and tendency to form large clusters[35,40,105]. In this study, we used biochemical reconstitution, cryo-electron microscopy (cryo-EM), *in vitro* motility assays, and live cell imaging to investigate how human NuMA binds MTs and focuses MTs together with dynein. We demonstrated that the NuMA N-terminus forms a ternary complex with dynein and dynactin and activates dynein motility, whereas the C-terminal region preferentially binds and suppresses the dynamicity of the minus-end of MTs. Full-length (FL) NuMA only weakly binds MTs or activates dynein, whereas mitotically phosphorylated NuMA activates dynein motility *in vitro* and triggers dynein-driven transport in interphase cells. Together with dynein, active NuMA FL focuses minus-ends of MTs into aster-like structures *in vitro*. These results provide key insights into how NuMA organizes MTs and drives mitotic functions of dynein in the spindle body and at the cell cortex.

3.3 Results

3.3.1 The NuMA N-terminus assembles into an active DDN complex

To test the ability of NuMA to activate dynein motility *in vitro*, we recombinantly expressed and purified three human NuMA constructs containing the N-terminal coiled-coil (a.a. 1-505, 1-705, and 1-1699) from insect cells **(Fig. 3.1b, Fig. 3.2)**. Mass photometry showed that all three constructs form homodimers **(Fig. 3.1c)**[106,107]. We next performed multi-color single-molecule motility assays on surface-immobilized taxol-stabilized MTs in the presence of dynein, dynactin, and Lis1, which favors the assembly of dynein with dynactin and adaptor protein **(Fig. 3.1d)**[75,76]. In the absence of NuMA, dynein did not exhibit any processive runs on MTs. The addition of NuMA N-terminal constructs resulted in the activation of dynein motility and comigration of NuMA with dynein towards the minus-ends of MTs **(Fig. 3.1e)**. The velocity, run length, and run frequency of dynein/dynactin/NuMA (DDN) complexes with shorter N-terminal coiled coils were comparable to dynein-dynactin complexes with other activating adaptors, such as BICDR1[94] **(Fig. 3.1f)**. However, DDN with NuMA 1-1699 had ~5-fold lower run frequency and ~30% lower velocity than that of the shorter NuMA fragments, suggesting that the long coiled-coil has an inhibitory effect on DDN motility. These results showed that NuMA is a bona fide cargo adaptor that activates dynein-dynactin motility.

3.3.2 Cryo-EM imaging of the DDN complex on MTs

To understand how NuMA forms a ternary complex with dynein and dynactin, we collaborated with Andrew P. Carter's laboratory at MRC Laboratory of Molecular Biology, Cambridge, United Kingdom. Ennio A. d'Amico prepared DDN complexes with NuMA 1-705 in the presence of Lis1 and used a previously established cryo-EM workflow[108,109]. He obtained a ~6.5 Å resolution map of the part of the complex that contains dynactin, dynein tails, and the coiled-coil of NuMA **(Fig. 3.3a-b and Fig. 3.5)**. The dynein motor domains, p150 arm, and Lis1 were not resolved. NuMA coiled-coil segments run along the length of dynactin, extending to the pointed end, and recruit two dynein motors (dynein-A and -B, **Fig. 3.3b**). The AlphaFold2 (AF2) model of NuMA predicts a break in the first coiled-coil between CC1a (a.a. 212-269) and CC1b (a.a. 276-396, **Fig. 3.3a**) that agrees with the density in our map **(Fig. 3.3b, Fig. 3.4a)**. Our map also shows extra density visible outside the pointed end. Based on a high-confidence AF2 model of the interaction between NuMA and the dynactin pointed end **(Fig. 3.4b-c)**, we assigned this density to the Spindly motif site at the N-terminus of CC2 (408-705; **Fig. 3.3b**).

In our model, CC1a contacts dynein-A at a site that includes DHC residues Y827 and R759. In other dynein/dynactin complexes[108,109], these residues bind the adaptor HBS1 motif, which consists of a conserved Gln residue and acidic patch **(Fig. 3.3c, Fig. 3.4d)**. AF2 is unable to predict a NuMA HBS1-DHC interaction. However, from the position of the CC1a fragment, NuMA is likely to bind dynein-A using an acidic patch (residues 231-240) and a conserved region near Q215 **(Fig. 3.3c)**. Although the HBS1 site is typically located in the middle of the coiled-coil in other activating adaptors[109], this putative HBS1 site of NuMA is at the very N-terminus of the coiled-coil marked by a conserved proline residue (P212).

NuMA is reported to bind the C-terminus of DLIC both through its Hook domain and a CC1-box-like motif[104]. In our structure, the proposed CC1-box-like motif sits on the far end of CC1b, in contact with the dynactin pointed end. Distance constraints and the lack of any additional density corresponding to the DLIC indicate that the CC1-box-like motif is unlikely to be engaged in interactions with dynein in our structure **(Fig. 3.3e)**. While we cannot resolve the NuMA Hook domain due to its flexibility, an AF2 prediction suggests the DLIC1 helix, with its two conserved phenylalanines fits between the α8 helix and the α7-α8 loop of the NuMA Hook domain[104] **(Fig. 3.3f-g)**. This position is consistent with previous mutational analysis[104]. Compared to the structure of the HOOK3 Hook domain – DLIC1 helix complex[110], the NuMA Hook domain lacks an α7 helix, which translates to closer contact with the α8 helix **(Fig. 3.3f)**.

NuMA makes multiple contacts with the pointed end subunits of dynactin through CC1b and the Spindly motif on CC2 **(Fig. 3.3e)**, but its Spindly motif differs from the consensus LxxEΦ motif (where Φ is hydrophobic) found in other adaptors[109]. In BICDR1 and JIP3, the hydrophobic residues in this motif bind a pocket on the pointed-end p25 subunit, while the glutamate shields the pocket and interacts with N20 on p25 **(Fig. 3.3f)**. In NuMA, the model predicts the Spindly motif sequence is LGDVL. The two leucines (L409 and L413) bind the hydrophobic pocket on p25, whereas a glutamate outside the core motif (E407) contacts N20 **(Fig. 3.3f, Fig. 3.4h)**. Collectively, our structural analysis showed that NuMA binds dynein and dynactin through an HBS1 site and a previously unknown Spindly motif, and that a proposed CC1-box-like motif is not likely involved in complex formation.

To validate our structural model, we introduced point mutations to the acidic patch, proposed CC1-box-like motif, and the Spindly motif of NuMA 1-505, and tested how these modifications affect DDN motility *in vitro* **(Fig. 3.3f-h)**. Consistent with our model, reversing the charges of the critical residues in the acidic patch (mtAP; DELELE → KRLRLR) nearly fully eliminated dynein motility, while previously proposed mutations to the CC1-box-like motif (A363V/A369V)[104] had only a minor effect **(Fig. 3.3g-h)**. Alanine mutations to the critical residues within the Spindly motif that our model predicts (mtSpndly) nearly eliminated dynein motility. A previously suggested position for the Spindly motif[35] is downstream from the predicted sequence but overlaps with it at residue L413. Alanine substitutions to this region (SpM) impaired dynein activity both in cells[35] and in our *in vitro* assays **(Fig. 3.3f-h, Fig. 3.4i)**. Reverting the residue 413 to leucine (L) in SpM (ctrSpM) nearly fully rescued DDN motility, indicating that SpM disrupts dynein motility due to the mutation to the Spindly motif at L413. These results strongly support our structural model and are consistent with the requirement of the Spindly motif in the activation of dynein motility by other adaptor proteins[111,112].

3.3.3 MTBD1 Preferentially Binds the Minus-end of MTs

To understand the interaction of the NuMA C-terminus with MTs, we purified NuMA C (a.a. 1700 - 2115), MTBD1 (a.a. 1811 – 1985; previously referred to as NuMA TIP[48]), and MTBD2 (a.a. 2002 – 2115; **Fig. 3.5a, Fig. 3.6a**). Although earlier studies referred to the NuMA C-terminus as a globular domain[113,114], AF2 predicts that it is almost fully disordered **(Fig. 3.6b)**, consistent with the interaction of this region with a diverse array of cellular factors and its role in liquid-liquid phase separation of NuMA both *in vitro* and *in vivo*[105]. The C-terminal constructs lack the coiled-coil region and primarily appeared as monomers in mass photometry **(Fig. 3.5b)**. We found that

NuMA C, which contains both MTBD1 and MTBD2 sites, appeared both on the lattice and the tip of MTs **(Fig. 3.5c, Fig. 3.6c)**. Consistent with a previous report[45], MTBD1 weakly interacted with the MT lattice. However, it mostly appeared as bright puncta at the tip of a subset of MTs. In comparison, MTBD2 densely decorated the MT lattice, albeit at a lower degree than NuMA C **(Fig. 3.5c)**. NuMA constructs that lack the C-terminus failed to bind MTs **(Fig. 3.6d)**.

Previous studies in live cells hinted that MTBD1 is sufficient for binding of NuMA to minus-ends of MTs, whereas there were conflicting reports on whether MTBD1 or MTBD2 prefers curled ends of MTs and is required for localization of NuMA at the plus-end tip of astral MTs[26,44,48,115]. We quantified the lattice and tip binding preference of NuMA C, MTBD1, and MTBD2 at sub-saturation concentrations **(Fig. 3.5d-e, Fig. 3.6e)**. MTBD1 rarely binds to the lattice and strongly (~80%) prefers binding to the minus-end when it lands on the MT. MTBD2 decorates the lattice even at low concentrations and does not exhibit strong tip binding (~20%), but it prefers to land on the plus-end when it only appears at the MT end. NuMA C exhibits the MT binding features of both MTBD1 and MTBD2, appearing both at the ends and the lattice of MTs, but prefers the minus-end when it only appears at the tip of the MT **(Fig. 3.5d-e)**. These results show that NuMA can recognize and bind to the minus-ends of MTs through MTBD1[26], but it also interacts with the lattice and the plus-end through MTBD2[44,115].

To determine whether MT binding of NuMA regulates MT dynamics, we immobilized MT seeds stabilized with a nonhydrolyzable GTP analog, GMP-CPP, to the glass surface and monitored active polymerization and depolymerization of MTs in the presence of free tubulin, GTP, and NuMA C **(Fig. 3.5f)**. We observed NuMA C binding to both ends and the lattice of dynamic MTs. The accumulation of NuMA C at the MT minus-end almost completely stopped its growth, whereas there was little to no effect on the polymerization dynamics at the plus-end **(Fig. 3.5g)**. These results show that the C-terminal region of NuMA caps and stabilizes the minus-ends of MTs.

We next sought to understand how MTBD2 binds to the MT lattice. The MT association of NuMA C weakened upon increasing the salt concentration to 200 mM KAc **(Fig. 3.6f)**, suggesting electrostatic interactions between NuMA and MTs. The interaction of NuMA C and MTBD2 with MTs was also substantially reduced when the tubulin tails were cleaved by a serine protease, subtilisin, indicating that tubulin tails play an important role in MT binding of NuMA **(Fig. 3.5h, Fig. 3.6g-h)**. To further test whether MTBD2 binds to the globular fold or the flexible tails of polymerized tubulin, we imaged MTs decorated with MTBD2 at near saturation. To reliably distinguish α and β tubulin and determine the MT seam, we co-decorated MTs with a construct that contains the dynein MTBD in a high-affinity state (dynein-MTBD)[116] **(Fig. 3.5i)** and imaged these MTs using cryo-EM. The pseudo-helical reconstruction and symmetry expansion of MTs at 3.3 Å resolution revealed a clear density that corresponds to the dynein-MTBD[116]. However, we did not observe any additional density that could correspond to NuMA MTBD2 **(Fig. 3.5j)**, even though NuMA MTBD2 densely localizes to MTs under these conditions **(Fig. 3.5j)**. These results support that MTBD2 of NuMA interacts with the flexible tails of tubulin, which cannot be directly observed in our cryo-EM reconstruction.

3.3.4 NuMA is Rescued from Autoinhibition by Phosphorylation

We turned our attention to full-length (FL) NuMA, which contains both dynein and MT interaction sites **(Fig. 3.7a)**. Previous studies, which used denaturation/renaturation of NuMA FL and rotary shadow imaging, reported that NuMA forms oligomers with 6-12 long flexible arms[40,106]. We imaged NuMA FL without protein denaturation using negative stain EM. Consistent with these reports, NuMA FL formed clusters that project ~200 nm long and flexible extension arms **(Fig. 3.7b-d)**. In contrast, NuMA 1-1699 only forms ~200 nm long extension arms without clusters **(Fig. 3.7c)**, demonstrating that the C-terminus is responsible for the clustering of NuMA FL, and long extension arms correspond to the coiled-coil domain. Compared to these reports[40,106], we observed NuMA forming larger clusters that project a highly variable number of flexible arms. These discrepancies may be due to the differences in sample preparation. Clustering of NuMA FL was also observed in fluorescence imaging assays **(Fig. 3.8a)**. These observations are in line with the punctate signals of NuMA at the cell cortex[35] and the proposed function of NuMA in crosslinking and focusing MT minus-ends into larger asters in acentrosomal spindles[115].

We next tested how NuMA FL interacts with dynein and MTs. Unlike NuMA C, NuMA FL had a low affinity for MTs and exhibited no clear preference for tip binding **(Fig. 3.8a-c)**. NuMA FL also resulted in ~10-fold less frequent processive runs and ~2-fold slower movement than complexes assembled with NuMA 1-705 under the same conditions **(Figs. 3.1e-f, 3.7e, and 3.8d-e)**. These results indicate that NuMA FL is autoinhibited for its interactions with dynein and MTs.

NuMA autoinhibition may involve interactions between the N- and C-terminal regions mediated by the central coiled-coil, analogous to other cargo adaptors of dynein[95,117,118]. We tested this possibility by truncating the central coiled-coil and the extreme C-terminus of NuMA. NuMA Bonsai, which contains both the N-terminal (1-705) and C-terminal (1700-2115) region, but lacks the intervening coiled-coil domain[20,35], binds to MTs more efficiently than NuMA FL, but less efficiently than NuMA C **(Figs. 3.7f and 3.8a-b)**. It prefers binding to the minus-end of MTs **(Fig. 3.9c)**. NuMA Bonsai also resulted in more frequent dynein runs than NuMA FL, albeit at a lower frequency than NuMA 1-705 **(Figs. 3.1e-f and 3.8d-e)**. A NuMA construct that lacks MTBD2 (ΔMTBD2) very weakly interacted with MTs and preferred to bind the MT minus-end **(Fig. 3.8c)**, consistent with MTBD2 being the main driver of MT binding, and MTBD1 being the site of minus-end recognition of MTs. Unlike NuMA Bonsai, ΔMTBD2 stimulated dynein motility nearly as efficiently as 1-705 **(Fig. 3.8e)**. Collectively, these results indicate that the central coiled-coil is involved in the autoinhibition of dynein binding at the N-terminus and MT binding at the C-terminus. The removal of this region results in partial activation of NuMA, suggesting that the N- and C-terminal regions are also part of the autoinhibitory mechanism, such that the presence of the C-terminus prevents full activation of dynein at the N-terminus and the N-terminus reduces MT binding of the C-terminus. We also note that DDN Bonsai and ΔMTBD2 moved at a similar velocity to that of complexes assembled with NuMA 1-705 **(Figs. 3.1e-f and 3.8e)**, suggesting that the presence of NuMA MTBDs does not cause intermittent pausing or dragging against dynein motility.

We reasoned that NuMA may be rescued from autoinhibition and activated for its mitotic functions through phosphorylation[119,120]. Studies in live cells revealed that, after nuclear envelope breakdown, NuMA is phosphorylated by CDK1 at T2055 to enhance its MT binding and inhibit

its localization to the cell cortex[32,121]. S1969, S1991, and S2047 phosphorylation by Aurora-A kinase facilitates the translocation of NuMA from spindle poles to the cell cortex[122]. NuMA is also phosphorylated by Plk1 at S1833/34 [123], which increases the rate of NuMA turnover at spindle poles and the cell cortex[124]. We generated phosphomimetic mutants of the Aurora A (S1969D, S1991D, and S2047D; 3StoD hereafter)[119,122], CDK1 (T2055D)[121], and Plk1 (S18833/34D)[124] phosphorylation sites and tested how these modifications affect dynein activation of NuMA FL **(Fig. 3.7a)**. Similar to wild-type NuMA FL, these mutants exhibited low affinity to bind MTs **(Fig. 3.9a-b)**. However, they exhibited differences in their end-binding preference. While T2055D was more likely to bind to the plus-end, S1833/34D was preferably localized to the MT minus end **(Fig. 3.9c)**. We concluded that phosphorylation of NuMA at these sites does not substantially affect its MT binding.

Unlike MT binding, all three phosphomimic mutants resulted in up to a 4-fold increase in the run frequency of DDN complexes **(Fig. 3.8f-g)**. The velocity of these complexes was comparable, but their run frequency was still lower than that of DDN complexes assembled with NuMA 1-705 **(Figs. 3.1f-g and 3.9d-e)**. These results indicate that interphase NuMA is autoinhibited for its interactions with dynein and partially activated by mitotic phosphorylation of its C-terminus by Aurora A, CDK1, and Plk1.

3.3.5 Mitotically Phosphorylated NuMA Activates Dynein in Cells

To investigate whether NuMA can activate dynein in cells, we collaborated with Sophie Dumont's laboratory at UCSF. Nathan H. Cho leveraged synthetic activation of dynein in peroxisome transport through chemically inducible dimerization of FRB and FKBP tags upon rapamycin addition **(Fig. 3.10a)**[125]. Peroxisomes typically diffuse freely through the interphase cytoplasm. He exogenously expressed a peroxisome marker (PEX3) fused with mEmerald and FKBP, and fused FRB to different NuMA constructs that lack the NLS motif. If the NuMA construct activates dynein-mediated transport, we expect PEX3-mEmerald to move to the centrosome, where minus-ends terminate, typically in the perinuclear region. Endogenous NuMA was mostly localized to the nucleus during interphase and was not depleted in these assays.

In agreement with our *in vitro* results **(Fig. 3.1)**, we found that NuMA 1-705 efficiently traffics peroxisomes to the centrosome in interphase cells **(Figs. 3.10b-d and Fig. 3.11).** A construct containing the previously predicted Spindly mutation (NuMA 1-705 SpM)[35] fully eliminated trafficking, verifying that trafficking results specifically from NuMA-dynein interactions, as opposed to an indirect mechanism. NuMA-Bonsai, which additionally has NuMA's C-terminus that can bind MTs, also trafficked peroxisomes. Notably, NuMA FL did not cause peroxisomes to cluster. In comparison, phosphomimetic NuMA FL constructs (S1969D and T2055D) trafficked peroxisomes, albeit in a lower percentage of cells compared to NuMA 1-705. Importantly, differences in NuMA expression level or pre-accumulation of NuMA to the centrosome do not explain the differences in trafficking between NuMA FL and phosphomimetic NuMA FL constructs **(Fig. 3.11c-d and g)**. These results are consistent with *in vitro* motility assays **(Fig. 3.8f-g)** and show that NuMA FL can activate dynein in interphase cells when mitotically phosphorylated. Therefore, these post-translational modifications on NuMA might not only control its cellular localization but also enable it to form active DDN complexes with dynein.

3.3.6 NuMA Focuses MTs into Asters Together with Dynein

We next investigated how NuMA affects the organization of MTs with or without dynein. To test whether NuMA can crosslink and bundle MTs, we enabled the free movement of MTs while keeping them near the glass surface using the depletion forces generated by a crowding agent **(Fig. 3.12a)**. In the absence of NuMA, we observed little to no bundling of MTs. NuMA FL was bound to freely floating MTs but did not cause substantial MT bundling, probably due to its low MT affinity. Although NuMA C or MTBD2 lack the coiled-coil region and do not form a dimer, they bundled the MTs to a significant extent[42] **(Fig. 3.12b)**.

To test whether minus-end recognition and dynein activation of NuMA are sufficient to focus MTs into spindles, we mixed freely diffusing MTs and NuMA with or without dynein/dynactin and imaged their accumulation on surface-immobilized MTs **(Figs. 3.12c and 3.13)**. In the absence of dynein and dynactin, NuMA FL constructs decorated the MT surface and occasionally caused bundling and coalescence of MTs, but we did not observe the formation of aster-like MT organization **(Fig. 3.13a)**. Similar results were observed for dynein and dynactin in the absence of NuMA **(Fig. 3.12c)**. Aster formation was also not observed when dynein and dynactin were mixed with either NuMA 1-705 that does not bind MTs or NuMA FL that is mostly autoinhibited and has very low dynein activation.

Remarkably, the addition of dynein, dynactin, and mitotically phosphorylated NuMA FL constructs resulted in a robust assembly of MTs into asters **(Fig. 3.12c)**. During aster formation, typically, NuMA first appears as bright puncta at the minus-end of MTs. The coalescence of these MTs with another MT results in its minus-end-directed transport by DDN. As a result, we observed a large accumulation of NuMA and focusing of MTs from their minus-ends at the center of the asters. Out of the constructs we tested, ΔMTBD2 was most efficient in forming aster-like structures together with dynein and dynactin **(Fig. 3.12c)**, likely because removal of MTBD2 resulted in substantial activation of DDN motility **(Fig. 3.8d)** without affecting the recognition of the minus-ends of MTs through MTBD1 **(Fig. 3.7f)**. These results indicate that both the MT minus-end recognition and dynein activation of NuMA are essential for focusing of the minus-ends into aster-like structures.

3.4 Discussion

We used biochemical reconstitution with purified components and single particle cryo-EM and light microscopy to directly observe how NuMA activates dynein motility, binds MTs, affects MT dynamics, and organizes the MT filaments together with dynein *in vitro*. We demonstrated that the N-terminus of NuMA forms a processive complex with dynein and dynactin, triggering dynein-driven transport when targeted to intracellular cargos in live cells. A puzzling feature of NuMA activation of dynein was the presence of both a Hook domain and a CC1-box-like motif. Our findings suggest that the CC1-box-like motif does not engage with DLIC, implicating the Hook domain as the primary mediator of this interaction. While we cannot exclude that the CC1-box-like motif interacts with dynein in other cellular contexts, our observation that the Hook domain is the only one relevant for the assembly of the full DDN complex is consistent with cellular observations[104]. Our structure also indicates that NuMA binds dynein and dynactin through a unique Spindly motif and HBS1 sequences. These results shed light on the diverse mechanisms by

which dynein and adaptors interact, suggesting a flexible, functionally specific framework for these interactions.

We also characterized the MT binding of MTBD1 and MTBD2 sites at the C-terminal region of NuMA. MTBD2 is the main driver of MT binding by interacting with the C-terminal tails of polymerized tubulin along the length of the MT. In comparison, MTBD1 weakly binds to the MT lattice and recognizes the minus-end of MTs. Minus-end localization of NuMA suppresses the dynamics of growth and shrinkage at this end. It remains to be determined which residues in MTBD1 and MTBD2 are responsible for MT binding. Future studies are also required to reveal whether MTBD1 recognizes the minus-end due to the exposed α-tubulin subunit or unique protofilament angles and curvature at the minus end[126,127].

We found that NuMA FL is autoinhibited for its interaction with dynein. The N-terminal Hook domain and the part of the coiled-coil (1-505 and 1-705) were most effective in the activation of dynein motility, whereas the inclusion of the rest of the coiled-coil (1-1699) disfavored the assembly of DDN complexes. The central coiled-coil may fold onto either of these domains for their inhibition, in line with our previous observation that it prevents NuMA from binding chromosomes at mitosis[20]. The ability of NuMA FL to interact with dynein was most significantly enhanced by the truncation of MTBD2, suggesting that the N-terminus is primarily inhibited by the NuMA C-terminus. Similarly, NuMA FL also weakly interacts with the MTs, suggesting that interactions between N- and C-termini may also block the MT interaction sites at the C-terminus. Future studies will be required to reveal the structure and mechanism of NuMA autoinhibition.

In interphase cells, NuMA is localized to the nucleus and is unable to decorate MTs or interact with dynein. Our peroxisome assays in live cells indicate that NuMA is inhibited from interacting with dynein even if it does not localize to the nucleus in interphase cells, providing molecular insights into the autoinhibition and activation of NuMA during mitosis. The autoinhibitory interactions may play a major role in repurposing NuMA for its diverse array of cellular functions. Our NuMA FL may represent NuMA's interphase state, which does not strongly interact with MTs and dynein. In comparison, the assembly of NuMA with dynein and dynactin was partially activated by phosphorylation of its C-terminus by mitotic kinases Aurora A, CDK1, and Plk1. Full activation of dynein interactions may require other posttranslational modifications or NuMA interaction factors, such as RanGTP and Gαi[38]. Consistent with this view, a recent study reported that activation of dynein by NuMA requires CDK1 phosphorylation of the N-terminus of the coiled-coil[128].

Our results indicate that mitotic phosphorylation of NuMA does not simply regulate NuMA localization, but it is required to activate motility and force generation of dynein for spindle pole focusing and cortical force generation. While the underlying mechanism remains unclear, these phosphorylation events may disrupt some of the autoinhibitory interactions between the N- and C-termini of NuMA and allow NuMA to attain an open conformation to interact with its partners. Notably, these phosphorylation events did not enhance MT binding of NuMA FL, suggesting that other phosphorylation sites or kinases may regulate the interaction of NuMA with the MT. It remains to be determined whether NuMA can attain different conformational states through phosphorylation/dephosphorylation and interacting with binding partners for its specific functions.

Our results are largely consistent with an emergent *in vitro* study of the activation of dynein motility and the MT minus-end recognition of NuMA[129]. Unlike our observation that NuMA FL is autoinhibited, Colombo et al. observed more robust MT interaction and dynein activation of NuMA FL[129]. Discrepancies between these studies may be relevant to differences in construct design and clustering of NuMA, or the usage of nonionic detergent to solubilize NuMA FL[129], which may potentially affect autoinhibitory interactions.

NuMA is a unique dynein adaptor that interacts with MTs at its "cargo binding end", thereby playing a central role in focusing the minus-ends of MTs[46,115]. In spindle poles, most MTs are not directly anchored to the centrosomes[19] but held together by NuMA[21,26,115,130]. Because spindle poles recruit other MT motors, capping proteins, and crosslinkers, it is challenging to dissect the precise role of NuMA and dynein in the minus-end focusing of MTs. We demonstrated that the C-terminal region enables crosslinking of freely floating MTs, presumably due to its clustering and binding to MTs at multiple sites. Neither NuMA nor dynein/dynactin alone could focus or align MTs, but together, they were able to focus minus-ends of MTs in the absence of other proteins. Aster formation requires the accumulation of NuMA at the MT minus-end, consistent with the ability of NuMA to localize to the MT minus-ends in cells, albeit less efficiently, in the absence of dynein[26]. Transport of these MTs by DDN complexes as cargo towards the minus-end of another MT results in focusing and aligning of MT minus-ends into asters with a large accumulation of NuMA at its center. *In vivo* studies showed that focusing MTs into spindle poles also requires minus-end-directed kinesin-14, KIFC1 (HSET)[115] and MT-associated crosslinkers[131]. The *in vitro* reconstitution assay we developed is poised to provide molecular insight into the specific contributions of MT motors, crosslinkers, and adaptors to spindle pole formation.

3.5 Figures

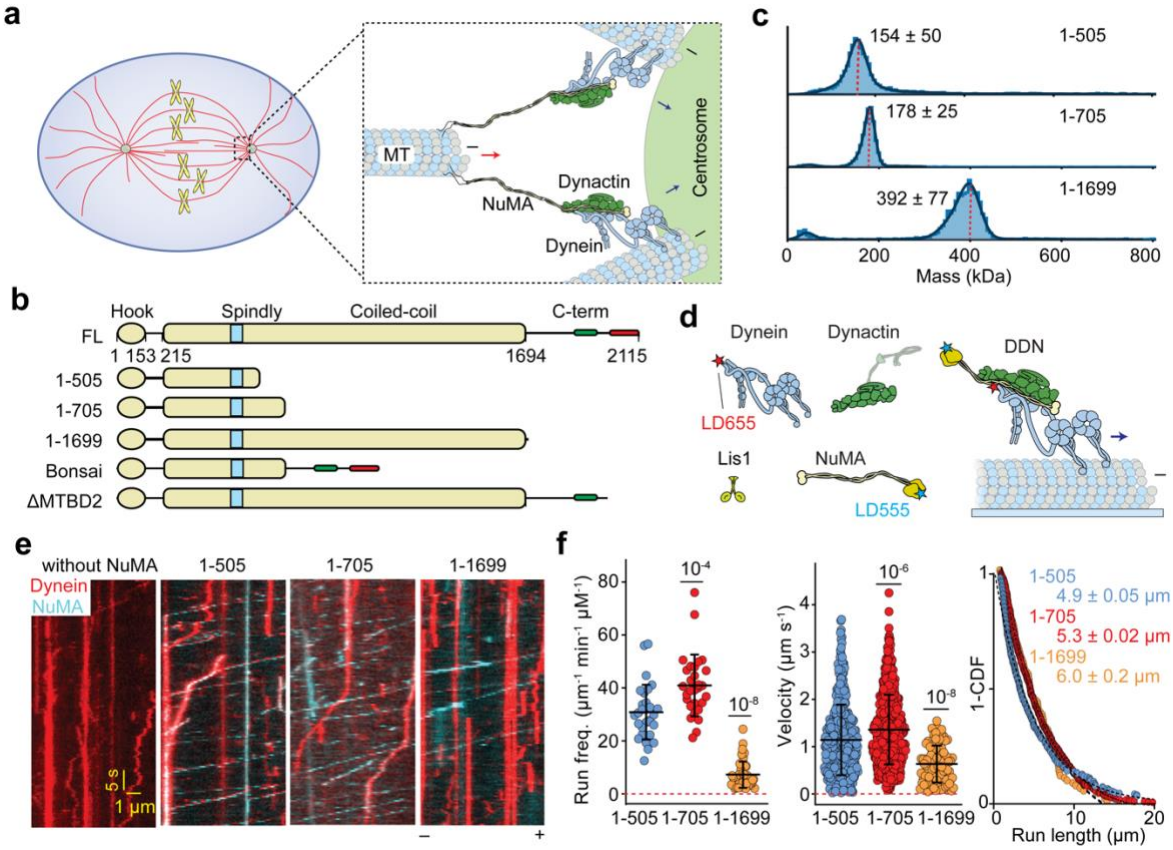

Fig. 3.1. NuMA is a bona fide activator of dynein and dynactin. a. Schematic for the mitotic roles of NuMA at the spindle pole. NuMA recruits dynein/dynactin to the spindle poles, and together, they sort and focus the minus-ends of MTs. DDN complexes move toward the MT minus-end (blue arrows) while NuMA interacts with the minus-ends of MTs as cargo. DDN motility moves the minus-ends of MTs towards the poles (red arrow). **b.** Domain organization and truncations of human NuMA. The Hook domain and the N-terminus of the long coiled-coil recruit dynein and dynactin. The C-terminus is disordered and interacts with MTs and other associated proteins. **c.** Mass photometry shows that NuMA 1-505, 1-705, and 1-1699 form homodimers (mean ± s.d.). Red dashed lines show the expected molecular weights of the dimeric forms of these constructs. **d.** Schematic depiction of the *in vitro* reconstitution and single-molecule imaging of DDN motility on surface-immobilized MTs. Lis1 was added to stimulate the formation of the DDN complex. Dynein and NuMA were labeled with LD655 and LD555 dyes, respectively. **e.** Kymographs show the processive motility of DDN complexes formed with different NuMA constructs *in vitro*. The assays were performed in 1 mM ATP and 100 mM KAc. **f.** The run frequency, velocity, and run length of single DDN complexes. The centerline and whiskers represent mean and s.d., respectively (from left to right, n = 29, 29, and 43 MTs for the run frequency, 418, 682, and 93 motors for the velocity and run length measurements). *P* values are calculated from a two-tailed t-test. The inverse cumulative distribution functions (1-CDF) of motor run length were fit to a single exponential decay to determine the mean run length (±s.e.).

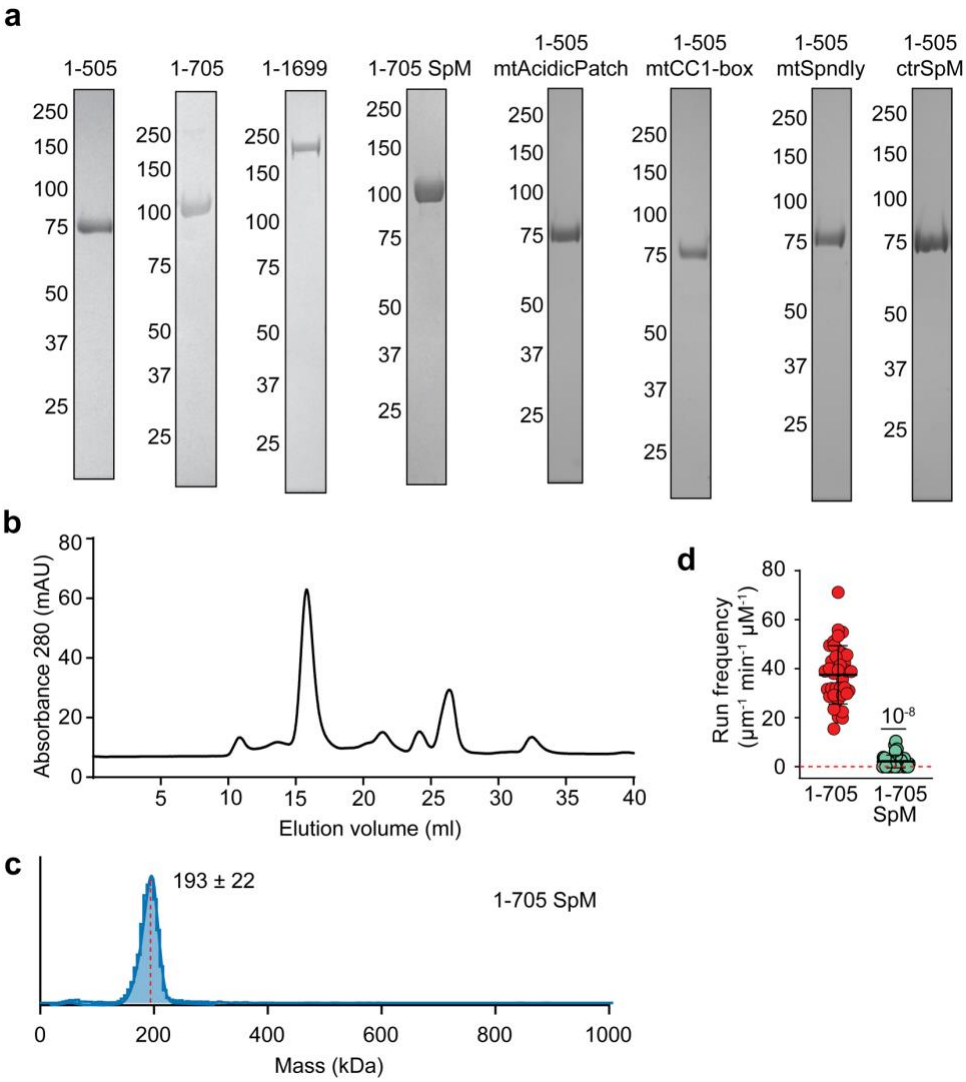

Fig. 3.2. Expression and biochemical characterization of N-terminal NuMA constructs. a. Representative denaturing gel pictures of N-terminal NuMA constructs after gel filtration (n = 3 technical replicates). The numbers on the left represent molecular weight in kDa. **b.** Elution of NuMA 1-505 from a Superose 6 gel filtration column. **c.** Mass photometry shows that NuMA 1-705 SpM forms a homodimer (mean ± s.d.). **d.** The comparison of the run frequencies of single DDN complexes assembled with NuMA 1-705 and NuMA 1-705 SpM. The centerline and whiskers represent mean and s.d., respectively (from left to right, n = 38 and 40 MTs). The *P* value is calculated from a two-tailed t-test. The velocity and run length of complexes formed with NuMA 1-705 SpM could not be determined due to the infrequency of processive runs.

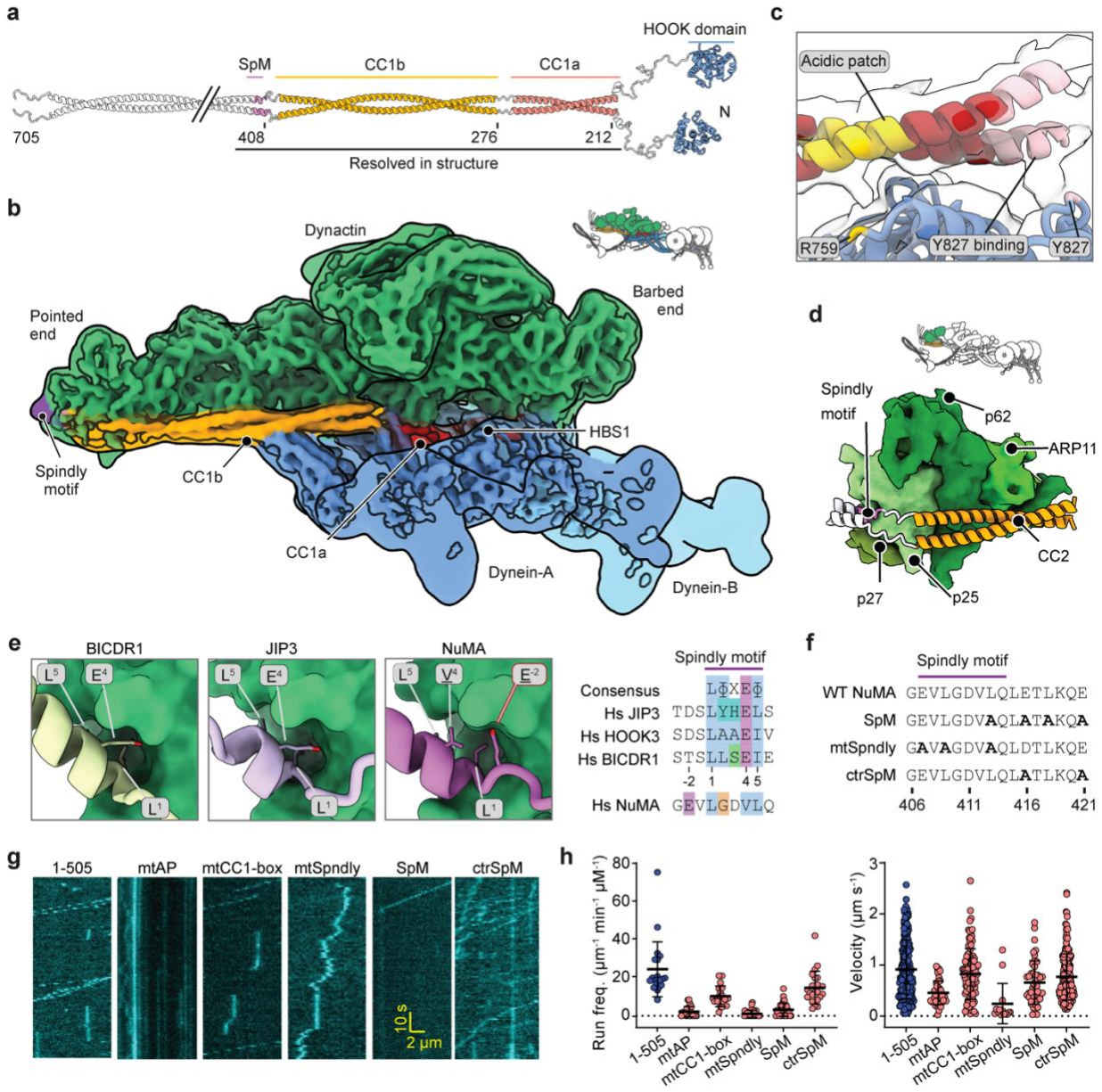

Fig. 3.3. Cryo-EM structure of the DDN complex. a. Linearized AF2 prediction of NuMA 1-705 shown in the C-to-N direction. Only the CC1a, CC1b, and the Spindly motif are resolved. **b.** EM density map of dynein-dynactin bound to NuMA and Lis1 on MTs. The coiled-coil of NuMA runs along dynactin and recruits two dyneins to dynactin. The schematic on the bottom left shows the structure of dynein-dynactin-adaptor complexes on MTs. The dynein motor domains, p150 arm, and Lis1 are not resolved. **c.** Cryo-EM density and model of the NuMA HBS1-DHC interfaces. **d.** AF2 model of the NuMA interaction with the dynactin pointed end. Individual dynactin subunits are labeled. **e.** Spindly motif interactions with the dynactin pointed end in BICDR1 (PDB: 7Z8M), JIP3 (PDB: 8PR4), and NuMA (AF2, this study) illustrate the different positions of the residues highlighted in a multiple sequence alignment on the right. **f.** The design of the mutants introduced to the Spindly motif of NuMA. **g.** Example kymographs show the motility of DDN complexes assembled with WT and mutant NuMA 1-505 constructs. The assays were performed in 1 mM ATP and 100 mM KAc. **h.** The run frequency and velocity of single

DDN complexes. The centerline and whiskers represent mean and s.d., respectively (from left to right, n = 21, 22, 19, 27, 31, and 22 MTs for the run frequency and 254, 42, 104, 14, 44, and 199 motors for velocity measurements).

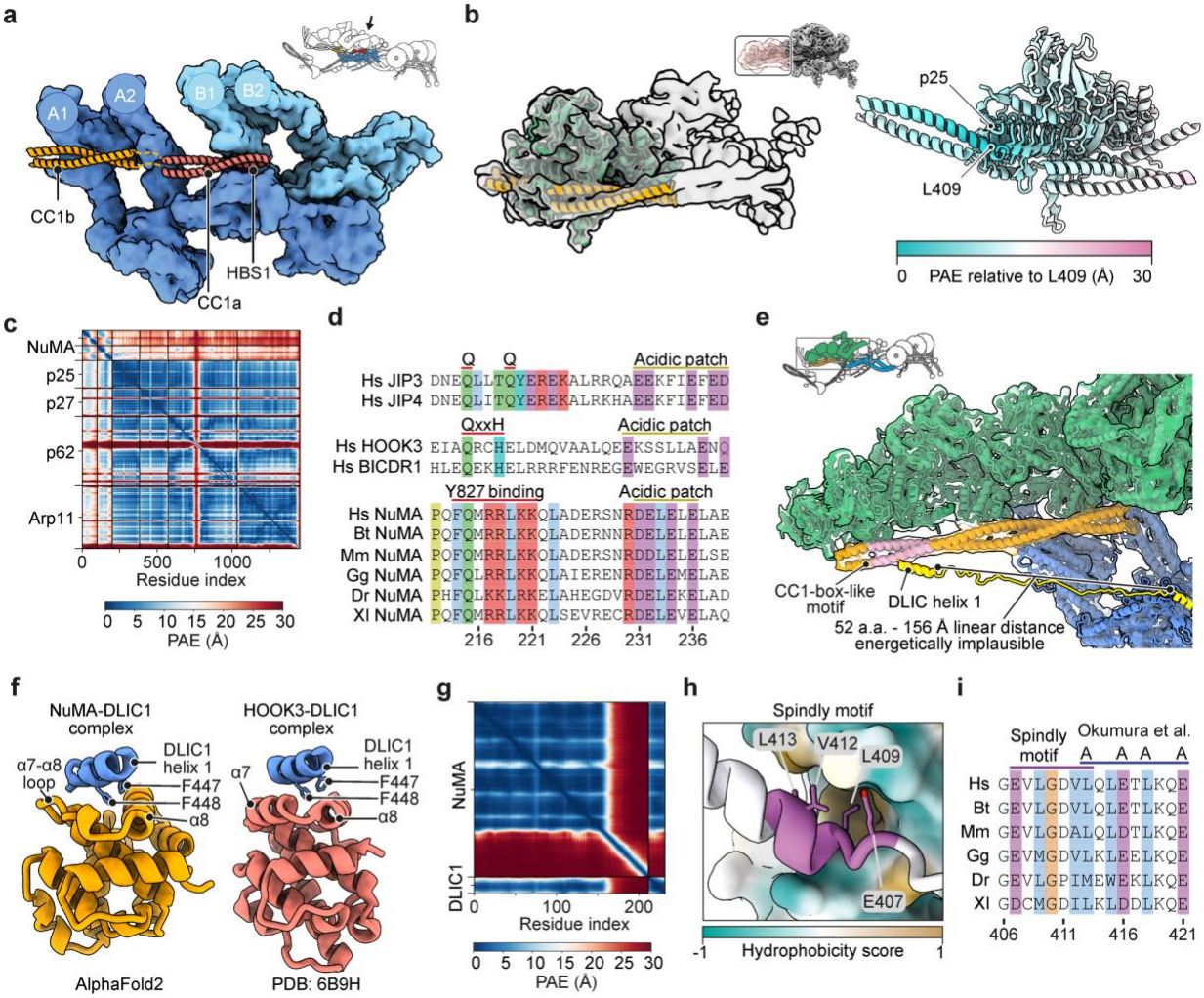

Fig. 3.4. Structural analysis of the interactions between NuMA and dynein-dynactin. a. The organization of the dynein-A and dynein-B interactions with the NuMA coiled-coil, with the dynactin subunits hidden. The arrow in the insert shows the viewing angle of the DDN complex. A1- A2 and B1-B2 are heavy chains of Dynein-A and Dynein-B shown in Fig. 2b. **b.** Fitting of an AF2 model of NuMA 351-450 bound to the dynactin pointed end complex into a locally refined EM density for the same region of dynactin, with the mask used and model colored by local predicted alignment error (PAE) values. Residues with low predicted local distance difference test (pLDDT) scores are hidden. **c.** The PAE plot for the NuMA-Pointed end model in b. **d.** Multiple sequence alignment of HBS1 from NuMA orthologs. Other activating adaptors with known HBS1 sequences are shown for comparison. **e.** Close-up view of the CC1-box-like motif (pink) on NuMA in our EM density. A model of the DLIC tail with the unstructured region extended illustrates that the interaction is likely unfavored due to the distance. **f.** Comparison between the AF2 model of the NuMA Hook domain interaction with DLIC1 and the published structure of the complex between the HOOK3 hook domain and DLIC1 (PDB 6B9H)[110]. Residues outside of the HOOK domain and DLIC are not displayed. **g.** The PAE plot for the NuMA-DLIC1 model in f. **h.** The Spindly motif of NuMA bound to the p25 subunit of dynactin, colored by hydrophobicity. **i.** Sequence alignment of the Spindly motif in NuMA orthologs, with the location of the mutations from Okumura et al.[35].

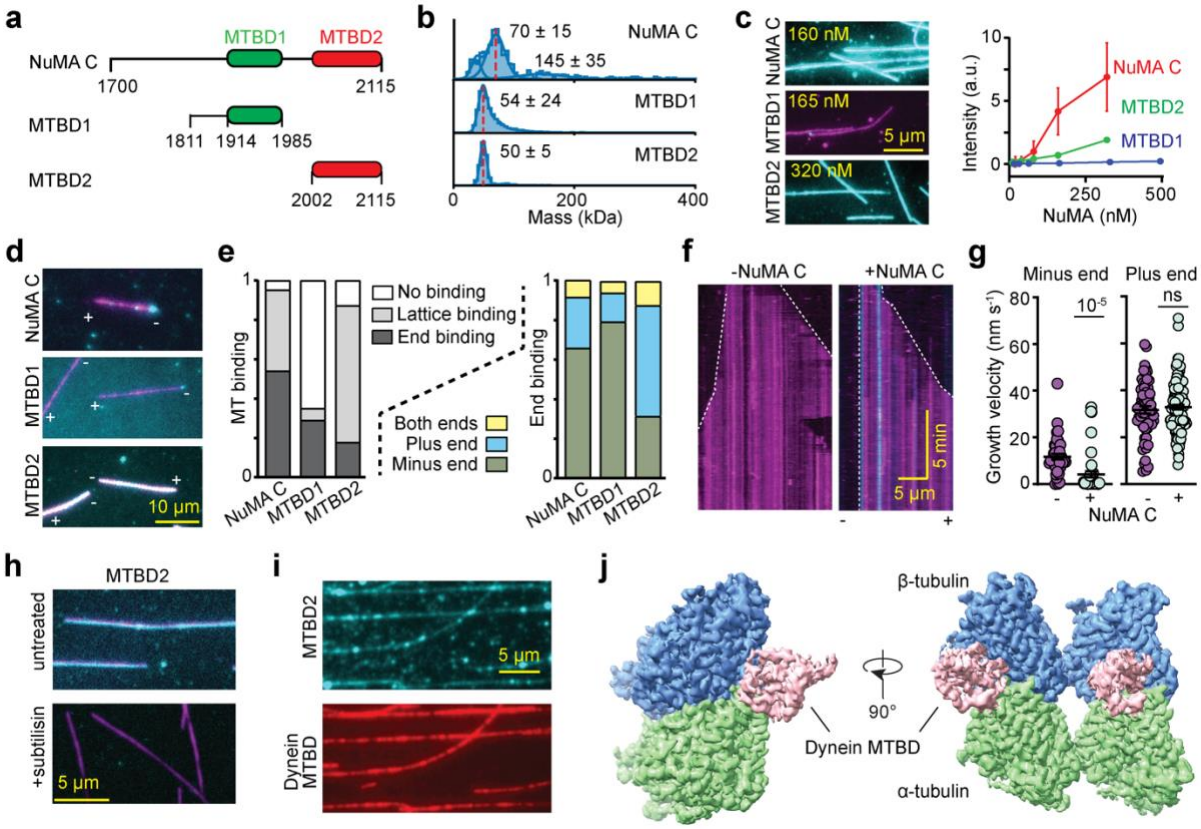

Fig. 3.5. The C-terminus of NuMA preferentially binds to the minus-end of MTs. a. The NuMA C-terminal region (NuMA C) contains two MTBDs (MTBD1 and 2). **b.** Mass photometry shows that the C-terminal constructs primarily form monomers (mean ±s.d.). Red dashed lines show the expected molecular weights of the monomers. **c.** (Left) Example pictures show NuMA C and MTBD2, but not MTBD1, densely decorated surface-immobilized MTs. (Right) The fluorescence intensity of NuMA constructs per MT length (from left to right, n = 282, 324, 328, 320, 316, 348 for NuMA C, 296, 195, 310, 313, 300, 318 for MTBD1, and 254, 200, 201, 206, 200, and 161 for MTBD2). The centerline and whiskers represent mean and s.d., respectively. **d.** Example pictures show MT binding of 25 nM NuMA C, 165 nM MTBD1, and 4 nM MTBD2. MT polarity is determined from the directionality of plus-end-directed Cy5-labeled K490 motors (not shown). **e.** Normalized MT binding and end binding preference of C-terminal constructs (from left to right, n = 107, 117, and 142 MTs). **f.** Kymographs of dynamic MTs with GMPCPP MT seeds in the presence and absence of 100 nM NuMA C. Minus-end accumulation of NuMA C stops its growth and shrinkage. **g.** Growth velocities of the MT plus and minus ends in the absence and presence of NuMA C (from left to right, n = 41, 43, 59, and 126 MT growth events). The centerline and whiskers represent mean and s.e.m., respectively. *P* values are calculated from a two-tailed t-test. **h.** MTBD2 exhibits little to no binding to subtilisin-treated MTs. **i.** MTs are co-decorated with 50 nM MTBD2 (cyan) and 500 nM dynein-MTBD (red). **j.** Cryo-EM reconstruction of the co-decorated MTs only shows density corresponding to dynein-MTBD. No additional density that could correspond to NuMA was observed. In c, d, f, and h, NuMA and MTs are colored in cyan and magenta, respectively. In d, h, and i, n = 3 technical replicates.

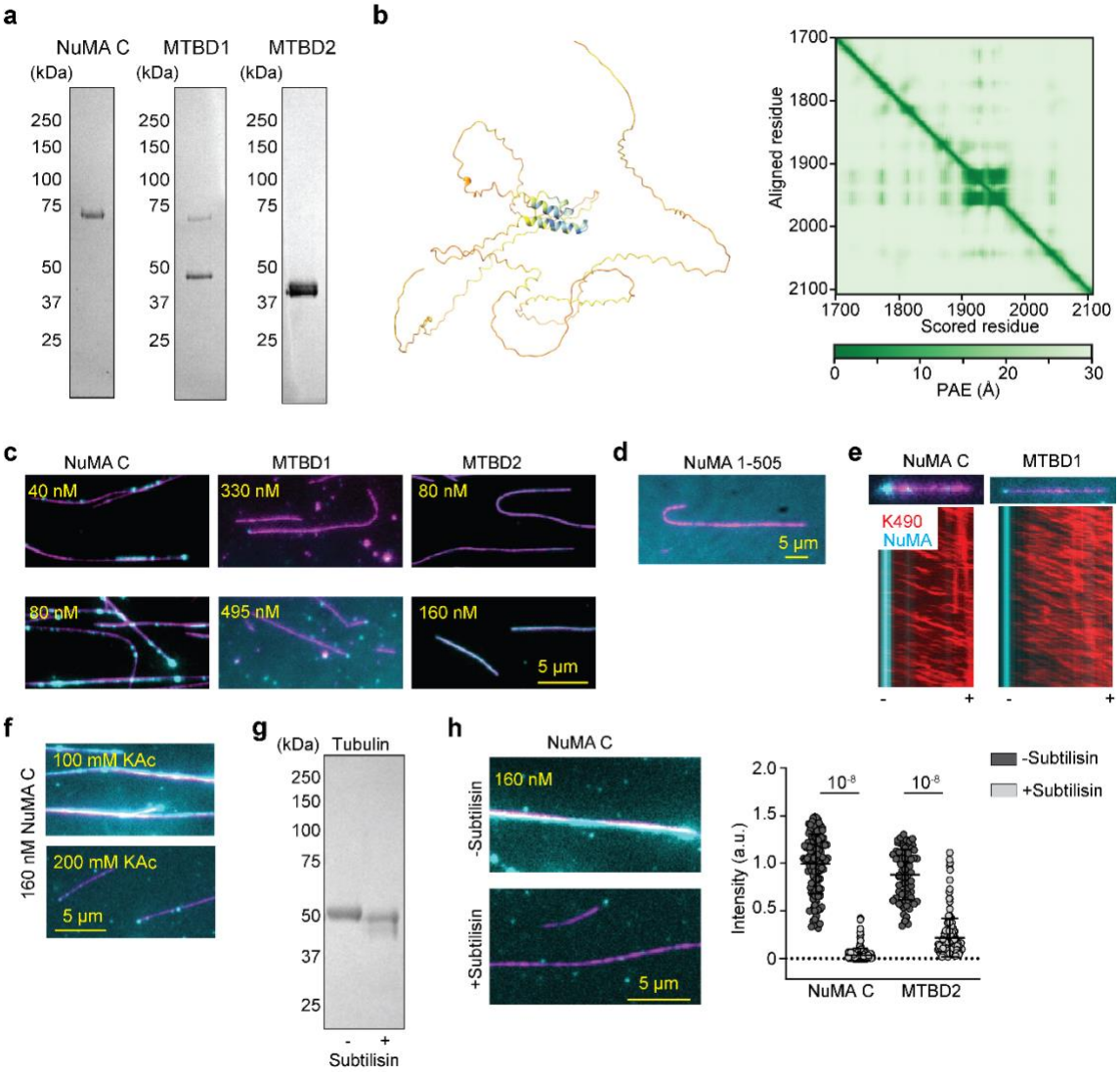

Fig. 3.6. Biochemical characterization and MT binding of C-terminal NuMA constructs. a. Representative denaturing gel pictures of C-terminal NuMA constructs after gel filtration. **b.** (Left) AF2 predicts that the NuMA C-terminus is almost fully unstructured except for a single short helix in MTBD1. (Right) PAE for the model. **c.** Example pictures show NuMA C and MTBD2, but not MTBD1, densely decorated surface-immobilized MTs. **d.** An example picture shows that NuMA 1-505 (cyan) in the flow chamber does not bind to MTs (magenta). **e.** Two-color kymographs of tail-truncated kinesin-1 (K490; red) and NuMA C or MTBD1 (cyan) on the MT. MT polarity was determined from the plus-end-directed motility of K490 motors. NuMA accumulates at the minus-end of the MTs. **f.** MT binding of NuMA C is greatly reduced by increasing the salt concentration from 100 mM to 200 mM. **g.** The denaturing gel picture shows the reduction of the molecular weight of tubulin due to the cleavage of tubulin C-terminal tails by subtilisin treatment. **h.** (Left) NuMA C exhibits little to no binding to subtilisin-treated MTs. (Right) The normalized fluorescence intensity of 300 nM NuMA C and 50 nM MTBD2 on surface-immobilized MTs in the presence and absence of subtilisin treatment. The centerline and whiskers represent mean and s.d., respectively (from left to right, n = 119, 166, 70, and 174 MTs). *P* values are calculated from a two-tailed t-test. In a, c, d, e, f, and g, n = 3 technical replicates.

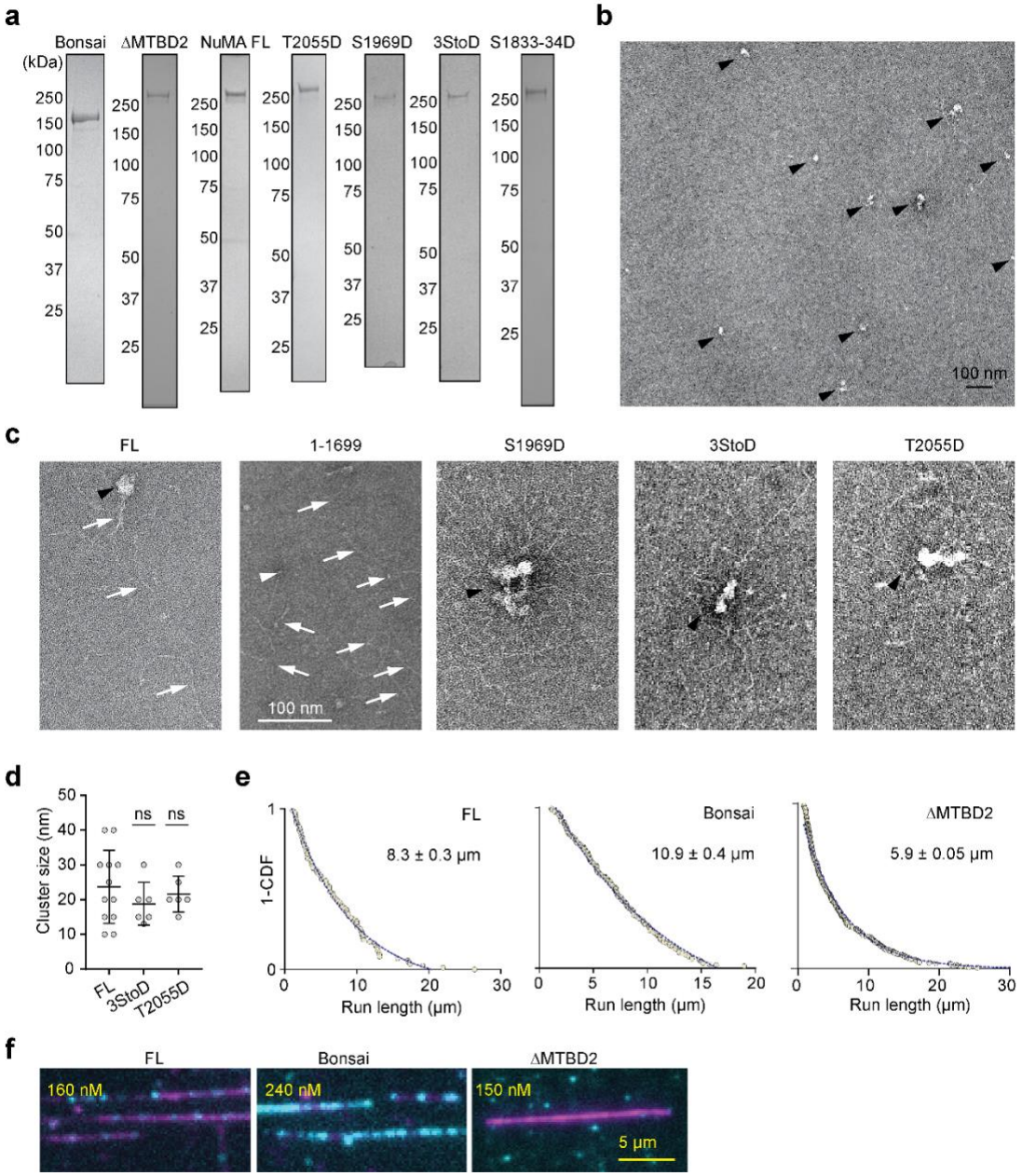

Fig. 3.7. Expression and characterization of NuMA FL constructs. a. Denaturing gel pictures of NuMA constructs after gel filtration. **b.** An example negative stain EM micrograph shows clustering of NuMA FL (black arrowheads). **c.** An example negative-stain EM micrograph shows that NuMA FL constructs form large clusters (black arrowheads) with coiled-coils pointing outward (white arrows). In comparison, NuMA 1-1699 forms only elongated coiled coils. **d.** The size of the clusters formed with NuMA constructs in a. The centerline and whiskers represent mean and s.d., respectively (from left to right, n = 12, 6, and 6 clusters). *P* values are calculated from a two-tailed t-test. **e.** The run lengths of single DDN complexes assembled with NuMA FL, Bonsai, and ΔMTBD2 constructs (from left to right, n = 87, 154, and 360 motors). 1-CDFs of motor run length were fitted to a single exponential decay (blue dashed curves) to determine the mean run

length (±s.e.). **f.** Example pictures show binding of NuMA FL, Bonsai, and ΔMTBD2 (cyan) to MTs (magenta). In a, b, c, and e, n = 3 technical replicates.

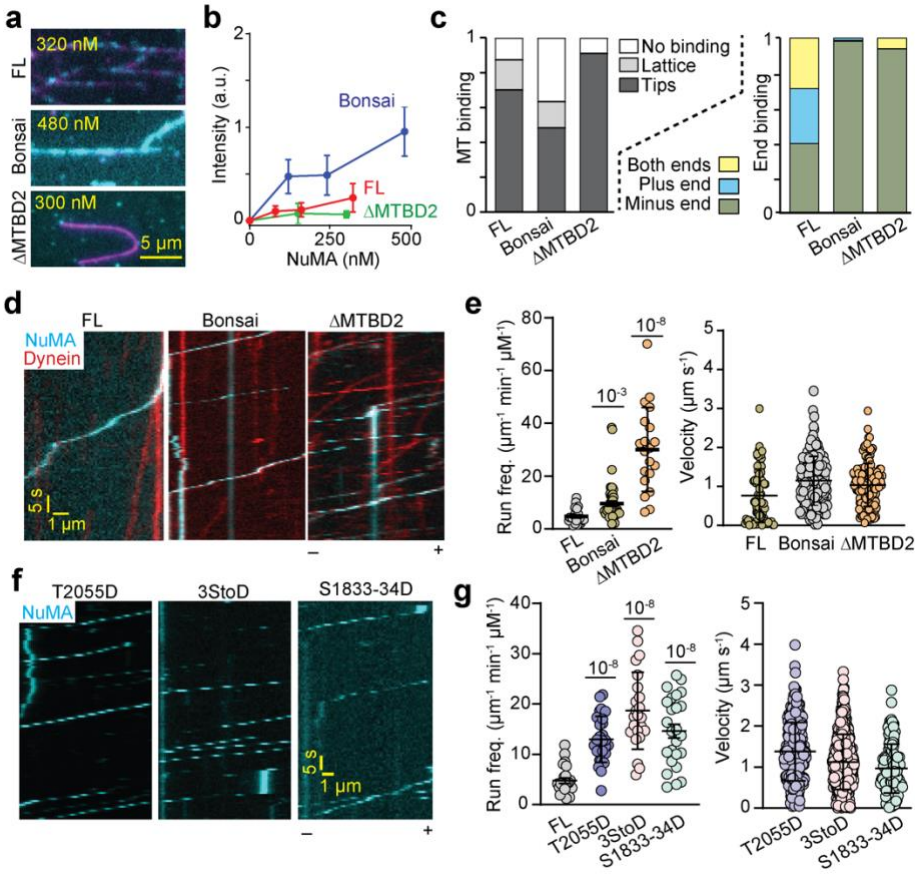

Fig. 3.8. Dynein interaction of NuMA FL is activated by the phosphorylation of its C-terminus. a. Example pictures show MT (magenta) binding of NuMA FL, Bonsai, and ΔMTBD2 (cyan) under different concentrations (n = 3 technical replicates). **b**. The intensity of NuMA constructs fused to mNeonGreen (mNG) per MT length (from left to right, n = 30, 203, 203, 348 MTs for NuMA FL; 30, 251, 237, and 276 for Bonsai; and 30, 48, 68 MTs for ΔMTBD2). **c.** Normalized MT binding and end binding preference of 150 nM NuMA FL, 120 nM Bonsai, and 300 nM ΔMTBD2 (n = 104,126, and 91 MTs, from left to right). **d**. Kymographs show processive motility of DDN complexes assembled with NuMA FL, Bonsai, and ΔMTBD2. **e**. The run frequency and velocity of DDN complexes assembled with NuMA FL, Bonsai, and ΔMTBD2 (from left to right, n = 24, 52, and 20 MTs for the run frequency and 85, 154, and 152 motors for the velocity measurements). **f.** Kymographs show the processive motility of DDN complexes assembled with phosphomimetic mutants of NuMA FL. The NuMA signal appears discontinuous due to time sharing with other fluorescent channels (not shown). **g.** The run frequency and velocity of DDN complexes assembled with phosphomimetic mutants of NuMA FL (from left to right, n = 24, 28, 23, and 25 MTs for run frequency and 286, 435, and 136 motors for velocity measurements)**.** In b, e, and g, the centerline and whiskers represent mean and s.d., respectively. *P* values are calculated from a two-tailed t-test.

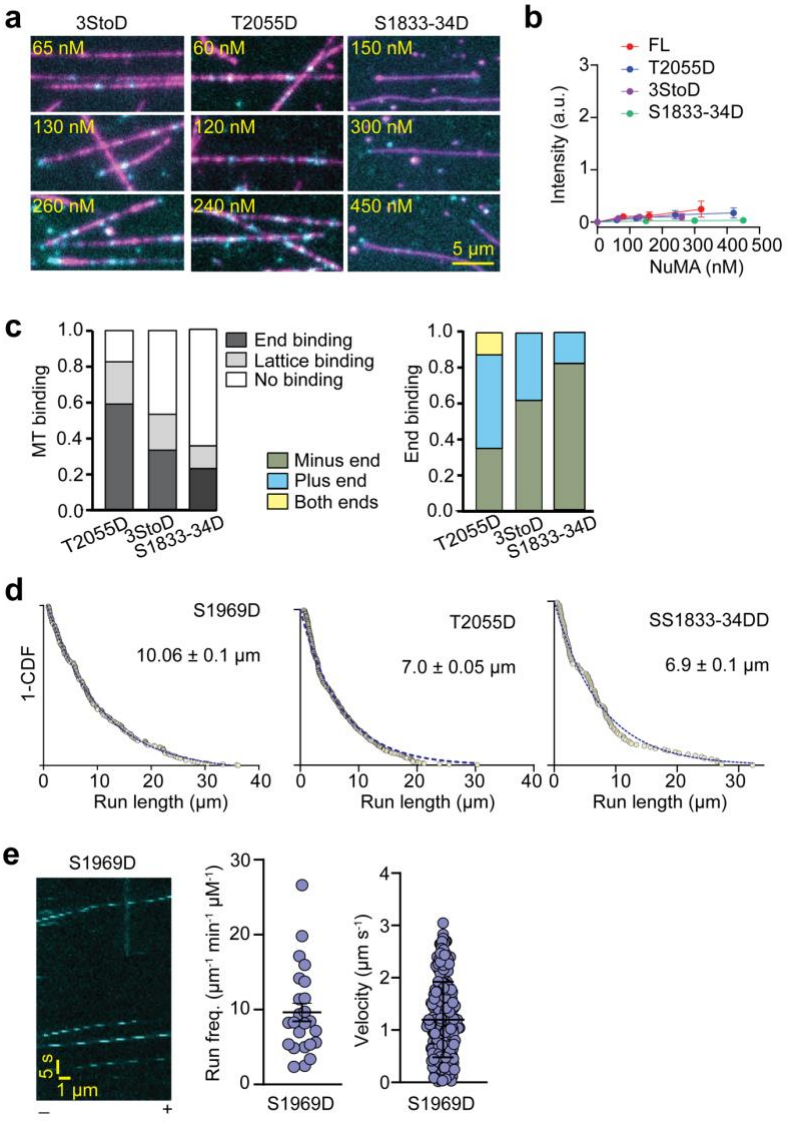

Fig. 3.9. MT binding and DDN motility of phosphomimetic mutants of NuMA. **a.** Example pictures show MT (magenta) binding of NuMA 3StoD and T2055D (cyan) under different concentrations (n = 3 technical replicates). **b**. The intensity of mitotically phosphorylated NuMA constructs per length of an MT. The centerline and whiskers represent mean and s.d., respectively (from left to right, n = 30, 203, 203, 348 MTs for NuMA FL; 30, 362, 394, 349, and 336 for T2055D; 30, 296, 301, 304 for 3StoD; 25, 156, 92, and 186 for S1833/34D). **c.** Normalized MT binding and end binding preference of mitotically phosphorylated NuMA constructs (from left to right, n = 178, 150, and 272 MTs). **d.** The run lengths of single DDN complexes assembled with mitotically phosphorylated NuMA constructs (from left to right, n= 243, 377, and 136 motors). 1-CDFs of motor run length were fitted to a single exponential decay (blue dashed curves) to determine the mean run length (±s.e.). **e.** An example kymograph, run frequency, and velocity of single DDN complexes assembled with S1969D. The centerline and whiskers represent mean and s.d., respectively (n= 24 MTs for the run frequency and 243 motors for velocity measurements).

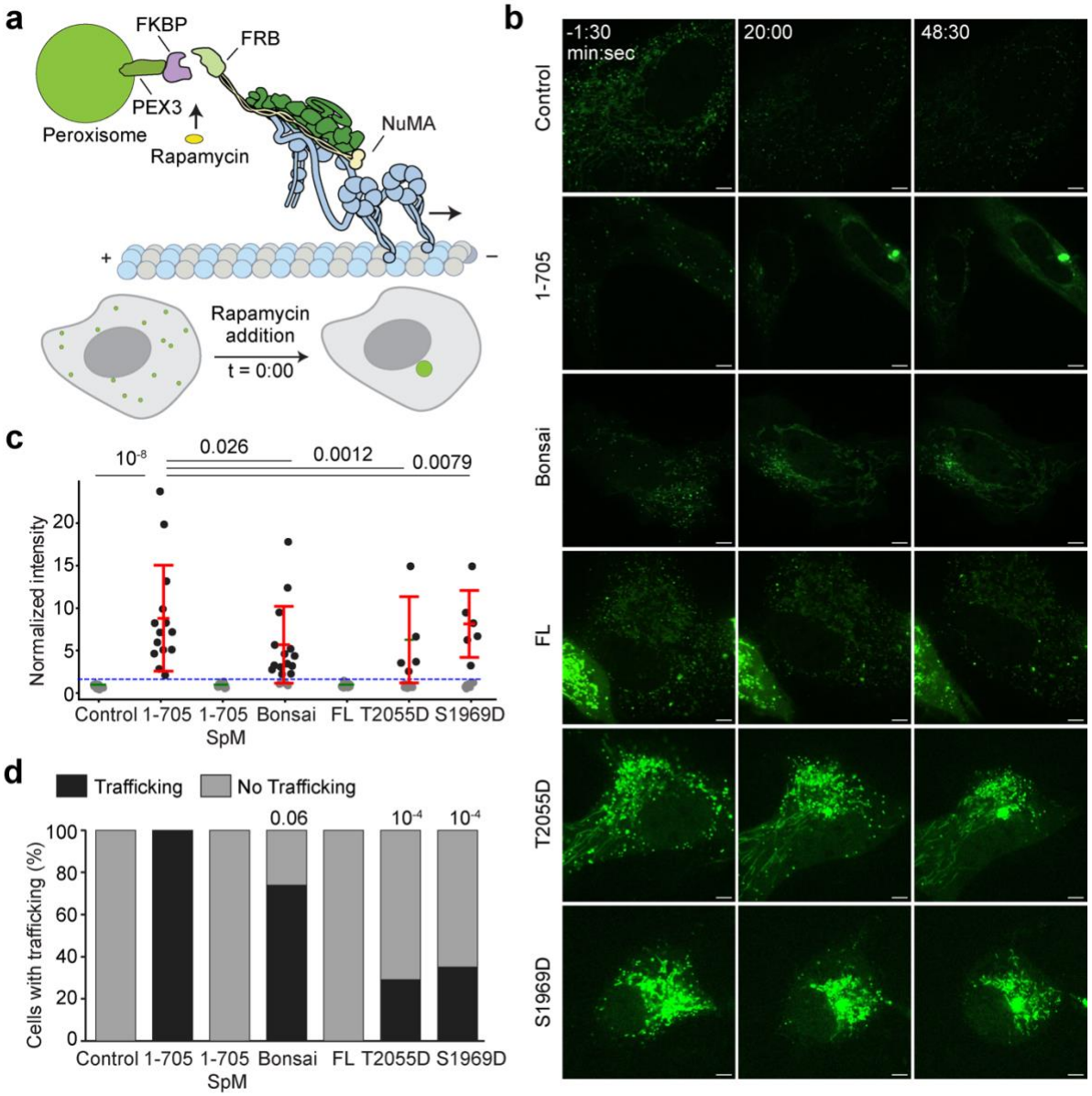

Fig. 3.10. Mitotically-phosphorylated NuMA activates dynein in interphase cells. a. Cartoon depiction of the peroxisome trafficking assay. Rapamycin addition (time 0:00) induces recruitment of a NuMA construct to peroxisomes. If the NuMA construct activates dynein, these peroxisomes are trafficked towards the centrosome. **b.** Representative confocal images of peroxisomes (PEX3, green) before and after rapamycin addition in WT RPE1 cells (control) and RPE1 cells expressing different NuMA constructs. PEX3-mEmerald-FKBP levels vary between cells due to variations in transfections. Scale bar = 5 µm. **c.** The ratio of final (45 min after rapamycin addition) mEmerald intensity to initial mEmerald intensity at the centrosome. Cells were scored as trafficking (black) if the ratio was above the threshold (2, blue dashed line) or no trafficking (grey) if below the threshold (from left to right, n = 16, 14, 15, 19, 22, 17, and 17; two independent experiments). Error bars represent mean ±s.d. of trafficking cells. *P* values are calculated from a two-tailed t-test and Fisher's exact test, respectively, in comparison to the 1-705 condition. **d.** Percent of cells with peroxisome trafficking, from the same samples as c.

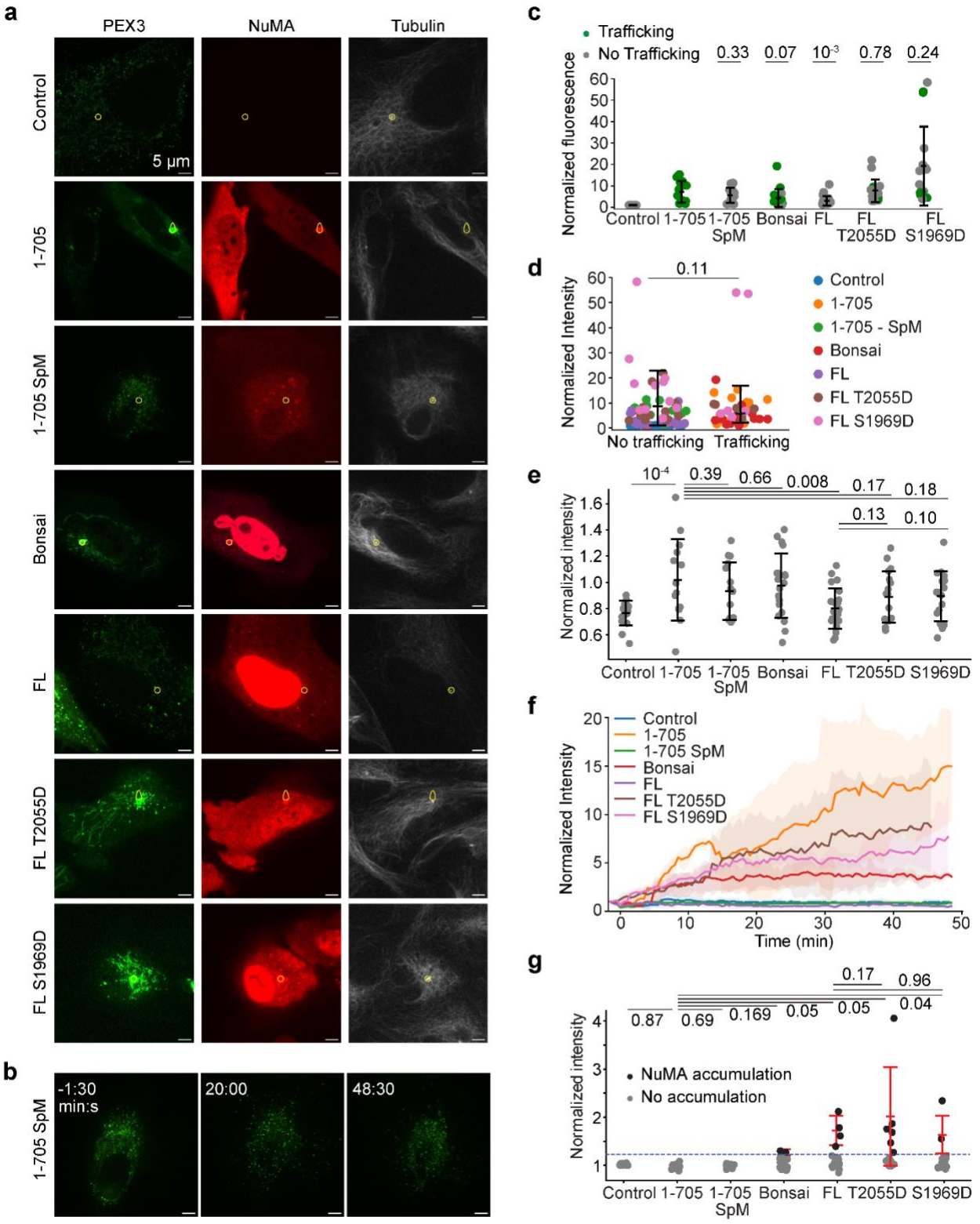

Fig. 3.11. The analysis of peroxisome trafficking assays. a. Representative confocal images of peroxisomes (PEX3, green), NuMA (red), and tubulin (SiR-tubulin, grey) from z-stacks taken 45

minutes after rapamycin addition in WT RPE1 cells (control) and RPE1 cells expressing different NuMA constructs (n = 3 technical replicates). Centrosomes (white dots in the tubulin channel) and consequently the area of quantification is marked by the yellow circle in each still. Cells are the same as in Fig. 5b. **b.** Representative confocal images of peroxisomes (PEX3, green) before and after rapamycin addition in RPE1 cells expressing NuMA 1-705 SpM. Scale bar = 5 µm. **c.** Normalized cytoplasmic NuMA concentration was calculated by averaging the mean pixel intensity for NuMA in the cytoplasm from the timepoints before rapamycin addition. **d.** Normalized cytoplasmic NuMA concentration sorted by trafficking outcome. **e.** The ratio of the final (45 min after rapamycin addition) mEmerald intensity to the initial mEmerald intensity in cytoplasm. No cells showed cytoplasmic accumulation over the threshold (2). **f.** Average peroxisome signal accumulation over time using normalized mEmerald intensity, from a subset of cells where the centrosome (marked by SiR-tubulin) stayed in focus for the majority of frames. For NuMA 1-705, Bonsai, T2055D, and S1969D, only cells that had trafficking were tracked. Time points where the centrosome was out of focus were excluded. Shading represents s.d. From top to bottom, n = 7, 4, 5, 4, 2, 3, and 3 cells pooled from two independent experiments. **g.** Normalized centrosomal NuMA concentration was calculated by averaging the mean pixel intensity for NuMA at the centrosome for the timepoints before rapamycin addition. Cells were scored as either NuMA accumulation (black) if the normalized intensity is above 1.2, or no accumulation (grey) if below the threshold. In c, d, e, and g, n = 16, 14, 15, 19, 22, 17, and 17 cells from left to right (two independent experiments), and the centerline and whiskers represent mean and s.d., respectively. *P* values are calculated from a two-tailed t-test.

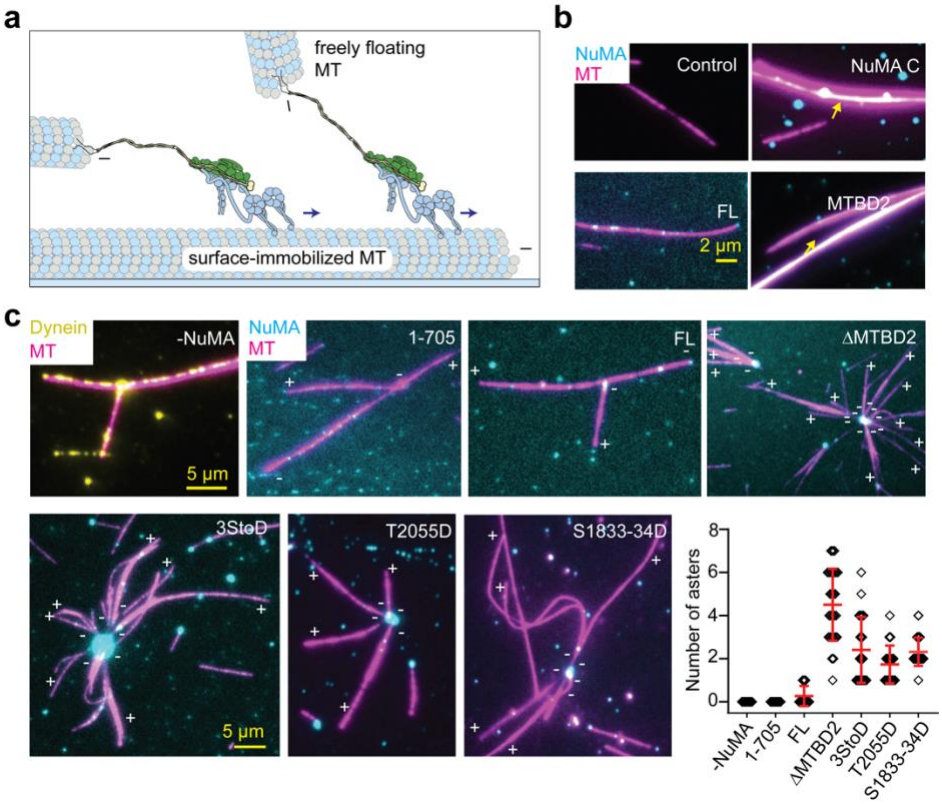

Fig. 3.12. NuMA focuses MT minus-ends into asters with dynein/dynactin. **a.** Schematic shows alignment and focusing of the minus-end of the freely floating MTs to the minus end of a surface-immobilized MT by the DDN complex. **b.** Example pictures show that NuMA FL weakly interacts with freely diffusing MTs, whereas NuMA C and MTBD2 form MT bundles (yellow arrows). **c.** Example pictures show the organization of MT minus-ends into aster-like structures in the presence of NuMA, dynein, and dynactin. MT polarity is determined from the minus-end-directed motility of DDNs (not shown). The disappearance of the MT signal near the center of the asters in DDN 3StoD and T2055D conditions is due to the bending of MTs in the z direction near the NuMA cluster, which positions them away from the evanescent field of TIRF excitation. (Bottom right) The number of asters detected in an 80 μm x 80 μm imaging area in the presence of different NuMA constructs. Asters were defined as the coalescence of the minus ends of at least three MTs (from left to right, n = 10, 10, 11, 28, 24, 19, and 31 images). The centerline and whiskers represent mean and s.d., respectively. In b and c, NuMA, MTs, and dynein are colored in cyan, magenta, and yellow, respectively.

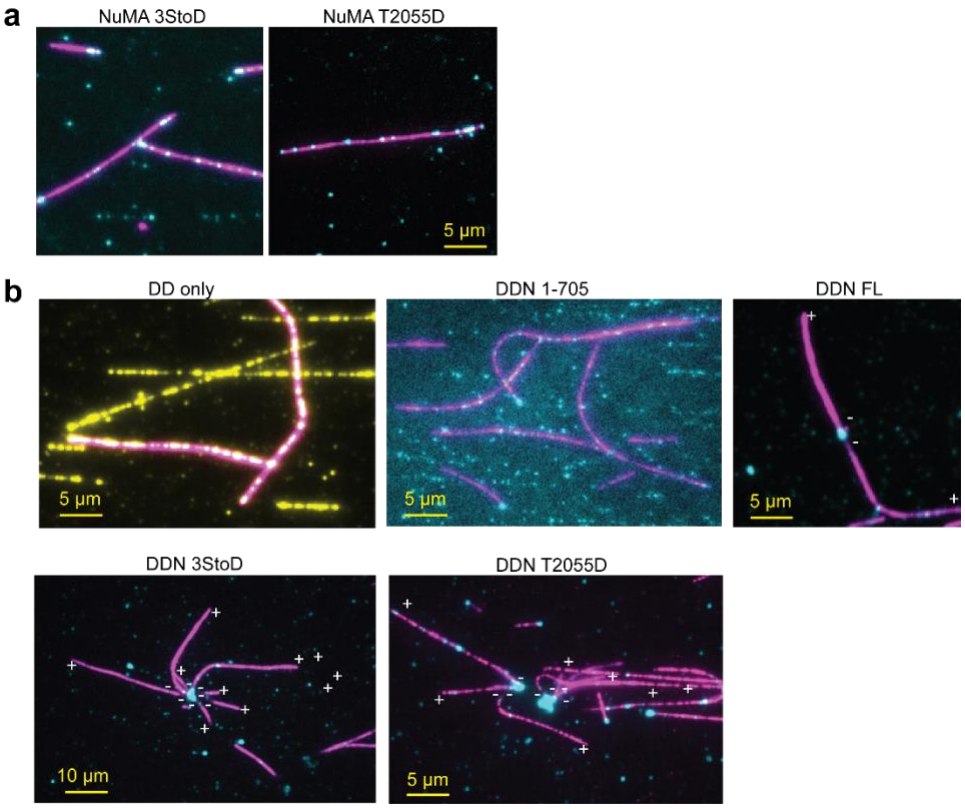

Fig. 3.13. Additional examples of the organization of MTs into aster-like structures by DDN. **a.** NuMA 3StoD and T2055D bind to freely diffusing MTs but cannot bundle MTs or form MT asters in the absence of dynein/dynactin (n = 3 technical replicates). **b.** Additional examples of the organization of MTs into aster-like structures by active DDN complexes formed by NuMA 3StoD and T2055D (n = 3 technical replicates). These structures were not observed in the absence of NuMA (DD only) or the presence of NuMA FL and NuMA 1-705. MT polarity was determined from the plus-end-directed motility of Cy5-labeled K490 (not shown). Dynein, NuMA, and MTs are colored yellow, cyan, and magenta, respectively.

	DDNL consensus	Pointed end with NuMA
EMDB ID	52171	52172
PDB ID	9HHL	-
Data collection		
Voltage	300 kV	300 kV
Electron exposure	40 $e^-/Å^2$	40 $e^-/Å^2$
Magnification	81000x	81000x
Pixel size	1.059 Å/px	1.059 Å/px
Defocus range	-1.2 to -2.2 µm	-1.2 to -2.2 µm
Total micrographs	44,287	44,287
Initial particle images	1,418,923	1,418,923
Final particle images	8,092	8,092
Map resolution	6.53 Å	6.78 Å
FSC threshold	0.143	0.143
Sharpening B-factor	-202	-380
Model refinement		
Model Resolution	8.8	-
FSC threshold	0.5	-
Model composition		-
Non-hydrogen atoms	64693	-
Protein residues	13016	-
Ligands	Zn: 3 ADP: 8 ATP: 2	-
RMSD deviations		
Bond lengths	0.004 Å	-
Bond angles	1.190 ˚	-
Validation		
Clashscore	3.53	-
MolProbity score	1.33	-
Rotamers outliers (%)	0.00	-
Ramachandran plot		
Favored	96.87 %	-
Allowed	3.10 %	-
Outliers	0.03 %	-

Table 3.1. Cryo-EM data collection and refinement statistics for the DDN complex.

	MT – NuMA MTBD2 – Dynein MTBD
EMDB ID	XXX
Microscope	Arctica
Voltage (kV)	200
Camera	K3
Defocus range (μm)	-0.8-1.8
Automation software	SerialEM
Frames	50
Total dose (electrons/Å^2)	50
Pixel size (Å/pixel)	1.14
Number of micrographs	1815
Starting number of particles (pre-symmetry expansion)	242,128
Number of particles in final map (post-symmetry expansion)	576,069
Map sharpening B factor (Å)	-40
Map sharpening methods	Relion 5
Symmetry	C1
Overall resolution (Å)	3.3
Resolution range of map (min-75th percentile) (Å)	3.1-5.9

Table 3.2. Cryo-EM data collection and refinement statistics for the MTs co-decorated with NuMA MTBD2 and dynein-MTBD.

3.6 Methods

3.6.1 Cloning and plasmid generation

All human NuMA constructs were cloned into the pOmnibac vector, incorporating an N-terminal His6-ZZ tag followed by a TEV protease cleavage site for protein expression and purification and a C-terminal SNAP or mNG sequence for fluorescent imaging. Full-length and C-terminal NuMA constructs were cloned into a vector containing an additional N-terminal MBP tag between the TEV cleavage and the ZZ tag to improve the solubility of expressed proteins. For live cell imaging, the coding sequence of NuMA-HaloTag-FRB constructs (NuMA 1-705, NuMA-Bonsai, NuMA 1-705 SpM, NuMA-FL, NuMA-FL-T2055D, and NuMA-FL-S1696D) were cloned into a puromycin-resistant lentiviral vector (Addgene #114021).

3.6.2 Cell culture

hTERT-RPE1 cells were purchased from ATCC (CRL-4000). Lentivirus was produced in HEK293T cells that were purchased from ATCC (CRL-3216). All cells were grown in DMEM/F12 media (ThermoFisher) supplemented with 10% tetracycline-screened FBS (PS-FB2; Peak Serum) and maintained at 37 °C and 5% CO_2.

3.6.3 Lentiviral plasmids, cell line constructions, and transfections

Lentivirus for each NuMA construct was produced in HEK293T cells. To generate stable polyclonal cell lines, wild-type RPE1 cells were infected with lentivirus and selected using 5 µg mL^{-1} puromycin. PEX3-mEmerald-FKBP (a gift from S. Reck-Peterson, UCSD) was transiently transfected into RPE1 cells to label peroxisomes for 2 or 3 days using Viafect (Promega) according to the manufacturer's recommendations. Tubulin (including the centrosome) was labeled in cells by adding 100 nM SiR-tubulin and 10 µM verapamil for 60 min before imaging (Cytoskeleton). NuMA was labeled with 100 nM Janelia Fluor 549 (Promega) for 15 min before imaging. Rapamycin was added to a final concentration of 1 µM to induce dimerization of FRB-FKBP.

3.6.4 Protein expression and purification

For baculovirus production, pOmnibac plasmids were transformed into DH10Bac competent cells and plated on Bacmid plates containing Bluo-Gal for 48 h at 37°C. Selected white colonies were grown overnight at 37°C in 2xYT medium. Bacmid DNA was purified using isopropanol precipitation and transfected into adherent SF9 cells (10^6 cells mL^{-1}) using FuGENE to produce P1 virus. The cells were cultured for 5–6 days at 27°C, and the P1 virus was harvested when more than 90% of the cells were transfected, as determined by monitoring fluorescent gene expression with a fluorescent light microscope. P2 virus was generated by infecting 50 ml of SF9 cells in suspension with 2 ml of P1 virus for 72 h at 27°C. The P2 virus was harvested by collecting the supernatant after centrifugation of SF9 cells at 4,000 g for 5 min at 4°C.

SF9 cells in 1 L suspension were infected with 1% (v/v) P2 virus and cultured for 72 h at 27°C. The cells were collected by centrifuging at 4,000 g for 10 minutes and washed with ice-cold PBS before being flash-frozen for further purification. Cell pellets were lysed in a lysis buffer supplemented with 1 mM DTT, 2 mM PMSF, and two cOmplete protease inhibitor cocktail tablets

(Roche) per liter of cells using a Dounce homogenizer. The lysate was clarified by centrifugation at 65,000 g for 30 minutes, and the supernatant was incubated with IgG Sepharose beads (Cytiva) for 1 hour at 4°C on a rotator. The beads were loaded onto a gravity-flow column and sequentially washed with a lysis buffer, followed by a wash buffer. The beads-protein mixture was then incubated with 0.1 mg/ml TEV protease overnight at 4°C. Proteins were eluted from the column using gravity flow and concentrated with molecular weight cutoff (MWCO) concentrators (Amicon). Protein concentration was determined by measuring absorbance at 280 nm using a NanoDrop 1000 (Thermo Fisher). Proteins containing a SNAP tag were fluorescently labeled by incubating them with a 5-fold molar excess of BG-LD655 or LD555 dye (Lumidyne). Excess dye was removed by gel filtration.

Dynein-expressing cell pellets were lysed in 50 mM HEPES (pH 7.4), 100 mM NaCl, 2 mM $MgCl_2$, 0.1 mM ATP, and 10% glycerol. The beads-protein mixture was washed with a buffer containing 50 mM Tris-HCl (pH 7.4), 150 mM KAc, 2 mM $Mg(Ac)_2$, 1 mM EGTA, 0.1 mM ATP, and 10% glycerol. The protein was then loaded onto a TSKgel G4000SWXL size exclusion column (Tosoh) for further purification.

KIF5B (1-490) was purified as previously described[81], using a lysis buffer consisting of 50 mM HEPES (pH 7.4), 1 M NaCl, 1 mM DTT, 2 mM PMSF, 2 mM $MgCl_2$, 0.1 mM ATP, and 10% glycerol. The wash buffer contained 50 mM HEPES (pH 7.4), 300 mM NaCl, 1 mM DTT, 2 mM $MgCl_2$, 0.1 mM ATP, and 10% glycerol.

Cell pellets expressing NuMA N-terminal constructs were lysed and washed with 50 mM HEPES (pH 7.4), 300 mM KCl, 1 mM EGTA, and 10% glycerol. The lysate was loaded onto a Superose 6 Increase 10/300 GL (Cytiva) column for size exclusion chromatography in a buffer containing 50 mM HEPES (pH 7.4), 150 mM KCl, 1 mM EGTA, and 10% glycerol.

For NuMA FL purification, cells were lysed in 50 mM HEPES (pH 7.4), 30 mM KCl, 2 mM $MgCl_2$, 1 mM EGTA, and 10% glycerol, supplemented with benzonase nuclease (Sigma). The KCl concentration was then increased to 300 mM before centrifugation. The NuMA FL protein-beads mixture was washed with 50 mM HEPES (pH 7.4), 300 mM KCl, 1 mM EGTA, and 10% glycerol and loaded onto a Superose 6 Increase 10/300 GL (Cytiva) column for size exclusion chromatography in 50 mM HEPES (pH 7.4), 150 mM KCl, 1 mM EGTA, and 10% glycerol.

Cells expressing NuMA C-terminal constructs were lysed in 50 mM HEPES (pH 7.4), 1 M KCl, 1 mM EGTA, and 10% glycerol. The lysate was washed with 50 mM HEPES (pH 7.4), 300 mM KCl, 1 mM EGTA, and 10% glycerol and loaded onto a Superdex 200 Increase 10/300 GL (Cytiva) column for size exclusion chromatography in 50 mM HEPES (pH 7.4), 150 mM KCl, 1 mM EGTA, and 10% glycerol.

Mammalian dynactin was purified as previously described from pig brains using SP Sepharose Fast Flow, MonoQ ion exchange columns (Cytiva), and the TSKgel G4000SWXL size exclusion column (Tosoh)[111].

3.6.5 Cryo-EM sample preparation for DDN

To prepare MTs, porcine brain tubulin was diluted in BRB80 buffer (80 mM PIPES pH 6.8, 1 mM $MgCl_2$, 1 mM EGTA) to a final concentration of 6 µM. GMPCPP was added to a final concentration of 1 mM and polymerization was induced by incubating at 37 ˚C for 1 h. MTs were pelleted by centrifugation at 20,000 *g* for 8 minutes and resuspended in BRB80, after which MTs were depolymerized by incubating 30 min on ice. A second polymerization round was performed by adding GMPCPP to a final concentration of 1 mM and incubating the solution at 37 ˚C for 1 h, followed by another round of centrifugation and resuspension in BRB80. Bradford assay (BioRad) was used to estimate the protein concentration, and MTs were diluted to 0.3 mg mL^{-1} immediately before use.

The DDN 1-705 complex was assembled by mixing the purified dynein, dynactin, Lis1, and NuMA in a 1:2:50:50 molar ratio, respectively, in GF150 buffer (25 mM HEPES pH 7.2, 150 mM KCl, 1 mM $MgCl_2$, 1 mM DTT), with dynein at a final concentration of 0.14 µM in 5 µL. The assembly solution was incubated on ice for 30 min and subsequently diluted 2-fold to a final volume of 10 µL in GF150. To bind the complex to MTs, 9 µL of the complex was mixed with 5 µL of diluted MTs and 9 µL of S1 buffer (25 mM HEPES pH 7.2, 5 mM $MgSO_4$, 1 mM EGTA, 2 mM DTT, 25 mM AMPPNP) and incubated at room temperature for 15 min. MT-bound complexes were separated from unbound protein by pelleting at 20,000 g for 8 min, and then resuspended in 80 µL S2 buffer (25 mM HEPES pH 7.2, 35 mM KCl, 5 mM $MgSO_4$, 1 mM EGTA, 1 mM DTT, 5.3 mM AMPPNP, 0.01% IGEPAL (Millipore-Sigma)). 4 µL of resuspended solution was applied to freshly glow-discharged Quantifoil R2/2 mesh 300 gold grids (Quantifoil) in a Vitrobot IV (ThermoFisher) at 100% humidity and 22 ˚C, incubated for 45 s, and blotted for 1.5 s at a blot force of -15 before plunge-freezing into liquid ethane.

3.6.6 Cryo-EM data acquisition for DDN

The sample was imaged using a FEI Titan Krios (300 kV) equipped with a K3 detector and energy filter (20 eV slit size, Gatan) using automated data collection (ThermoFisher EPU). A total of 44,287 movies was acquired at 81,000X magnification (1.059 Å/pixel), with a 2.32 s exposure time, 40 fractions, and fluence of ~40 $e^-/Å^2$. A 100 µm objective aperture and a defocus range between -1.2 and -2.2 µm were used during image acquisition.

3.6.7 Cryo-EM image processing for DDN

Global motion correction and the contrast transfer function (CTF) estimation were performed using MotionCor2 and CTFFIND4 within RELION 4.0 respectively[132-134]. MTs were initially picked using crYOLO 1.9[135] in single particle mode, utilizing a model trained on manually picked micrographs in filament mode. The coordinates were then resampled at a 4 nm interval using a multi-curve fitting script, resampled coordinates were split into short segments of 10 coordinates each, and MT subtraction was subsequently performed, as previously described[136].

The resulting "once-subtracted" micrographs were fed back into crYOLO for a second, third, and fourth round of MT picking, multi-curve fitting, filament splitting, and subtraction, all using the same parameters as the first round. After the fourth round, the quadruple-subtracted micrographs

were utilized to pick complexes using crYOLO. If no MTs were detected following a given round of subtraction, the last successfully subtracted micrograph was used instead for particle picking.

The picked particles were extracted using RELION 4.0 and imported into CryoSPARC[137], for particle sorting. Each step of sorting was repeated multiple times to minimize the effects of stochastic variations in sorting results, with the best class of all parallel iterations pooled together. Firstly, particles went through a round of heterogeneous refinement using eight reference volumes, out of which six were contaminants, one was a dynein-dynactin-BICD2 complex with two dynein dimers, and one was a dynein-dynactin-BICD2 complex with one dynein dimer. These volumes were previously determined to be effective in isolating *bona fide* dynein-dynactin-adaptor complexes. The one-dynein class degraded during refinement, so only the two-dynein class was taken forward. Heterogeneous refinement was followed by two rounds of 3D classification in cryoSPARC, with masks spanning the entirety of the complex first, and the more stable component afterwards. In each round, the class with the best density for dynein-dynactin-adaptor was taken forward. The particles coming out of the last classification were locally refined and exported into RELION 5.0 for particle polishing and rebinning, after which they were imported again into CryoSPARC for CTF refinement and particle subtraction. A graphical summary of the processing pipeline including particle numbers, FSCs, B-factors, intermediate maps, and masks used for refinements, classifications, and particle subtractions are shown in Extended Data Figure 2.

3.6.8 Model building and refinement of DDN

Model building was performed using ISOLDE[138] and COOT[139], and refinements were performed in PHENIX[140]. Protein Data Bank (PDB) models or AF2 predictions were docked into cryo-EM maps using UCSF ChimeraX[141]. Refinement statistics are available in **Table 3.1**. AF2 models were generated using a local installation of ColabFold 5[142], using MMSeq[143] for homology searches and AlphaFold2-Multimer[144].

To build the full complex model, we docked coiled-coil fragments from an AF2 model of NuMA (1-705) dimer into the adaptor density based on their length and fitted using restrained flexible fitting in ISOLDE. We could not model the linkers between coiled-coil fragments. We have assigned fragments together based on distance, but we could not exclude that the other possible arrangement might be accurate. The model of dynactin and the dynein tails was built using PDB ID 8PTK[109] as the starting model. To model the CC3 fragment, including the Spindly motif and the CC1b-CC2 linker, we used an AF2 model of NuMA (351-450) dimer and the pointed end subunits, which was joined to the CC1b and flexibly fitted with restraints into the density. Using the density from the pointed end subcomplex local refinement, we could assign the CC2 making the Spindly box contacts and the CC1b contacting the side of the pointed end to the same molecule. The linker connecting the other protomer was not resolved and deleted at this stage.

3.6.9 Negative stain EM

Proteins for negative stain were diluted to 20 nM with the following buffer (50 mM HEPES pH 7.4, 150 mM KCl) and 4 µL of sample was applied to homemade carbon-coated grids after glow discharging the grids. Samples were then stained with 1.5% uranyl formate, blotted, and then air dried. Imaging was performed at ~30,000x magnification with a Tecnai 12 microscope.

3.6.10 Fluorescence microscopy

For *in vitro* imaging, a custom-built multicolor objective-type TIRF microscope was used, equipped with a Nikon inverted Ti-E microscope body, a 100X magnification, 1.49 N.A. apochromatic oil-immersion objective (Nikon), and a Perfect Focus System. Fluorescent signals were detected using an electron-multiplied charge-coupled device (EMCCD) camera (Andor, iXon EM+, 512 × 512 pixels), resulting in an effective pixel size of 160 nm after magnification. The mNG, LD555, and LD655 probes were excited by 488 nm, 561 nm, and 633 nm laser beams (Coherent), respectively. The fluorescence signal was filtered using a notch dichroic filter and 525/40, 585/40, and 695/75 bandpass emission filters (Semrock) for the respective probes. Micro-Manager 1.4 was used to control the microscope and acquire movies.

For live cell imaging, cells were plated onto #1.5 glass-bottom 35 mm dishes coated with poly-D-lysine (P35G-1.5-20-C, MatTek Life Sciences) and imaged in a humidified stage-top incubator maintained at 37 °C and 5% CO_2 (Tokai Hit). Cells were imaged on a spinning disk (CSU-X1, Yokogawa) confocal inverted microscope (Eclipse Ti-E, Nikon Instruments) with the following components: Di01-T405/488/568/647 head dichroic (Semrock); 488 nm (120 mW), 561 nm (100 mW), and 639 nm (160 mW) diode lasers; ET525/36M, ET600/50M, and ET676/37M emission filters (Chroma Technology); and an iXon3 Ultra 897 EMCCD camera (Andor Technology). Images were acquired with a 100x 1.45 Ph3 oil objective (Nikon Instruments) using Micromanager 2.0.0.

3.6.11 Flow chamber preparation

For *in vitro* fluorescence imaging assays, polyethylene glycol (PEG)-coated coverslips were used to prevent nonspecific surface binding of proteins. The coverslips were washed with water, acetone, and water again, each for 10 min in an ultrasonic cleaner. For hydroxylation, they were incubated in 1 M KOH for 40 min in the ultrasonic cleaner, followed by rinsing with water and methanol. The coverslips were then treated with an aminosilanization mixture containing 3-aminopropyltriethoxysilane, acetate, and methanol for 10 min, rinsed with water for 1 min, and subjected to a second 10 min incubation in the aminosilanization mixture in the ultrasonic cleaner. The coverslips were then rinsed with methanol and air-dried. Hydroxylated coverslips were biotinylated by placing 30 µL of 25% biotin-PEG-succinimidyl valerate in $NaHCO_3$ buffer (pH 7.4) between two coverslip pieces, forming a sandwich, and incubating overnight at 4°C. The coverslips were then rinsed with water, air-dried, vacuum-sealed, and stored at -20°C. Flow chambers were prepared by attaching the PEG-biotin-coated coverslip to a glass slide using double-sided tape.

3.6.12 MT polymerization assays

Biotinylated MTs were prepared by diluting 4 µL of 38 mg/mL unlabeled pig brain tubulin and 2 mg/ml biotin-labeled pig brain tubulin in 56 µL BRB80 buffer (80 mM PIPES, pH 6.8, 1 mM $MgCl_2$, 1 mM EGTA). This mixture was combined with 60 µL of polymerization buffer (1x BRB80, 2 mM GTP, 20% DMSO) and incubated at 37°C for 45 min. After adding 1 mM taxol, the tubulin mixture was incubated for an additional 45 min at 37°C. The polymerized MTs were pelleted by centrifugation at 21,000 g for 15 min at 37°C and resuspended in 25 µL of BRB80 supplemented with 10 µM taxol and 1 mM DTT. The same procedure was followed to prepare

biotin-free, fluorescently labeled MTs by diluting 4 μL of 40 mg/mL pig brain tubulin, 5% of which was Cy3- or Cy5-labeled. For subtilisin treatment, 2 mg/mL polymerized MTs were incubated with 0.025 mg/mL subtilisin for 1 h at 37° C. The proteolytic activity of subtilisin was quenched by adding 1 mM PMSF. The cleavage of the tubulin tails by subtilisin was confirmed using denaturing gel analysis.

For GMPCPP-MT seed preparation, a mixture of unlabeled tubulin, 5% biotinylated tubulin, and 5% Cy3-labeled tubulin was diluted to 3 mg/mL in ice-cold BRB80 containing 10% DMSO. After 3 min incubation on ice, the mixture was centrifuged at 400,000 g for 10 min at 4°C. The supernatant was mixed with GMPCPP to a final concentration of 1 mM and incubated at 37°C for 20 min. The GMPCPP-stabilized MT seeds were pelleted by centrifugation at 400,000 g for 10 min at 37°C. The pellet was gently resuspended in 25 μL of BRB80 at room temperature.

3.6.13 Single-molecule motility assays

To immobilize biotinylated MTs, the PEG/PEG-biotin coated flow chambers were incubated with 1 mg/ml streptavidin for 3 min, followed by a wash with MB buffer (30 mM HEPES pH 7.4, 5 mM $MgSO_4$, 1 mM EGTA, 1 mM DTT, and 10 μM Taxol). The biotinylated MTs were then flowed into the chamber, incubated for another 3 min, and washed with MB buffer. For dynein motility assays, dynein and dynactin were mixed and incubated on ice for 3 min. NuMA was then added and incubated for an additional 3 min, followed by the addition of Lis1 with a further 3 min incubation. The molar ratio of the DDNL components in the stock mixture was 1:3:20:30 (dynein:dynactin:NuMA:Lis1) for N terminal NuMA constructs and 1:3:5:40 for NuMA FL constructs. The final volume of the DDNL stock mixture was adjusted to 10 μL by adding MBC buffer (MB buffer supplemented with 1 mg/mL casein, 0.5% pluronic acid, 100 mM KAc, and 0.4% methylcellulose). The DDNL stock was diluted 10-fold for the NuMA FL construct and 60-fold for the N-terminal NuMA construct. Both dilutions were prepared in imaging buffer (MBC buffer supplemented with 0.1 mg/mL glucose oxidase, 0.2 mg/mL catalase, 0.8% D-glucose, and 1 mM ATP) and introduced into the flow chamber. For DDN motility assays with N-terminal NuMA, 20 nM NuMA and 30 nM Lis1 were used in the flow chamber. For assays with NuMA FL, 20 nM NuMA and 160 nM Lis1 were used. Motility was recorded for 200 frames with 0.2 s exposure per frame.

For aster formation assays, biotinylated MTs were immobilized to the PEG/PEG-biotin surface. The DDNL mix with Cy3-labeled, biotin-free MTs was then flowed into the chamber. The aster formation was imaged by overlaying the mNG-labeled NuMA and Cy3-labeled MT channels. To assess the directionality of the MTs, Cy5-labeled KIF5B (a.a. 1-490) was added to the channel and imaged.

3.6.14 NuMA MT binding assays

To test the MT binding affinity of NuMA, taxol-stabilized MTs were labeled with Cy3 and biotin and immobilized on PEG/PEG-bio coated coverslips using streptavidin-biotin linkage. Serial dilutions of each mNG fused NuMA construct were flowed into the channel in MBC buffer supplemented with 0.1 mg/mL glucose oxidase, 0.2 mg/mL catalase, and 0.8% D-glucose. Images were taken for both the NuMA and MT channels under each condition.

To test the MT binding preference of NuMA, Cy3-labeled free-floating MTs were mixed with NuMA for 3 minutes, diluted in MBC buffer supplemented with 0.1 mg/mL glucose oxidase, 0.2 mg mL^{-1} catalase, 0.8% D-glucose, and 1mM ATP, and then flowed into a channel. 15 nM Cy5 labeled human kinesin-1 K490 was included in the imaging buffer to determine the directionality of the MTs. Final concentrations of 25 nM NuMA C, 165 nM MTBD1, 4 nM MTBD2, 25 nM NuMA-FL, 25 nM 3StoD, and 25 nM T2055D were used.

3.6.15 Dynamic MT assays

Biotinylated GMPCPP-MT seeds were immobilized in a 1 mg/mL streptavidin-coated flow chamber by incubating for 3 min. To generate dynamically growing and shrinking MTs, a dynamic MT mixture (2 mg/mL tubulin with 5% Cy3 labeling, 4 mM GTP, 1 mM ATP, 1 mg/mL casein, 0.5% pluronic acid, 1 mM DTT, and 0.2% methylcellulose in BRB80, pH 6.8,) was introduced into the chamber. To assess its effect, 100 nM of the NuMA C-mNG was added to the mixture. MT dynamics was monitored by timelapse imaging with 200 frames, a 0.2 s exposure time, and a 5000 s interval between the frames.

3.6.16 Mass photometry

High-precision coverslips (Azer Scientific) were cleaned sequentially with isopropanol and water three times, using an ultrasonic cleaner for 2 min per cycle, and then air-dried. Gaskets were rinsed alternately with water and isopropanol three times, air-dried, and placed on a clean coverslip. For autofocus, 14 µL of mass photometry buffer (50 mM HEPES, pH 7.4, 150 mM NaCl, 1 mM EGTA, and 10% glycerol) was loaded into a well of the gasket. The protein sample was diluted to 5–20 nM in mass photometry buffer and added to the autofocused gasket well. Protein contrast counts were measured using a TwoMP mass photometer (Refeyn 2) with a minimum of two replicates. The instrument was calibrated for mass measurements using a mixture of conalbumin, aldolase, and thyroglobulin. DiscoverMP software (Refeyn) was used to fit the mass photometry profiles to multiple skewed Gaussian peaks and to determine their mean, standard deviation, and proportions.

3.6.17 Peroxisome trafficking assays

Cells expressing both PEX3-mEmerald-FKBP and a NuMA-HaloTag-FRB construct were imaged every 30 s for approximately 50 min. Rapamycin was added to the dishes after 90 s of imaging. At the end of the time-lapse imaging, a z-stack was taken to determine whether peroxisomes had clustered at the centrosome. Peroxisome trafficking was determined by quantifying the ratio of final (45 min) to initial (0 min) PEX3 intensity integrated over 2.54 µm x 2.54 µm oval section at the centrosome using FIJI. Cells were considered to have trafficking if the ratio was above 2. As a control, the final to initial PEX3 intensity in the cytoplasm was also calculated. NuMA intensity in the cytoplasm was calculated over a 10.07 µm x 10.07 µm rectangular area using FIJI, averaged over three timepoints before rapamycin addition, and normalized to control. NuMA intensity at the centrosome was quantified over a 2.54 µm x 2.54 µm oval selection before rapamycin addition, averaged over three timepoints before rapamycin addition, and normalized to the control. Cells were considered to have NuMA accumulation if the normalized centrosomal intensity was above 1.2. In time-lapses where the centrosome remained in focus for the majority of imaging, PEX intensity was integrated over a 2.54 µm x 2.54 µm oval selection at the centrosome at every time

point and normalized to the first time point of imaging before rapamycin addition. Cells were transfected with different NuMA constructs on different days with variable transfection levels, which resulted in variability in protein expression levels. To account for this variability, the final/initial mEmerald signal was normalized for both centrosomal (Fig. 5c) and cytoplasmic (Ext. Data Fig. 9e) protein. We also normalized the Janelia Fluor 549 signal on exogenous NuMA in the cytoplasm and showed that variability in the fluorescence signal did not affect the trafficking outcome (Ext. Data Fig. 9d). Individual timepoints where the cell was temporarily out of focus were excluded from the traces. The assays were performed in the presence of endogenous NuMA, which typically localizes to the nucleus during interphase. We cannot rule out the possibility of endogenous NuMA to oligomerize or multimerize with expressed NuMA constructs in cycling cells.

3.6.18 Data analysis

Recorded movies of DDN single-molecule motility assays were analyzed using ImageJ. For two-color imaging, the fluorescence channels were merged in ImageJ to create a composite image. A custom ImageJ macro was used to generate kymographs by plotting segmented lines along MTs. For run frequency analysis, the number of processive NuMA molecules on each MT was divided by the MT length (μm), time (min), and NuMA concentration (μM). Dynein's velocity and run length were determined by identifying the start and end points of each processive NuMA run. For MT binding assays, the intensity of NuMA on the MTs was quantified after background subtraction using a custom MATLAB code (MTIMBS). The dynamic MT growth velocity was calculated by drawing kymographs and identifying the start and end points of each growing end in ImageJ.

To determine the binding preference of different NuMA constructs on biotin-free MTs, NuMA fused to mNG, Cy3-labeled MTs, and Cy5-labeled KIF5B (1-490) channels were overlaid. MTs with mNG signal accumulated at one or both ends were manually counted as exhibiting end-binding. The directionality of the MTs was confirmed by analyzing the movement of KIF5B (1-490) through kymographs. NuMA-bound MTs without signal accumulation at the tips were quantified as displaying lattice binding.

3.6.19 Statistical analysis

P values were determined using statistical tests in Prism. Fisher's exact tests were performed to compare categorical datasets. Two-sided two-sample t-tests were performed to compare continuous datasets, assuming that NuMA and dynein levels are approximately normally distributed. Each result was based on a minimum of two independent experiments. The number of replicates and data points (n) and the specific statistical methods used are provided in the figure legends. Representative data from independently repeated experiments are shown.

Chapter 4. Concluding Remarks

Motor proteins are regulated at multiple levels to coordinate their essential roles spatially and temporally within the cell. For my thesis work, I reconstituted the mitochondrial transport machinery in vitro and showed that the adaptor protein TRAK activates both kinesin and dynein. TRAK can recruit the two motors simultaneously, and these complexes move exclusively toward the microtubule plus end at kinesin speed, indicating that dynein is carried as an inactive passenger. I also found that mitochondrial pausing is not mediated by Miro-dependent inhibition of motors, but instead by syntaphilin, which acts as a static anchor to oppose motor-driven motility.

The TRAK study provides evidence that kinesin transports dynein to the plus ends of axonal microtubules, which are located far from the cell soma. However, further studies are necessary to elucidate the mechanism that switches between plus- and minus-end-directed motors. One important approach to better understand TRAK-mediated regulation of opposing motors would be to assemble the dynein–dynactin–TRAK–kinesin complex on microtubules and determine its structure using single-particle cryo-EM. We hypothesize that the resulting DDKT complex will contain kinesin in an active conformation, whereas dynein may remain associated but unable to form an active motile complex. In contrast, complexes containing active dynein bound to TRAK may exclude kinesin binding. Resolving the binding interfaces of the motors in both active and inactive conformations will provide mechanistic insight into how TRAK coordinates opposing motor activities.

Additionally, Gladkova et al. identified a dynein regulatory helix (DRH) on TRAK adaptors and showed that the open conformational state of DRH biases dynein-driven motility over kinesin by enabling DLIC to interact with the TRAK CC1-box[145]. When the DRH is in the closed conformation, dynein is unable to bind to the CC1 box, allowing kinesin to engage for anterograde motility, while inactive dynein-dynactin remains associated with the complex through the Spindly motif. Furthermore, they showed that TRAK1 and 2 exhibit different DRH conformations and that these states can be modulated by physiological signaling, such as stress-induced kinase phosphorylation, potentially explaining the distribution of mitochondria in axons.

In my second project, I investigated the activation and regulation of the dynein-dynactin-NuMA complex using biochemical reconstitution, single-particle cryo-EM, and live-cell imaging. I found that the N-terminal coiled-coil of NuMA activates dynein and recruits two dynein dimers to dynactin through specific tail interactions, while the C-terminal region binds and stabilizes microtubule minus ends. Full-length NuMA is autoinhibited during interphase and is activated by mitotic phosphorylation, enabling the dynein-dynactin-NuMA complex to sort and focus microtubule minus ends into aster-like structures.

Although I demonstrated that dynein activation by the N-terminal region of NuMA is inhibited by both the extended coiled-coil and the C-terminal region, further studies are required to elucidate the autoinhibition mechanism of NuMA. Cross-linking mass spectrometry (XL-MS) of full-length NuMA may reveal the inhibitory molecular interactions within the protein. Further point mutations based on the interacting sites may provide a more in-depth understanding of the autoinhibition mechanism.

Furthermore, previous studies and our negative-stain analysis of full-length NuMA indicate that NuMA clusters through its C-terminus. However, the exact molecular mechanism underlying this clustering remains unknown. Careful experiments will be required to determine the specific

sequences responsible for clustering, the effect of the coiled-coil region on this process, and how clustering may influence NuMA's dynein activation and microtubule interaction.

While we know that NuMA interacts with MTs through tubulin C-terminal tails using two distinct MT-binding domains on its C-terminus, MTBD1 and MTBD2, the exact MT-binding sequences have not yet been identified. MTBD1 mediates NuMA's MT minus end binding, but the underlying mechanism remains unknown. To identify the exact MT-binding sequences, point mutations can be generated in MTBD1 and MTBD2 and tested for their effects on MT-binding affinity. To further evaluate NuMA's MT minus-end recognition, one should test MTBD1 binding affinity to alpha tubulin C-terminal tail peptide in comparison to beta tubulin C-terminal tail peptide using biolayer interferometry. Another approach would be to mix MTBD1 with unpolymerized tubulin and investigate binding to alpha versus beta tubulin using cross-linking followed by mass spectrometry. Furthermore, testing MTBD1 and MTBD2 binding to microtubules polymerized from recombinantly expressed alpha-tubulin lacking C-terminal tail or beta-tubulin lacking the C-terminal tail would provide direct evidence for potential tubulin tail preferences of NuMA.

The microtubule binding ability of NuMA is also inhibited in the full-length protein, and mitotic phosphorylation does not appear to rescue this activity in vitro. Future studies that generate point mutations in the microtubule-binding regions, as well as further evaluation of NuMA's other known C-terminal binding partners, such as LGN, 4.1R, PIPs, and importins, may shed light on this mechanism. NuMA also interacts with the minus-end-directed motor HSET (KIFC1) during mitosis, facilitating microtubule focusing through crosslinking. Investigating the combined effects of HSET and the active dynein-dynactin-NuMA complex on aster formation may reveal the molecular principles underlying spindle pole focusing.

REFERENCES

1. Hirokawa, N., Noda, Y., Tanaka, Y. & Niwa, S. Kinesin superfamily motor proteins and intracellular transport. *Nat Rev Mol Cell Biol* **10**, 682-96 (2009).
2. Hirokawa, N. Kinesin and dynein superfamily proteins and the mechanism of organelle transport. *Science* **279**, 519-26 (1998).
3. Rahman, A., Kamal, A., Roberts, E.A. & Goldstein, L.S. Defective kinesin heavy chain behavior in mouse kinesin light chain mutants. *J Cell Biol* **146**, 1277-88 (1999).
4. Rice, S. et al. A structural change in the kinesin motor protein that drives motility. *Nature* **402**, 778-84 (1999).
5. Hackney, D.D. The rate-limiting step in microtubule-stimulated ATP hydrolysis by dimeric kinesin head domains occurs while bound to the microtubule. *J Biol Chem* **269**, 16508-11 (1994).
6. Kawaguchi, K. & Ishiwata, S. Nucleotide-dependent single- to double-headed binding of kinesin. *Science* **291**, 667-9. (2001).
7. Cao, L. et al. The structure of apo-kinesin bound to tubulin links the nucleotide cycle to movement. *Nat Commun* **5**, 5364 (2014).
8. Yildiz, A. Mechanism and regulation of kinesin motors. *Nat Rev Mol Cell Biol* (2024).
9. Asenjo, A.B. & Sosa, H. A mobile kinesin-head intermediate during the ATP-waiting state. *Proc Natl Acad Sci U S A* **106**, 5657-62 (2009).
10. Guydosh, N.R. & Block, S.M. Direct observation of the binding state of the kinesin head to the microtubule. *Nature* **461**, 125-8 (2009).
11. Roberts, A.J., Kon, T., Knight, P.J., Sutoh, K. & Burgess, S.A. Functions and mechanics of dynein motor proteins. *Nat Rev Mol Cell Biol* **14**, 713-26 (2013).
12. Yildiz, A. & Zhao, Y. Dyneins. *Curr Biol* **33**, R1274-R1279 (2023).
13. Canty, J.T. & Yildiz, A. Activation and Regulation of Cytoplasmic Dynein. *Trends Biochem Sci* **45**, 440-453 (2020).
14. Kon, T., Sutoh, K. & Kurisu, G. X-ray structure of a functional full-length dynein motor domain. *Nat Struct Mol Biol* **18**, 638-42 (2011).
15. Roberts, A.J. et al. AAA+ Ring and linker swing mechanism in the dynein motor. *Cell* **136**, 485-95 (2009).
16. Urnavicius, L. et al. The structure of the dynactin complex and its interaction with dynein. *Science* **347**, 1441-1446 (2015).
17. Carter, A.P. Crystal clear insights into how the dynein motor moves. *J Cell Sci* **126**, 705-13 (2013).
18. Redwine, W.B. et al. The human cytoplasmic dynein interactome reveals novel activators of motility. *Elife* **6**(2017).
19. Radulescu, A.E. & Cleveland, D.W. NuMA after 30 years: the matrix revisited. *Trends Cell Biol* **20**, 214-22 (2010).
20. Serra-Marques, A. et al. The mitotic protein NuMA plays a spindle-independent role in nuclear formation and mechanics. *J Cell Biol* **219**(2020).
21. Merdes, A., Ramyar, K., Vechio, J.D. & Cleveland, D.W. A complex of NuMA and cytoplasmic dynein is essential for mitotic spindle assembly. *Cell* **87**, 447-58 (1996).
22. Heald, R. et al. Self-organization of microtubules into bipolar spindles around artificial chromosomes in Xenopus egg extracts. *Nature* **382**, 420-5 (1996).

23. Merdes, A., Heald, R., Samejima, K., Earnshaw, W.C. & Cleveland, D.W. Formation of spindle poles by dynein/dynactin-dependent transport of NuMA. *J Cell Biol* **149**, 851-62 (2000).
24. Sikirzhytski, V. et al. Direct kinetochore-spindle pole connections are not required for chromosome segregation. *J Cell Biol* **206**, 231-43 (2014).
25. Elting, M.W., Hueschen, C.L., Udy, D.B. & Dumont, S. Force on spindle microtubule minus ends moves chromosomes. *J Cell Biol* **206**, 245-56 (2014).
26. Hueschen, C.L., Kenny, S.J., Xu, K. & Dumont, S. NuMA recruits dynein activity to microtubule minus-ends at mitosis. *Elife* **6**(2017).
27. Tanenbaum, M.E., Macurek, L., Galjart, N. & Medema, R.H. Dynein, Lis1 and CLIP-170 counteract Eg5-dependent centrosome separation during bipolar spindle assembly. *EMBO J* **27**, 3235-45 (2008).
28. Ferenz, N.P., Paul, R., Fagerstrom, C., Mogilner, A. & Wadsworth, P. Dynein antagonizes eg5 by crosslinking and sliding antiparallel microtubules. *Curr Biol* **19**, 1833-8 (2009).
29. Hueschen, C.L., Galstyan, V., Amouzgar, M., Phillips, R. & Dumont, S. Microtubule End-Clustering Maintains a Steady-State Spindle Shape. *Curr Biol* **29**, 700-708 e5 (2019).
30. Neahring, L., Cho, N.H. & Dumont, S. Opposing motors provide mechanical and functional robustness in the human spindle. *Dev Cell* **56**, 3006-3018 e5 (2021).
31. Du, Q. & Macara, I.G. Mammalian Pins is a conformational switch that links NuMA to heterotrimeric G proteins. *Cell* **119**, 503-16 (2004).
32. Seldin, L., Poulson, N.D., Foote, H.P. & Lechler, T. NuMA localization, stability, and function in spindle orientation involve 4.1 and Cdk1 interactions. *Mol Biol Cell* **24**, 3651-62 (2013).
33. Kotak, S., Busso, C. & Gonczy, P. NuMA interacts with phosphoinositides and links the mitotic spindle with the plasma membrane. *EMBO J* **33**, 1815-30 (2014).
34. Zheng, Z., Wan, Q., Meixiong, G. & Du, Q. Cell cycle-regulated membrane binding of NuMA contributes to efficient anaphase chromosome separation. *Mol Biol Cell* **25**, 606-19 (2014).
35. Okumura, M., Natsume, T., Kanemaki, M.T. & Kiyomitsu, T. Dynein-Dynactin-NuMA clusters generate cortical spindle-pulling forces as a multi-arm ensemble. *Elife* **7**(2018).
36. Kotak, S., Busso, C. & Gonczy, P. Cortical dynein is critical for proper spindle positioning in human cells. *J Cell Biol* **199**, 97-110 (2012).
37. Kiyomitsu, T. & Cheeseman, I.M. Chromosome- and spindle-pole-derived signals generate an intrinsic code for spindle position and orientation. *Nat Cell Biol* **14**, 311-7 (2012).
38. Kiyomitsu, T. & Boerner, S. The Nuclear Mitotic Apparatus (NuMA) Protein: A Key Player for Nuclear Formation, Spindle Assembly, and Spindle Positioning. *Front Cell Dev Biol* **9**, 653801 (2021).
39. Lydersen, B.K. & Pettijohn, D.E. Human-specific nuclear protein that associates with the polar region of the mitotic apparatus: distribution in a human/hamster hybrid cell. *Cell* **22**, 489-99 (1980).
40. Harborth, J., Wang, J., Gueth-Hallonet, C., Weber, K. & Osborn, M. Self assembly of NuMA: multiarm oligomers as structural units of a nuclear lattice. *EMBO J* **18**, 1689-700 (1999).

41. Gueth-Hallonet, C., Wang, J., Harborth, J., Weber, K. & Osborn, M. Induction of a regular nuclear lattice by overexpression of NuMA. *Exp Cell Res* **243**, 434-52 (1998).
42. Cho, N.H., Aslan, M., Taheri, A., Yildiz, A. & Dumont, S. NuMA mechanically reinforces the spindle independently of its partner dynein. *Curr Biol* **35**, 4084-4095 e5 (2025).
43. Kiyomitsu, T. The cortical force-generating machinery: how cortical spindle-pulling forces are generated. *Curr Opin Cell Biol* **60**, 1-8 (2019).
44. Pirovano, L. et al. Hexameric NuMA:LGN structures promote multivalent interactions required for planar epithelial divisions. *Nat Commun* **10**, 2208 (2019).
45. Chang, C.C., Huang, T.L., Shimamoto, Y., Tsai, S.Y. & Hsia, K.C. Regulation of mitotic spindle assembly factor NuMA by Importin-beta. *J Cell Biol* **216**, 3453-3462 (2017).
46. Silk, A.D., Holland, A.J. & Cleveland, D.W. Requirements for NuMA in maintenance and establishment of mammalian spindle poles. *J Cell Biol* **184**, 677-90 (2009).
47. Tsuchiya, K. et al. Ran-GTP Is Non-essential to Activate NuMA for Mitotic Spindle-Pole Focusing but Dynamically Polarizes HURP Near Chromosomes. *Curr Biol* **31**, 115-127 e3 (2021).
48. Seldin, L., Muroyama, A. & Lechler, T. NuMA-microtubule interactions are critical for spindle orientation and the morphogenesis of diverse epidermal structures. *Elife* **5**(2016).
49. Sheng, Z.H. & Cai, Q. Mitochondrial transport in neurons: impact on synaptic homeostasis and neurodegeneration. *Nat Rev Neurosci* **13**, 77-93 (2012).
50. Wong, Y.C. & Holzbaur, E.L. The regulation of autophagosome dynamics by huntingtin and HAP1 is disrupted by expression of mutant huntingtin, leading to defective cargo degradation. *J Neurosci* **34**, 1293-305 (2014).
51. Guo, X. et al. The GTPase dMiro is required for axonal transport of mitochondria to Drosophila synapses. *Neuron* **47**, 379-93 (2005).
52. Glater, E.E., Megeath, L.J., Stowers, R.S. & Schwarz, T.L. Axonal transport of mitochondria requires milton to recruit kinesin heavy chain and is light chain independent. *J Cell Biol* **173**, 545-57 (2006).
53. Macaskill, A.F. et al. Miro1 is a calcium sensor for glutamate receptor-dependent localization of mitochondria at synapses. *Neuron* **61**, 541-55 (2009).
54. Stowers, R.S., Megeath, L.J., Gorska-Andrzejak, J., Meinertzhagen, I.A. & Schwarz, T.L. Axonal transport of mitochondria to synapses depends on milton, a novel Drosophila protein. *Neuron* **36**, 1063-77 (2002).
55. van Spronsen, M. et al. TRAK/Milton motor-adaptor proteins steer mitochondrial trafficking to axons and dendrites. *Neuron* **77**, 485-502 (2013).
56. Fransson, S., Ruusala, A. & Aspenstrom, P. The atypical Rho GTPases Miro-1 and Miro-2 have essential roles in mitochondrial trafficking. *Biochem Biophys Res Commun* **344**, 500-10 (2006).
57. Brickley, K. & Stephenson, F.A. Trafficking kinesin protein (TRAK)-mediated transport of mitochondria in axons of hippocampal neurons. *J Biol Chem* **286**, 18079-92 (2011).
58. Morris, R.L. & Hollenbeck, P.J. Axonal transport of mitochondria along microtubules and F-actin in living vertebrate neurons. *J Cell Biol* **131**, 1315-26 (1995).
59. Overly, C.C., Rieff, H.I. & Hollenbeck, P.J. Organelle motility and metabolism in axons vs dendrites of cultured hippocampal neurons. *J Cell Sci* **109 (Pt 5)**, 971-80 (1996).

60. Pilling, A.D., Horiuchi, D., Lively, C.M. & Saxton, W.M. Kinesin-1 and Dynein are the primary motors for fast transport of mitochondria in Drosophila motor axons. *Mol Biol Cell* **17**, 2057-68 (2006).
61. Saxton, W.M. & Hollenbeck, P.J. The axonal transport of mitochondria. *J Cell Sci* **125**, 2095-104 (2012).
62. Henrichs, V. et al. Mitochondria-adaptor TRAK1 promotes kinesin-1 driven transport in crowded environments. *Nat Commun* **11**, 3123 (2020).
63. Fenton, A.R., Jongens, T.A. & Holzbaur, E.L.F. Mitochondrial adaptor TRAK2 activates and functionally links opposing kinesin and dynein motors. *Nat Commun* **12**, 4578 (2021).
64. Saotome, M. et al. Bidirectional Ca2+-dependent control of mitochondrial dynamics by the Miro GTPase. *Proc Natl Acad Sci U S A* **105**, 20728-33 (2008).
65. Wang, X. & Schwarz, T.L. The mechanism of Ca2+ -dependent regulation of kinesin-mediated mitochondrial motility. *Cell* **136**, 163-74 (2009).
66. Kang, J.S. et al. Docking of axonal mitochondria by syntaphilin controls their mobility and affects short-term facilitation. *Cell* **132**, 137-48 (2008).
67. Nguyen, T.T. et al. Loss of Miro1-directed mitochondrial movement results in a novel murine model for neuron disease. *Proc Natl Acad Sci U S A* **111**, E3631-40 (2014).
68. Chen, Y. & Sheng, Z.H. Kinesin-1-syntaphilin coupling mediates activity-dependent regulation of axonal mitochondrial transport. *J Cell Biol* **202**, 351-64 (2013).
69. Reck-Peterson, S.L., Redwine, W.B., Vale, R.D. & Carter, A.P. The cytoplasmic dynein transport machinery and its many cargoes. *Nat Rev Mol Cell Biol* **19**, 382-398 (2018).
70. Schroeder, C.M. & Vale, R.D. Assembly and activation of dynein-dynactin by the cargo adaptor protein Hook3. *J Cell Biol* **214**, 309-18 (2016).
71. Gama, J.B. et al. Molecular mechanism of dynein recruitment to kinetochores by the Rod-Zw10-Zwilch complex and Spindly. *J Cell Biol* **216**, 943-960 (2017).
72. McKenney, R.J., Huynh, W., Tanenbaum, M.E., Bhabha, G. & Vale, R.D. Activation of cytoplasmic dynein motility by dynactin-cargo adapter complexes. *Science* **345**, 337-41 (2014).
73. Schlager, M.A., Hoang, H.T., Urnavicius, L., Bullock, S.L. & Carter, A.P. In vitro reconstitution of a highly processive recombinant human dynein complex. *EMBO J* **33**, 1855-68 (2014).
74. Elshenawy, M.M. et al. Cargo adaptors regulate stepping and force generation of mammalian dynein-dynactin. *Nat Chem Biol* **15**, 1093-1101 (2019).
75. Elshenawy, M.M. et al. Lis1 activates dynein motility by modulating its pairing with dynactin. *Nat Cell Biol* **22**, 570-578 (2020).
76. Htet, Z.M. et al. LIS1 promotes the formation of activated cytoplasmic dynein-1 complexes. *Nat Cell Biol* **22**, 518-525 (2020).
77. Marzo, M.G., Griswold, J.M. & Markus, S.M. Pac1/LIS1 stabilizes an uninhibited conformation of dynein to coordinate its localization and activity. *Nat Cell Biol* **22**, 559-569 (2020).
78. Kozielski, F. et al. The crystal structure of dimeric kinesin and implications for microtubule-dependent motility. *Cell* **91**, 985-94. (1997).
79. Hooikaas, P.J. et al. MAP7 family proteins regulate kinesin-1 recruitment and activation. *J Cell Biol* **218**, 1298-1318 (2019).

80. Monroy, B.Y. et al. Competition between microtubule-associated proteins directs motor transport. *Nat Commun* **9**, 1487 (2018).
81. Ferro, L.S. et al. Structural and functional insight into regulation of kinesin-1 by microtubule-associated protein MAP7. *Science* **375**, 326-331 (2022).
82. Belyy, V. et al. The mammalian dynein-dynactin complex is a strong opponent to kinesin in a tug-of-war competition. *Nat Cell Biol* **18**, 1018-24 (2016).
83. Derr, N.D. et al. Tug-of-war in motor protein ensembles revealed with a programmable DNA origami scaffold. *Science* **338**, 662-5 (2012).
84. Babic, M. et al. Miro's N-terminal GTPase domain is required for transport of mitochondria into axons and dendrites. *J Neurosci* **35**, 5754-71 (2015).
85. Bodakuntla, S., Jijumon, A.S., Villablanca, C., Gonzalez-Billault, C. & Janke, C. Microtubule-Associated Proteins: Structuring the Cytoskeleton. *Trends Cell Biol* **29**, 804-819 (2019).
86. Chen, O. et al. Compact high-quality CdSe-CdS core-shell nanocrystals with narrow emission linewidths and suppressed blinking. *Nat Mater* **12**, 445-51 (2013).
87. Tymanskyj, S.R., Yang, B.H., Verhey, K.J. & Ma, L. MAP7 regulates axon morphogenesis by recruiting kinesin-1 to microtubules and modulating organelle transport. *Elife* **7**, 36374 (2018).
88. Chiba, K., Ori-McKenney, K.M., Niwa, S. & McKenney, R.J. Synergistic autoinhibition and activation mechanisms control kinesin-1 motor activity. *Cell Rep* **39**, 111016 (2022).
89. Niescier, R.F., Kwak, S.K., Joo, S.H., Chang, K.T. & Min, K.T. Dynamics of Mitochondrial Transport in Axons. *Front Cell Neurosci* **10**, 123 (2016).
90. Hirokawa, N., Sato-Yoshitake, R., Yoshida, T. & Kawashima, T. Brain dynein (MAP1C) localizes on both anterogradely and retrogradely transported membranous organelles in vivo. *J Cell Biol* **111**, 1027-37 (1990).
91. Hirokawa, N. et al. Kinesin associates with anterogradely transported membranous organelles in vivo. *J Cell Biol* **114**, 295-302 (1991).
92. Schwarz, T.L. Mitochondrial Trafficking in Neurons. *Cold Spring Harbor Perspectives in Biology* **5**(2013).
93. Kendrick, A.A. et al. Hook3 is a scaffold for the opposite-polarity microtubule-based motors cytoplasmic dynein-1 and KIF1C. *J Cell Biol* **218**, 2982-3001 (2019).
94. Urnavicius, L. et al. Cryo-EM shows how dynactin recruits two dyneins for faster movement. *Nature* **554**, 202-206 (2018).
95. Gibson, J.M. et al. Coil-to-alpha-helix transition at the Nup358-BicD2 interface activates BicD2 for dynein recruitment. *Elife* **11**, 74714 (2022).
96. Ogawa, F. et al. DISC1 complexes with TRAK1 and Miro1 to modulate anterograde axonal mitochondrial trafficking. *Hum Mol Genet* **23**, 906-19 (2014).
97. Cartoni, R. et al. The Mammalian-Specific Protein Armcx1 Regulates Mitochondrial Transport during Axon Regeneration. *Neuron* **94**, 689 (2017).
98. Lopez-Domenech, G. et al. The Eutherian Armcx genes regulate mitochondrial trafficking in neurons and interact with Miro and Trak2. *Nat Commun* **3**, 814 (2012).
99. Bingham, J.B., King, S.J. & Schroer, T.A. Purification of dynactin and dynein from brain tissue. *Methods Enzymol* **298**, 171-84 (1998).
100. Canty, J.T., Tan, R., Kusakci, E., Fernandes, J. & Yildiz, A. Structure and Mechanics of Dynein Motors. *Annu Rev Biophys* **50**, 549-574 (2021).

101. Trokter, M., Mucke, N. & Surrey, T. Reconstitution of the human cytoplasmic dynein complex. *Proc Natl Acad Sci U S A* **109**, 20895-900 (2012).
102. Torisawa, T. et al. Autoinhibition and cooperative activation mechanisms of cytoplasmic dynein. *Nat Cell Biol* **16**, 1118-24 (2014).
103. Zhang, K. et al. Cryo-EM Reveals How Human Cytoplasmic Dynein Is Auto-inhibited and Activated. *Cell* **169**, 1303-1314 e18 (2017).
104. Renna, C. et al. Organizational Principles of the NuMA-Dynein Interaction Interface and Implications for Mitotic Spindle Functions. *Structure* **28**, 820-829 e6 (2020).
105. Sun, M. et al. NuMA regulates mitotic spindle assembly, structural dynamics and function via phase separation. *Nat Commun* **12**, 7157 (2021).
106. Harborth, J., Weber, K. & Osborn, M. Epitope mapping and direct visualization of the parallel, in-register arrangement of the double-stranded coiled-coil in the NuMA protein. *EMBO J* **14**, 2447-60 (1995).
107. Forth, S., Hsia, K.C., Shimamoto, Y. & Kapoor, T.M. Asymmetric friction of nonmotor MAPs can lead to their directional motion in active microtubule networks. *Cell* **157**, 420-432 (2014).
108. Chaaban, S. & Carter, A.P. Structure of dynein-dynactin on microtubules shows tandem adaptor binding. *Nature* **610**, 212-216 (2022).
109. Singh, K. et al. Molecular mechanism of dynein-dynactin complex assembly by LIS1. *Science* **383**, eadk8544 (2024).
110. Lee, I.G. et al. A conserved interaction of the dynein light intermediate chain with dynein-dynactin effectors necessary for processivity. *Nat Commun* **9**, 986 (2018).
111. Canty, J.T., Hensley, A., Aslan, M., Jack, A. & Yildiz, A. TRAK adaptors regulate the recruitment and activation of dynein and kinesin in mitochondrial transport. *Nat Commun* **14**, 1376 (2023).
112. Gladkova, C. et al. A molecular switch for stress-induced activation of retrograde mitochondrial transport. *bioRxiv*, 2024.09.13.612963 (2024).
113. Compton, D.A., Szilak, I. & Cleveland, D.W. Primary structure of NuMA, an intranuclear protein that defines a novel pathway for segregation of proteins at mitosis. *J Cell Biol* **116**, 1395-408 (1992).
114. Yang, C.H., Lambie, E.J. & Snyder, M. NuMA: an unusually long coiled-coil related protein in the mammalian nucleus. *J Cell Biol* **116**, 1303-17 (1992).
115. So, C. et al. Mechanism of spindle pole organization and instability in human oocytes. *Science* **375**, eabj3944 (2022).
116. Carter, A.P. et al. Structure and functional role of dynein's microtubule-binding domain. *Science* **322**, 1691-5 (2008).
117. Fagiewicz, R. et al. In vitro characterization of the full-length human dynein-1 cargo adaptor BicD2. *Structure* **30**, 1470-1478 e3 (2022).
118. d'Amico, E.A. et al. Conformational transitions of the Spindly adaptor underlie its interaction with Dynein and Dynactin. *J Cell Biol* **221**(2022).
119. Gallini, S. et al. NuMA Phosphorylation by Aurora-A Orchestrates Spindle Orientation. *Curr Biol* **26**, 458-69 (2016).
120. Saredi, A., Howard, L. & Compton, D.A. Phosphorylation regulates the assembly of NuMA in a mammalian mitotic extract. *J Cell Sci* **110 (Pt 11)**, 1287-97 (1997).
121. Kotak, S., Busso, C. & Gonczy, P. NuMA phosphorylation by CDK1 couples mitotic progression with cortical dynein function. *EMBO J* **32**, 2517-29 (2013).

122. Kotak, S., Afshar, K., Busso, C. & Gonczy, P. Aurora A kinase regulates proper spindle positioning in C. elegans and in human cells. *J Cell Sci* **129**, 3015-25 (2016).
123. Kettenbach, A.N. et al. Quantitative phosphoproteomics identifies substrates and functional modules of Aurora and Polo-like kinase activities in mitotic cells. *Sci Signal* **4**, rs5 (2011).
124. Sana, S., Keshri, R., Rajeevan, A., Kapoor, S. & Kotak, S. Plk1 regulates spindle orientation by phosphorylating NuMA in human cells. *Life Sci Alliance* **1**, e201800223 (2018).
125. Stevens, D.A. et al. Antiviral function and viral antagonism of the rapidly evolving dynein activating adaptor NINL. *Elife* **11**(2022).
126. Atherton, J. et al. Structural determinants of microtubule minus end preference in CAMSAP CKK domains. *Nat Commun* **10**, 5236 (2019).
127. Aher, A., Urnavicius, L., Xue, A., Neselu, K. & Kapoor, T.M. Structure of the gamma-tubulin ring complex-capped microtubule. *Nat Struct Mol Biol* **31**, 1124-1133 (2024).
128. van Toorn, M., Shintomi, K. & Kiyomitsu, T. CDK1-dependent N-terminal NuMA phosphorylation promotes dynein-dynactin-NuMA assembly for accurate chromosome segregation. *bioRxiv*, 2025.07.19.665708 (2025).
129. Colombo, S. et al. NuMA is a mitotic adaptor protein that activates dynein and connects it to microtubule minus ends. *J Cell Biol* **224**(2025).
130. van Toorn, M., Gooch, A., Boerner, S. & Kiyomitsu, T. NuMA deficiency causes micronuclei via checkpoint-insensitive k-fiber minus-end detachment from mitotic spindle poles. *Curr Biol* **33**, 572-580 e2 (2023).
131. Wittmann, T., Wilm, M., Karsenti, E. & Vernos, I. TPX2, A novel xenopus MAP involved in spindle pole organization. *J Cell Biol* **149**, 1405-18 (2000).
132. Rohou, A. & Grigorieff, N. CTFFIND4: Fast and accurate defocus estimation from electron micrographs. *J Struct Biol* **192**, 216-21 (2015).
133. Zheng, S.Q. et al. MotionCor2: anisotropic correction of beam-induced motion for improved cryo-electron microscopy. *Nat Methods* **14**, 331-332 (2017).
134. Kimanius, D., Dong, L., Sharov, G., Nakane, T. & Scheres, S.H.W. New tools for automated cryo-EM single-particle analysis in RELION-4.0. *Biochem J* **478**, 4169-4185 (2021).
135. Wagner, T. et al. SPHIRE-crYOLO is a fast and accurate fully automated particle picker for cryo-EM. *Commun Biol* **2**, 218 (2019).
136. Chai, P., Rao, Q. & Zhang, K. Multi-curve fitting and tubulin-lattice signal removal for structure determination of large microtubule-based motors. *J Struct Biol* **214**, 107897 (2022).
137. Punjani, A., Rubinstein, J.L., Fleet, D.J. & Brubaker, M.A. cryoSPARC: algorithms for rapid unsupervised cryo-EM structure determination. *Nat Methods* **14**, 290-296 (2017).
138. Croll, T.I. ISOLDE: a physically realistic environment for model building into low-resolution electron-density maps. *Acta Crystallogr D Struct Biol* **74**, 519-530 (2018).
139. Emsley, P., Lohkamp, B., Scott, W.G. & Cowtan, K. Features and development of Coot. *Acta Crystallogr D Biol Crystallogr* **66**, 486-501 (2010).
140. Afonine, P.V. et al. Real-space refinement in PHENIX for cryo-EM and crystallography. *Acta Crystallogr D Struct Biol* **74**, 531-544 (2018).
141. Meng, E.C. et al. UCSF ChimeraX: Tools for structure building and analysis. *Protein Sci* **32**, e4792 (2023).

142. Mirdita, M. et al. ColabFold: making protein folding accessible to all. *Nat Methods* **19**, 679-682 (2022).
143. Mirdita, M., Steinegger, M. & Soding, J. MMseqs2 desktop and local web server app for fast, interactive sequence searches. *Bioinformatics* **35**, 2856-2858 (2019).
144. Evans, R. et al. Protein complex prediction with AlphaFold-Multimer. *bioRxiv*, 2021.10.04.463034 (2022).
145. Gladkova, C., Paez-Segala, M.G., Myers, S.A. & Vale, R.D. The molecular basis for stress-induced activation of retrograde mitochondrial transport. *Molecular Biology of the Cell* **35**(2024).